

# Snow, ice and solar radiation

Peter Kuipers Munneke



Copyright © 2009, P. Kuipers Munneke, Utrecht, The Netherlands

Author: Peter Kuipers Munneke  
ISBN: 978-90-393-5164-2  
Printing: Ipskamp Drukkers BV, Enschede

Institute for Marine and Atmospheric research Utrecht (IMAU)  
Department of Physics and Astronomy  
Faculty of Science  
Utrecht University

Cover: A hexagonal stellar-plate snow crystal. Snow crystals are the building blocks of ice sheets and glaciers. The typical six-fold symmetry is determined by the hexagonal structure of the  $\text{H}_2\text{O}$  molecules in the ice crystal lattice. Stellar plates grow when the ambient temperature is around  $-2^\circ\text{C}$  or between  $-10$  and  $-20^\circ\text{C}$ .

# Snow, ice and solar radiation

Sneeuw, ijs en zonnestraling

(met een samenvatting in het Nederlands)

PROEFSCHRIFT

ter verkrijging van de graad van doctor aan de  
Universiteit Utrecht op gezag van de rector magnificus,  
prof. dr. J.C. Stoof, ingevolge het besluit van het  
college voor promoties in het openbaar te verdedigen  
op 14 oktober 2009 des middags te 4.15 uur

door

Peter Kuipers Munneke

geboren op 31 maart 1980 te Groningen

Promotor: Prof. dr. J. Oerlemans  
Co-promotor: Dr. C. H. Tijm-Reijmer

# Contents

<b>Samenvatting</b>	<b>iii</b>
<b>Summary</b>	<b>vii</b>
<b>1 Snow, ice and climate</b>	<b>1</b>
1.1 The role of solar radiation in the climate system . . . . .	1
1.2 The albedo of snow and ice . . . . .	2
1.3 Snow and ice in past climate . . . . .	4
1.4 Present-day climate change . . . . .	5
1.5 Modelling snow and ice albedo . . . . .	8
1.6 The Summit Radiation Experiment (SURE '07) . . . . .	10
1.7 This thesis . . . . .	13
<b>2 Broadband radiative transfer</b>	<b>15</b>
2.1 Introduction . . . . .	16
2.2 Single scattering . . . . .	16
2.3 Multiple scattering . . . . .	20
2.4 Doubling-adding method . . . . .	21
2.5 Correlated $k$ -distribution method . . . . .	23
2.6 Validation I: Model intercomparison . . . . .	28
2.7 Validation II: Clear-sky radiative closure study . . . . .	31
2.8 Conclusions . . . . .	33
<b>3 Modelling radiative transfer in the snow-atmosphere system</b>	<b>35</b>
3.1 Introduction . . . . .	36
3.2 Optical properties of snow and clouds . . . . .	36
3.3 Clear-sky snow albedo . . . . .	39
3.4 Cloudy-sky snow albedo . . . . .	44

<b>4</b>	<b>Analysis of clear-sky Antarctic snow albedo</b>	<b>47</b>
4.1	Introduction . . . . .	48
4.2	Data and methods . . . . .	48
4.3	Results . . . . .	53
4.4	Discussion . . . . .	56
4.5	Summary and conclusions . . . . .	58
<b>5</b>	<b>Cloud properties from radiation measurements over snow and ice</b>	<b>61</b>
5.1	Introduction . . . . .	62
5.2	Data and methods . . . . .	63
5.3	Results . . . . .	70
5.4	Applications . . . . .	76
5.5	Conclusions . . . . .	81
<b>6</b>	<b>The energy budget of the snowpack at Summit, Greenland</b>	<b>83</b>
6.1	Introduction . . . . .	84
6.2	Data . . . . .	85
6.3	The energy balance model . . . . .	86
6.4	Results and comparison with measurement data . . . . .	89
6.5	Discussion and conclusions . . . . .	98
<b>7</b>	<b>Spectral snow albedo and snow grain size</b>	<b>101</b>
7.1	Introduction . . . . .	102
7.2	Data and methods . . . . .	103
7.3	Results . . . . .	107
7.4	Discussion and conclusions . . . . .	113
	<b>Bibliography</b>	<b>115</b>
	<b>Dankwoord</b>	<b>123</b>
	<b>Curriculum vitae</b>	<b>125</b>
	<b>Publications</b>	<b>127</b>

## Samenvatting

Zonnestraling levert een belangrijke bijdrage aan de energiehuishouding van sneeuw- en ijsoppervlakken. Sneeuw heeft een hoog reflecterend vermogen, ook wel *albedo* genoemd. Een albedo van 1 betekent dat alle invallende zonnestraling wordt weerkaatst, een albedo van 0 betekent volledige absorptie. Het deel van de invallende zonnestraling dat wordt geabsorbeerd levert energie voor de opwarming en afsmelting van de sneeuw. Het albedo van sneeuw is erg hoog. Juist daardoor hebben kleine veranderingen in het albedo een groot effect op de hoeveelheid opwarming en afsmelting. Kennis van processen die het albedo beïnvloeden is daarom van groot belang. Met het onderzoek in dit proefschrift probeer ik bij te dragen aan een beter begrip van veranderingen in het albedo van sneeuw en ijs. De resultaten van dit onderzoek kunnen helpen de beschrijving van het albedo van sneeuw in klimaat- en massabalansmodellen te verbeteren.

Het albedo van sneeuw is niet gelijk voor alle golflengtes van het zonlicht: voor zichtbaar licht is het albedo meer dan 0,9: meer dan 90% van het zichtbare licht wordt weerkaatst. Voor golflengtes in het nabij-infrarood (boven 900 nm) is het albedo veel lager (0,05 tot 0,30). Om het gemiddelde albedo voor al het zonlicht te bepalen is het daarom van belang te weten hoeveel zonnestraling van welke golflengte aan het sneeuwoppervlak arriveert. In hoofdstuk 2 beschrijf ik daarom een model voor de berekening van stralingstransport door een atmosfeer die behalve absorberende gassen ook wolken en aerosolen kan bevatten. Dit stralingstransportmodel kan gebruikt worden om te berekenen hoeveel straling van welke golflengtes uiteindelijk bij een sneeuwoppervlak aankomt. Uit het bovenstaande volgt dat albedo geen eigenschap van het oppervlak is, maar veeleer afhangt van het stralingstransport in de gehele atmosfeer. Het model wordt gevalideerd aan de hand van nauwkeurige metingen onder een onbewolkte hemel. Deze metingen zijn verricht tijdens een periode met onbewolkt weer in Cabauw, een meetlocatie van het KNMI nabij Utrecht.

In hoofdstuk 3 beschrijf ik hoe aan het stralingstransportmodel een sneeuwlaag kan worden toegevoegd. Door aan de onderste lagen van de modelatmosfeer eigenschappen van sneeuw toe te kennen, kan de hoeveelheid invallende en gereflecteerde zonnestraling aan de bovenkant van een sneeuwlaag worden bestudeerd. Aan de hand daarvan wordt het albedo berekend. Modelresultaten bevestigen de theorie dat het albedo afneemt naarmate de zon hoger aan een onbewolkte hemel staat. Onder bewolkte omstandigheden heeft de zonnestraling die het oppervlak bereikt altijd ongeveer dezelfde hoek van circa 40° met het oppervlak, zodat het albedo dan niet langer afhankelijk is van de stand van de zon. De belangrijkste invloed

van bewolking is echter dat zij de spectrale samenstelling van het invallende zonlicht verandert: bewolking houdt juist die golflengtes van het zonlicht tegen waarvoor het albedo van sneeuw laag is. Als gevolg daarvan wordt het albedo gemiddeld over alle golflengtes hoger. Voorts laten modelresultaten zien dat een kleine concentratie van roetdeeltjes in de sneeuw het albedo danig verlaagt. Tot slot blijkt uit modelberekeningen dat sneeuw die bestaat uit grote sneeuw kristallen een lager albedo heeft dan sneeuw die bestaat uit kleine sneeuw kristallen. Omdat sneeuw kristallen groter worden naarmate ze meer energie absorberen, heeft dit de belangrijke implicatie dat een verandering van het albedo zichzelf versterkt: als het albedo afneemt, wordt meer zonnestraling geabsorbeerd, waardoor sneeuw kristallen kunnen groeien en het albedo verder afneemt. Zo'n proces dat zichzelf versterkt noemen we een positieve terugkoppeling.

In hoofdstuk 4 neem ik een aantal meerjarige meetreeksen van sneeuw albedo in verschillende delen van Antarctica onder de loep. Met het stralingstransportmodel onderzoek ik wat ruimtelijke en tijdsvariaties in het albedo van de sneeuw op Antarctica veroorzaakt. Het blijkt dat veranderingen in de grootte van de sneeuw kristallen veruit de grootste invloed hebben op veranderingen van het albedo. In het binnenland van Antarctica, waar het veel kouder is dan aan de kust, zijn sneeuw kristallen kleiner en het albedo is derhalve hoger. Aan de kust, maar ook in het binnenland neemt in de zomer de grootte van de sneeuw kristallen toe, zodat het albedo in de zomer lager is dan in de omliggende maanden. De invloed van de stand van de zon en van verschillen in de samenstelling van de atmosfeer blijkt beperkt.

Zoals in hoofdstuk 3 wordt aangetoond, heeft bewolking een grote invloed op het albedo van sneeuw: hoe dikker de bewolking, hoe meer het albedo toeneemt. Deze informatie kan worden gebruikt om met behulp van albedometingen onder onbewolkte en bewolkte omstandigheden de dikte van de bewolking te schatten. Hierbij gaat het niet om de fysieke dikte van een wolk, maar om haar optische dikte. Deze grootheid zegt iets over de doorlatendheid van wolken voor zonnestraling. Het blijkt dat de optische dikte van wolken een duidelijke correlatie vertoont met de langgolvlige straling (warmtestraling) die aan het oppervlak gemeten wordt. Omdat warmtestraling dag en nacht, en 's zomers en 's winters, gemeten kan worden, kan met behulp van die correlatie de optische dikte van bewolking geschat worden, zelfs als de zon niet schijnt. Metingen van weerstations op Groenland en Antarctica laten zien dat de optische dikte van bewolking afneemt naarmate de afstand tot de kust groter wordt. Bewolkte omstandigheden kunnen worden gescheiden van onbewolkte door te kijken naar de berekende optische dikte. Als we op die manier bewolkte en onbewolkte dagen apart bekijken, blijkt dat het albedo van sneeuw sterk toeneemt bij bewolking, overeenstemmend met de theorie en de modelresultaten van hoofdstuk 3. De optische dikte kan op dezelfde wijze worden bepaald boven een ijsoppervlak. Uit analyse van bewolkte en onbewolkte dagen komt naar voren dat het albedo van ijs niet wordt beïnvloed door bewolking.

Hoofdstukken 6 en 7 beschrijven metingen die in de zomer van 2007 zijn verricht nabij de wetenschappelijke basis Summit, op het hoogste punt van de Groenlandse ijskap. In hoofdstuk 6 doe ik verslag van metingen aan de energiebalans van de sneeuwlaag. Nadrukke-

lijk kijk ik naar de rol van zonnestraling in deze energiebalans. Hoogwaardige metingen van zonnestraling, warmtestraling en meteorologische grootheden worden gebruikt als invoer voor een model dat niet alleen de energiebalans van het sneeuwoppervlak berekent maar ook de temperatuurverdeling in de sneeuw. Een vergelijking van gemodelleerde met gemeten sneeuwtemperaturen leidt tot de hypothese dat zonnestraling die dieper in de sneeuw doordringt wezenlijk bijdraagt aan de opwarming van de sneeuw en de temperatuurverdeling in de sneeuwlaag: zonder deze stralingspenetratie op te nemen in het energiebalansmodel, kunnen gemeten sneeuwtemperaturen niet gereconstrueerd worden. Metingen aan de grootte van de sneeuw kristallen worden gebruikt om ook door het stralingstransportmodel het effect van stralingspenetratie te laten berekenen. De resultaten van deze berekeningen komen vrij goed overeen met de resultaten van het energiebalansmodel. Ten slotte wordt aangetoond dat zonnestraling veruit de belangrijkste bron van energie is voor de opwarming van het sneeuw pakket. Deze toevoer van energie wordt voornamelijk gecompenseerd door netto uitstraling van warmte, door opwarming van de sneeuw, door koeling van het sneeuwoppervlak door wind, en door sublimatie van sneeuw.

In hoofdstuk 7 worden tot slot metingen van het albedo van sneeuw voor verschillende golflengtes geanalyseerd en vergeleken met modelberekeningen. In eerdere literatuur konden modelberekeningen alleen in overeenstemming worden gebracht met waarnemingen door te veronderstellen dat zich een zeer dun laagje van kleine sneeuw kristallen in de bovenste millimeter van de sneeuw laag bevond. In dit hoofdstuk laat ik met behulp van een stereografische analyse van digitale foto's van sneeuw monsters voor het eerst zien dat deze dunne laag ook inderdaad aanwezig is. De theorie van stralingstransport boven en in een sneeuw laag wordt hierdoor versterkt.



## Summary

Solar radiation is an important component of the energy budget of snow and ice surfaces on glaciers and ice sheets. Snow has a high reflectivity, also known as the *albedo*. A surface having an albedo of 1 reflects all incident solar radiation. On the other hand, an albedo of 0 implies complete absorption. The absorbed part of the incident solar radiation provides energy for heating and melting of the snowpack. The albedo of snow is very high. Exactly for that reason, small changes in its value have a large impact on the amount of heating and melt. It is therefore important to gain knowledge of processes that influence the albedo. In this dissertation, a better understanding of the variability and changes of the albedo of snow and ice surfaces is pursued. The results of this research can help to improve parameterizations of snow and ice albedo in climate and mass balance models.

The albedo of snow and ice is highly variable with the wavelength of solar radiation: albedo is higher than 0.9 in the visible part of the spectrum: more than 90% of the incident visible radiation is reflected. The albedo for near-infrared radiation (wavelengths over 900 nm) is much lower, at 0.05 to 0.30. In order to determine the broadband albedo accurately, it is therefore important to know how much radiation of a certain wavelength arrives at the snow (or ice) surface. For that purpose, I present a radiative transfer model in chapter 2. This model computes radiative transfer through an atmosphere that not only contains absorbing gases, but also clouds and aerosols. It calculates how much radiation of a particular wavelength arrives at the surface. One can conclude from the above, that the albedo is not an inherent property of the surface. Rather, it depends on radiative transfer in the entire atmosphere. The model is validated using detailed clear-sky measurement, performed during a period of cloudless weather in Cabauw, The Netherlands.

In chapter 3, a snowpack is added to the radiative transfer model. By assigning snow optical properties to the lowermost model layers, the amount of incident and reflected solar radiation at the top of the snowpack can be studied, and the albedo can be determined. Model results confirm the established theory that albedo decreases as the sun stands higher above the horizon in a clear sky. During cloudy conditions, this dependence of albedo on the solar zenith angle vanishes since solar radiation at the surface always has an effective zenith angle of about  $50^\circ$  in the presence of cloud cover. The most important effect of clouds is however their ability to alter the spectral composition of the incident solar radiation: clouds absorb exactly the radiation of wavelengths for which the albedo of snow is low. As a result, the broadband albedo increases. Furthermore, model results show that a small concentration of

soot particles significantly lowers the albedo of the snowpack. Lastly, model calculations show that snow consisting of large snow grains has a lower albedo than snow consisting of small snow grains. At the same time, snow grains are known to grow as they absorb more energy. This has the important implication that a change in albedo amplifies itself: when the albedo decreases, more solar radiation is absorbed, causing snow grains to grow and the albedo to decrease further. Such a self-amplifying process is called a positive feedback.

In chapter 4, I study several multi-year series of snow albedo observations from various parts of Antarctica. Using the radiative transfer model, it is assessed which processes drive the spatial and temporal variability in snow albedo in Antarctica. It turns out that changes in snow grain size have by far the largest impact on variations of snow albedo. On the Antarctic Plateau, where temperatures are much lower than in the coastal regions, snow grains are smaller and albedos higher. In coastal as well as inland regions, snow grain size is larger in the summer months, resulting in reduced snow albedos compared to the spring and autumn months. The impact of variations of solar zenith angle and atmospheric composition are of limited importance.

As demonstrated in chapter 3, cloud cover has a prominent influence on the albedo of snow. The increase of snow albedo with respect to clear-sky conditions is proportional to the optical thickness of the cloud cover. This observation can be used to infer cloud optical thickness from measurements of albedo under clear and cloudy conditions. It turns out that cloud optical thickness and the amount of longwave (thermal) radiation arriving at the surface are clearly correlated. Longwave radiation is recorded both day and night, and both in summer and winter, so the cloud optical thickness can be determined using this correlation, even in the absence of solar radiation itself. Data from weather stations on the Greenland and Antarctic ice sheets reveal that cloud optical thickness decreases away from the coast. Cloudy conditions can be separated from clear-sky conditions using computed cloud optical thickness. By separately studying clear and cloudy periods, snow albedo turns out to increase strongly in the presence of clouds, conforming with theory and with the model results from chapter 3. In the same way, optical thickness can be determined above ice surfaces. Analysis of clear and cloudy days reveals that ice albedo is *not* influenced by the presence of clouds.

Chapters 6 and 7 deal with a measurement campaign carried out at the scientific base at Summit, Greenland, in the summer of 2007. The Greenland Environmental Observatory at Summit is located near the highest point of the Greenland ice sheet. In chapter 6, measurements of the energy budget of the snowpack are presented, focussing on the role of solar radiation. State-of-the-art measurements of solar and thermal radiation, as well as meteorological variables, are used as input for an energy balance model that also computes the temperature distribution within the snowpack. A comparison between modelled and observed snow temperatures suggests that subsurface absorption of penetrated solar radiation contributes significantly to the warming of the snowpack and to its temperature distribution: observed snow temperatures cannot be simulated when the radiation penetration term is omitted from the energy balance. Observations of snow grain size profiles are prescribed in the radiative transfer

model to compute the effect of radiation penetration. The results of these calculations agree reasonably well with the results from the energy balance model. Furthermore, we show that shortwave radiation is by far the most important source of energy for heating of the snowpack. The energy budget is closed by net emission of longwave radiation, by heating of the snowpack, and by net negative sensible and latent heat fluxes.

In the final chapter, observations of spectral snow albedo are analysed and compared with spectral radiative transfer calculations. In previous literature, the presence of a submillimeter layer of small snow grains had to be assumed to achieve agreement between model calculations and field observations of spectral snow albedo. In this chapter, stereographic analysis of snow grain images shows, for the first time, that this submillimeter layer is actually present in natural snow, reinforcing the theory of radiative transfer in and over a snow layer.



# Snow, ice and climate

## 1.1 The role of solar radiation in the climate system

Climate on Earth is, to a large extent, driven by the radiation it receives from the Sun. The energy required for many climatic processes on Earth is ultimately provided by solar radiation.

Solar radiation heats the atmosphere, the land and the oceans. However, the amount of solar radiation is not distributed evenly over the globe. Due to the spherical geometry of the Earth, the radiative energy of a beam of solar radiation is spread over a larger surface area in the polar regions than around the equator. As a consequence, there is more solar radiation available at the equator than at the poles, and thus, the equatorial region is heated more than the polar regions. With respect to the global average, there is an excess of heat at the equator, and a deficit near the poles. A continuous poleward transport, both by the oceans and by the atmosphere, attempts to cancel this imbalance. The exact relative contribution of oceanic and atmospheric transport has been debated for decades, but they are of the same order of magnitude.

The atmospheric poleward transport of air and heat is affected by the rotation of the Earth, leading to some characteristic climatic phenomena. At tropical and subtropical latitudes (roughly between  $30^{\circ}\text{N}$  and  $30^{\circ}\text{S}$ ), it gives rise to the Hadley circulation. In this circulation, air ascends in a band region known as the intertropical convergence zone, characterized by the formation of large convective clouds and vigorous vertical mixing of the atmosphere. The migration of the intertropical convergence zone is dictated by the seasonal oscillation of the solar zenith point around the equator, and causes distinctive dry and wet seasons in the tropics. The air aloft is transported poleward, before descending over the subtropics. As the air moves downward, the air is heated adiabatically, which suppresses the formation of clouds and precipitation. Arid regions are therefore found around  $30^{\circ}\text{N}$  and  $30^{\circ}\text{S}$ . To close the circulation in the Hadley cell, air is transported back to the tropics at the surface by the trade winds. At middle latitudes, the interplay between atmospheric poleward transport and the Earth's rotation leads to the formation of large low- and high-pressure systems that govern weather and climate in temperate regions.

The relative energy deficit at the poles due to the Earth's geometry is amplified by the presence of snow and ice, that cover large parts of the Earth's polar regions. Snow and ice surfaces in polar regions act as large 'mirrors' for solar radiation, and reflect most of it back to space. As a consequence, the amount of energy absorbed by the climate system is reduced even more than from geometric considerations only.

The extent of snow and ice cover on Earth is considerable, and consists of large continental ice masses (ice sheets) as well as vast expanses of frozen ocean (sea ice). On the Northern Hemisphere, the Arctic Ocean occupies most of the area north of the Polar Circle. About 5 to 7 million km<sup>2</sup> of the Arctic Ocean is covered with multi-year sea ice that survives throughout the year. In winter, sea-ice cover increases to 15 to 17 million km<sup>2</sup> (for reference, the land surface area of Europe is approximately 10 million km<sup>2</sup>). Furthermore, the Northern hemisphere features the Greenland ice sheet, which has an area of 1,700,000 km<sup>2</sup> and a volume of 2,900,000 km<sup>3</sup> (a potential sea-level rise of 7.3 m). On the Southern Hemisphere, the Antarctic Ice Sheet occupies an area of 12,300,000 km<sup>2</sup> and has a volume of 24,700,000 km<sup>3</sup> (potential sea-level rise of 56.6 m). At approximately 3 million km<sup>2</sup>, the area of multi-year sea ice around Antarctica is much smaller than its Northern Hemisphere counterpart. In winter, sea-ice cover at the Southern Hemisphere increases to ~19 million km<sup>2</sup>.

As discussed above, these vast areas of snow and ice reduce the amount of energy that enters the climate system in the polar regions, leading to a lower surface temperature. Thanks to these low temperatures, snow and ice can continue to exist. In other words, ice sheets and sea ice partly sustain their own presence. There is thus a very tight connection between solar radiation and climate in polar regions, owing to the presence of snow and ice. It will not come as a surprise that snow and ice have been playing a crucial role in the history of Earth's climate. Before we can discuss the role of snow and ice in past and present climate however, we will need to better understand their optical properties.

## 1.2 The albedo of snow and ice

The fraction of solar radiation that is reflected by a surface is referred to as *albedo*, denoted by  $\alpha$ . An albedo of 0.4 means that 40% of the incident solar radiation is reflected. The remaining 60% is absorbed by the surface. Snow and ice surfaces generally have a high albedo, ranging from 0.4 for ice to 0.9 for clean and fresh dry snow. A list of the typical albedo for different surfaces is shown in table 1.1. It is apparent that most snow and ice surfaces have a much higher albedo than other surface types.

Snow and ice albedo depend on many factors, which will be discussed extensively in chapters 3 and 4. One of the most important factors for snow albedo is the size of the snow grains that constitute the snowpack. Snow grains constantly evolve under the influence of temperature and temperature gradients in the snow [Flanner and Zender, 2006], a process which is referred to as snow metamorphism. The effective size of the snow grains tends to

**Table 1.1:** Typical values for the albedo of different surface types occurring on Earth.

Surface type	Albedo	
	min	max
Fresh snow	0.80	0.90
Aged snow	0.70	0.80
Firn	0.43	0.69
Clean glacier ice	0.34	0.51
Dirty glacier ice	0.15	0.33
Ocean water	0.03	0.25
Bare rock	0.15	0.30
Grassland	0.16	0.20

increase over time. As we will see in chapter 3, these larger snow grains scatter incoming solar radiation deeper into the snowpack, increasing the chance that radiation gets absorbed on its path. The albedo of the snow decreases as a result. There is thus a potentially strong positive feedback mechanism in which absorbed solar radiation increases snow temperature, leading to faster metamorphism, which in its turn lowers the albedo so that even more solar radiation is absorbed. High-albedo surfaces in particular are sensitive to small changes in the albedo. Suppose that the albedo of a surface drops from 0.90 to 0.85. The amount of absorbed radiation then increases by 50%. In other words, the amount of absorbed radiation increases rapidly when the albedo of a high-albedo surface is lowered.

A similar albedo-related feedback mechanism is that of disappearing snow cover on glaciers and ice sheets. Glaciers and ice sheets consist of a large body of ice, covered with a layer of snow. In the ablation zone of a glacier or ice sheet, the snow cover eventually disappears during the summer melt season, exposing the underlying glacier ice. As shown in table 1.1, glacier ice has a lower albedo than snow. As a result, more solar radiation is absorbed, leading to more melt, and thus removal of more mass from the glacier surface. The onset and duration of snow and ice melt in spring and summer, determined largely by air temperature and the amount of solid precipitation, is important for the mass balance of glaciers and ice sheets.

A third feedback mechanism dealing with albedo is that of a debris feedback on glaciers. Recently, it has been observed that the albedo in the ablation zones of mountain glaciers decreases due to an increasing dust and debris content of the surface ice [Oerlemans *et al.*, 2009]. Retreating glaciers leave behind a dry and barren forefield, dust and debris of which is advected onto the glacier surface. The albedo of the ice surface drops, the melt rate increases, and the glacier retreats faster.

In general, this positive feedback mechanism is referred to as the albedo-mass balance feedback. On one hand, this feedback ensures that ice sheets and sea ice can be maintained by

their own presence. On the other hand, relatively small changes in the local climate, for example a temperature increase, can lead to a rapid decay of such ice bodies. Past climate variations have thus been dictated by snow- and ice-related feedbacks, as we will discuss in the next section. In section 1.4, attention will be given to present-day climate change, and its impacts on snow and ice in polar regions.

### 1.3 Snow and ice in past climate

Both from geological evidence and from major ice coring efforts, it is now known that snow and ice have played a very important role throughout the history of the Earth. Presumably, there have been episodes in which almost all of the Earth was covered with snow and ice, and the oceans were frozen. These conditions, referred to as a ‘Snowball Earth’, supposedly occurred once to a few times in the Neoproterozoic era between 1,000 and 542 million years (Myr) ago. The possibility of a Snowball Earth was first discussed by *Budyko* [1969], and elaborated by e.g. *Hoffmann et al.* [1998]. It is hypothesized that once sea-ice cover had crossed a certain latitude, the feedback between temperature and snow and ice cover would bring the Earth climate in a runaway state in which the entire globe is covered with snow and ice. With photosynthesis and ocean carbon uptake being shut down, carbon dioxide produced during volcanic eruptions could reach extremely high levels over the course of tens of millions of years. The heat trapped by this intense greenhouse eventually led to the meltdown of the Snowball Earth. Possibly, the Snowball Earth was able to develop due to a weaker sun, a larger tilt of the Earth’s rotation axis, a favourable configuration of the continents, or a combination of these. One can imagine that a full-blown Snowball Earth would have had far-reaching consequences for the development of life on Earth. For that and other reasons, there is some dispute amongst scientists about the occurrence and extent of the Snowball Earth episodes. Geological evidence in support of the Snowball Earth hypothesis might not be thoroughly convincing, and could also be an indication for some intermittent glaciation at lower latitudes, without entirely frozen oceans [*Allen and Etienne*, 2008].

The most recent (semi-)permanent glaciation of the Antarctic continent is believed to have started about 34 Myr ago during the Oligocene-Eocene transition [*Zachos et al.*, 2001]. The Antarctic ice sheet appears to have been in place continuously from about 16 Myr ago up to the present day. Glaciation of Greenland and the Northern hemisphere is thought to have started about 2.7 Myr ago, in the Pleistocene. Glacial and interglacial periods have occurred alternatingly up to the present day, initially in cycles of  $\sim 40,000$  years but later of  $\sim 100,000$  years [*Bintanja and Van de Wal*, 2008].

The occurrence of Pleistocene glacials and interglacials is closely linked to small cyclical aberrations in the orbit of the Earth around the Sun. In 1930, Milutin Milanković published his book *Mathematische Klimalehre und Astronomische Theorie der Klimaschwankungen*, in which he presents and substantiates the theory that small variations in the amount and

timing of incoming solar radiation (insolation) are the driver of climatic fluctuations on Earth [Milanković, 1930]. These fluctuations are caused by quasi-periodical variations in three orbital parameters, now known as Milanković cycles: orbital shape (eccentricity), axial tilt (obliquity) and axial rotation (precession). Each of these orbital variations acts on a different time scale, causing them to amplify or dampen each other in an irregular fashion.

Milanković suggested that the summer insolation at  $65^{\circ}\text{N}$  is the pacemaker for the Pleistocene ice ages. Large continental land masses are present around that latitude, on which a snow cover can easily develop, and on which large ice sheets can be sustained. Although the variations in summer insolation have a small magnitude of a few  $\text{W m}^{-2}$ , strong positive feedbacks involving snow and ice cover cause large ice masses to develop on the Northern Hemisphere. In summer, these feedbacks are strongest, as the largest amount of radiation is available. If summer insolation is reduced, the summer snow cover extent remains larger and temperatures remain lower, favouring the build-up of large ice sheets. The albedo-mass balance feedback ensures that the mass balance remains positive. The ice sheet can grow, so that its surface reaches a higher altitude at which temperatures are lower. Although not directly an albedo feedback, this height-mass balance feedback is initiated by the albedo-mass balance feedback. Milanković' theory was finally supported by observational evidence from deep-sea sediment cores [Hays *et al.*, 1976], some 45 years after the publication of his book. Maxima in the concentration of the  $^{18}\text{O}$  isotope in these cores, telling of lower temperatures and larger ice masses, indeed turned out to coincide with minima in summer insolation at  $65^{\circ}\text{N}$ .

## 1.4 Present-day climate change

Up until the industrial revolution about 200 years ago, we can be certain that variations in climate had natural causes. Combustion of fossil fuels has since then led to an unprecedentedly rapid increase in atmospheric concentrations of carbon dioxide ( $\text{CO}_2$ ) and other greenhouse gases like methane ( $\text{CH}_4$ ). Atmospheric  $\text{CO}_2$  concentrations have increased from 280 ppm in the pre-industrial era (1000–1750 AD) to 388 ppm in 2008, an increase of almost 40%. As greenhouse gases are transparent to solar radiation but opaque for heat emitted by the Earth, it won't be difficult to understand that the observed recent warming at the Earth's surface is very likely due to anthropogenic emissions of greenhouse gases, in line with findings from the most recent assessment of the Intergovernmental Panel for Climate Change [IPCC, 2007]. In an interesting modelling experiment, the evolution of global climate during the last century is simulated with and without forcing from anthropogenic emission of greenhouse gases and aerosols. Figure 1.1, containing the results of this experiment, convincingly shows that current global warming (1950 to present) can no longer be explained by natural climate variability [IPCC, 2007]: beyond 1950, the model runs that do not take into account anthropogenic forcings start to deviate significantly from the observed globally-averaged temperature trend.

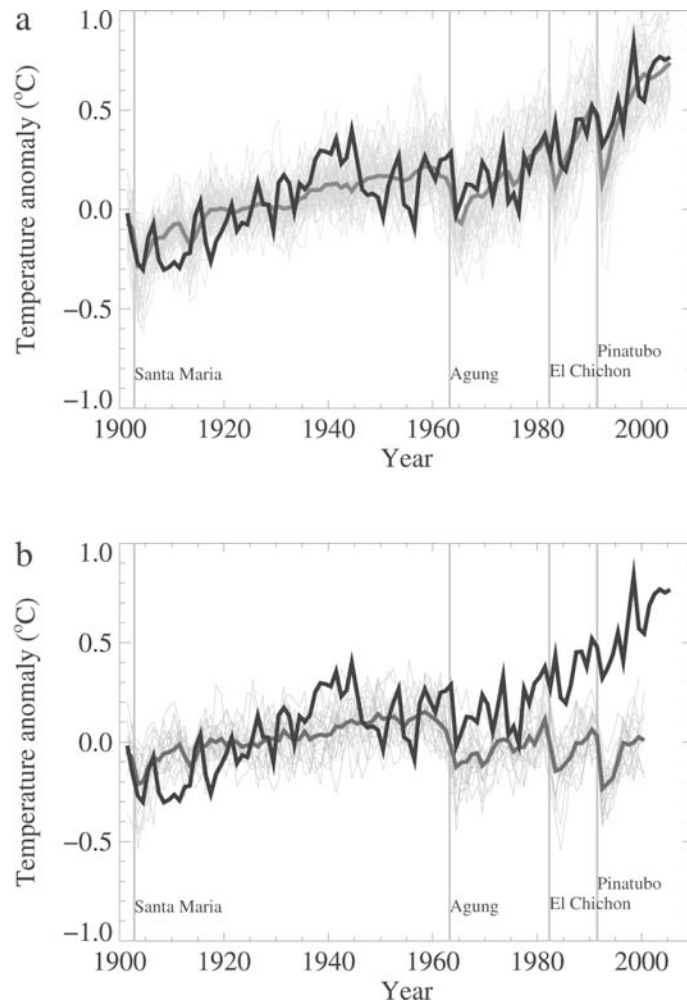


**Figure 1.1:** Comparison between global mean surface temperature anomalies from observations (black lines) and general circulation model simulations forced with (a) both natural and anthropogenic forcings, and (b) only natural forcings. In both figures, results from an ensemble of model runs are presented. The individual ensemble members are represented by the thin lines, and the ensemble average by the thick gray lines. Also shown are the timing of major volcanic eruptions in the 20<sup>th</sup> century, depicted by the vertical gray bars. Figure taken from the IPCC Fourth Assessment Report [IPCC, 2007, chapter 9, figure 9.5]

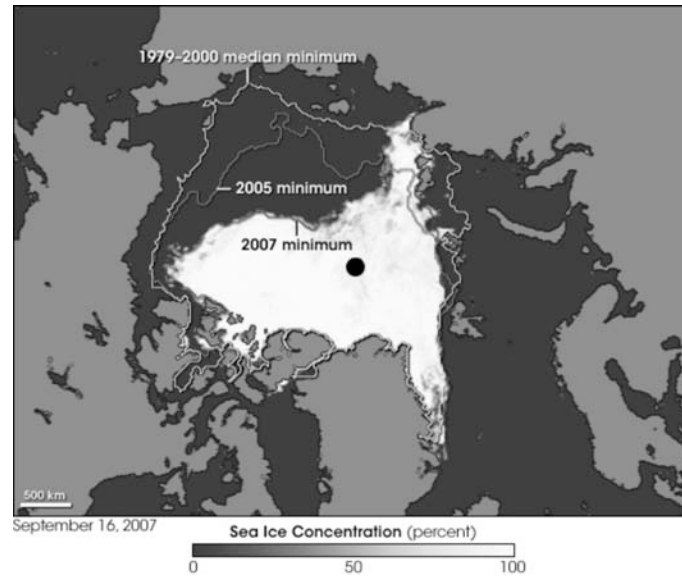


**Figure 1.2:** Image of the minimum sea-ice extent and concentration in the Arctic Ocean. Shown are the 2005 and 2007 minima, as well as the 1979–2000 median minimum annual sea-ice extent. Image taken from <http://www.nsidc.org>, National Snow and Ice Data Center, USA.

As a consequence of the current warming, snow and ice are disappearing at significant rates. The disappearance of snow and ice enables more absorption of solar radiation in the climate system, leading to an enhanced temperature increase and further melt. Sea-ice extent over the Arctic Ocean has shrunk significantly in the past 25 years. Figure 1.2 shows the record minimum sea-ice extent from September 2007 (4.30 million km<sup>2</sup>) compared to the median minimum sea-ice extent between 1979–2000 (7.04 million km<sup>2</sup>). In the case of sea ice, there is a particularly strong albedo feedback mechanism, since sea ice (albedo  $\sim 0.5$ – $0.7$ ) is replaced by open ocean (albedo  $< 0.1$ ). Moreover, the heated surface layer of the water in the Arctic Ocean can flow under the ice and enhance melt of sea ice from below. Multi-year Arctic sea ice is projected to have disappeared by the end of the 21<sup>st</sup> century [Boé *et al.*, 2009].

Higher temperatures also affect the surface mass balance of the Greenland Ice Sheet (GIS). The occurrence and properties of the snowpack on the GIS are very sensitive to climate change. The areal extent of the GIS experiencing melt, detected by passive microwave sensors aboard satellites, has increased in the past decades [Fettweis *et al.*, 2007]. A warmer atmosphere delivers more heat to the snow and ice, leading to more rapid snow metamorphism, and a more intense and prolonged melt season. More rapid snow metamorphism leads to lower albedo, more absorption of solar radiation and thus an earlier removal of snow in the ablation zone of the GIS: the albedo-mass balance feedback is obvious here. A regional

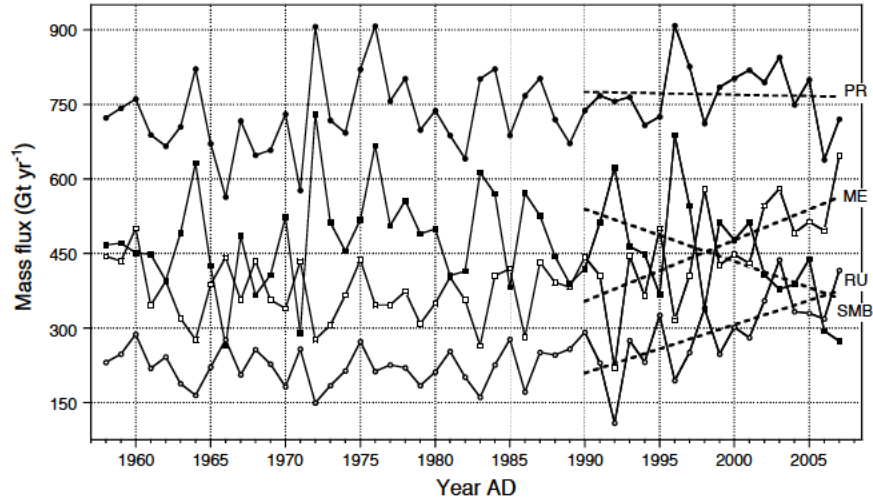


**Figure 1.3:** Model output of surface mass balance (SMB, open circles), precipitation (PR, solid circles), melt (ME, open squares) and runoff (RU, solid squares), integrated over the entire ice sheet for the period 1957–2008, expressed in  $\text{Gt yr}^{-1}$ . Dotted lines indicate linearly fitted trends for the period 1990–2008. Data and figure from Ettema *et al.* [2009], using the RACMO2/GRN model.

climate modelling study by Ettema *et al.* [2009] shows that the amount of melt over the GIS has increased in the last few decades, making the surface mass balance less positive (figure 1.3).

With an decrease in sea-ice extent, an increase in ice sheet melting, and a seasonal snow cover that gets smaller and lives shorter (a process that we have not discussed here), the observed and predicted change in surface temperature in polar regions is understandably larger than the global average. This observed polar amplification is thus due to strong feedbacks related to snow and ice albedo.

## 1.5 Modelling snow and ice albedo

Models of varying complexity are used to reconstruct past climate, simulate current climate and predict future climate. Mass and energy balance models are used to reconstruct and predict changes in the mass and energy balance of glaciers and ice sheets. In all of these models, climatic variables have an influence on snow and ice cover, and vice versa, the presence of snow and ice has an impact on the local climate. These modeling studies cover a wide range of time scales, from day-to-day reanalysis runs of present climate to multi-million year palaeoclimatic reconstructions. For all applications, care should be taken to correctly incorporate

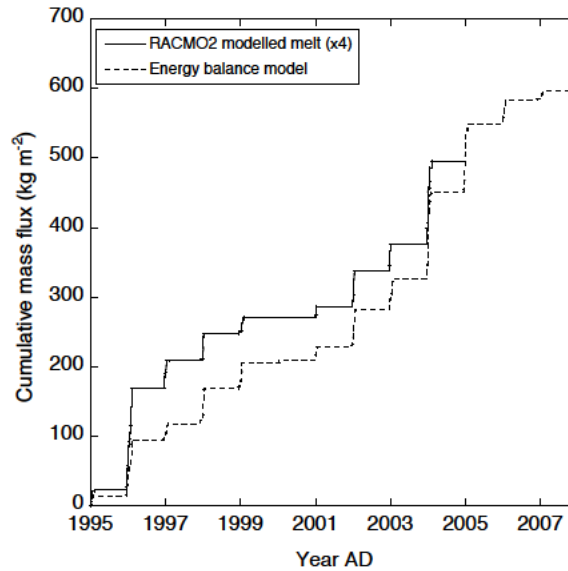


**Figure 1.4:** Comparison of meltwater fluxes at Neumayer station, East Antarctica as modelled with an energy balance model (dashed line) and modelled using RACMO2/ANT (solid line), between 1995 and 2008. Note that the solid line is multiplied by a factor 4.

the albedo of snow and ice surfaces, especially because of the sensitive positive feedback mechanisms in which snow and ice surfaces are usually involved. Ideally, a detailed snow metamorphism model should thus be coupled to a climate model to correctly prescribe snow albedo and albedo-related feedbacks. However, this is rarely done, either for computational or practical reasons. Instead, the effects of snow metamorphism are usually approximated using variables like surface temperature, which is readily available as a prognostic variable in climate models.

An example that demonstrates the importance of a correct representation of snow albedo is the calculation of meltwater fluxes on the Antarctic continent using the regional atmospheric climate model RACMO2/ANT [Van den Berg *et al.*, 2006]. From observations and energy balance modelling, we know that snow albedo tends to drop when liquid water is present in the surface snow [Van den Broeke *et al.*, 2009]. This induces a positive feedback, as more solar radiation becomes available for the production of even more meltwater. The albedo parameterization in RACMO2/ANT does not capture the dependence on liquid water content [Reijmer *et al.*, 2005] and the model thus misses this positive feedback. As a result, the

estimate of meltwater production will be too small at locations where surface temperature exceeds the melting point. In figure 1.4, it is shown that at Neumayer station, a coastal station in East Antarctica, meltwater production computed by RACMO2/ANT is underestimated by a factor of 4 [Van den Broeke *et al.*, 2009].

In an increasing number of studies, global or regional climate models are coupled to an ice sheet model in order to study the effects of climate change on ice sheets, and to assess the role of ice sheets in climate. Furthermore, regional climate models are employed to compute energy and mass balance histories of ice sheets. A potential problem in these applications is that the model grid resolution hardly exceeds the typical width of the ablation zone of an ice sheet, which is in the order of a few tens of kilometres. The albedo-mass balance feedback is likely to be poorly captured. For sea ice, the correct representation of positive feedback mechanisms is challenged in a similar fashion, due to low grid resolution. However, these problems are not addressed in this thesis.

Improvement of snow and ice albedo representations in models requires a good knowledge of the processes that influence albedo. Improving knowledge about snow and ice albedo, and about the interaction between solar radiation and snow and ice surfaces in general, is the main motivation for the research presented in this thesis. In this thesis, I will combine a model for the albedo of snow with measurements from several locations in Greenland and Antarctica. In the summer of 2007, an experiment dedicated to the radiation and energy budget of polar snow was carried out in Greenland, from which results are used in this thesis. A summary of this experiment is given in the next section.

## 1.6 The Summit Radiation Experiment (SURE '07)

In chapters 6 and 7, results from the Summit Radiation Experiment (SURE '07) are analyzed and presented. This glaciometeorological experiment was set up in order to get more insight into the radiation and energy balance of a polar ice sheet surface. In particular, the influence of snow microstructure on the optical properties of the snowpack was studied, as well as the role of solar radiation and albedo in the energy budget of the snowpack.

SURE '07 took place in June and July 2007 at the Greenland Environmental Observatory at Summit, Greenland. Summit is located very close to the highest point of the Greenland Ice Sheet at an altitude of 3209 m a.s.l. Its coordinates are 72°34' N, 38°28' W, shown on the map in figure 1.5. Dominant winds are from the southwest and south, and of rather weak katabatic nature. Research at this location started in 1989 with the retrieval of the GISP2 ice core, and ever since, the station has hosted a wide range of research in the fields of polar meteorology, ice coring and atmospheric and snow chemistry.

During the experiment, which was in full operation for 42 consecutive days, wind speed, wind direction, air temperature, air pressure and relative humidity were measured continuously

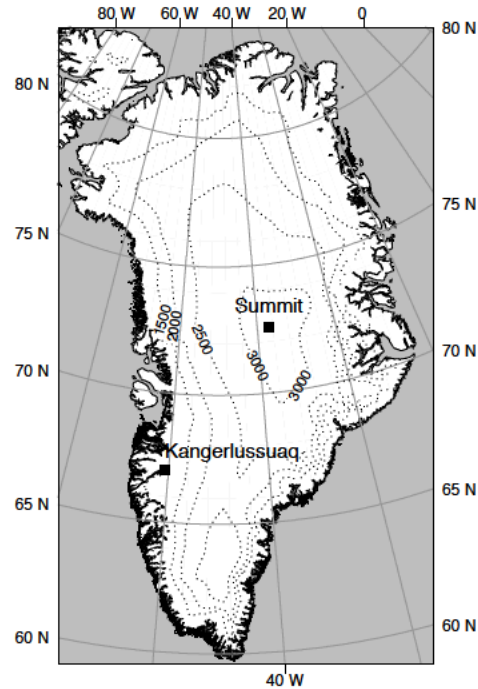


**Figure 1.5:** Location of the Greenland Environmental Observatory at Summit, Greenland. Also shown is the location of Kangerlussuaq. Height contours are shown in 500 m intervals, in m a.s.l.

using a single-level automatic weather station (AWS), shown on the uppermost panel in figure 1.6. On the AWS, a sonic anemometer was installed measuring turbulent fluxes of sensible heat. Furthermore, snow depth and snow temperatures at 10 levels were measured using thermocouples (at depths of 2, 4, 6, 8 and 10 cm) and thermistors (at 20, 30, 50, 75 and 100 cm). Short- and longwave radiation were measured using a wide array of pyrano- and pyrgeometers on a separate radiation mast (middle panel in figure 1.6). Also, diffuse radiation was measured with a pyranometer equipped with a shadow ring. Among the pyranometers were nine pairs of sensors that measured solar radiation in particular wavelength bands that correspond to various satellite bands of currently operational satellites. Cloud observations were done by a skyward-facing digital camera and a Total Sky Imager. Lastly, albedo spectra were recorded under clear and cloudy conditions using a spectroradiometer, shown in the lower panel of figure 1.6.

As the snow microstructure is of importance to the shortwave optical properties of the snow surface, a part of the experiment was dedicated to sampling of the surface snow. During the experiment, we collected five pairs of snow samples in 5 to 6-day intervals. The snow was cast in a solution of dyed diethyl phthalate to prevent further snow metamorphism. The frozen

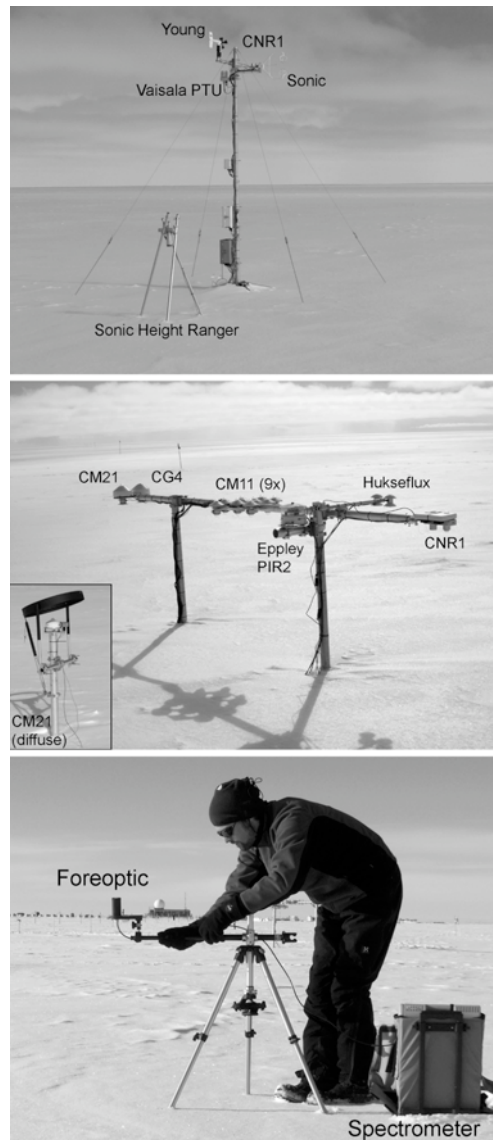


**Figure 1.6:** Top: The automatic weather station deployed during SURE '07 (Young = wind speed and direction monitor, CNR1 = shortwave and longwave radiation, Vaisala PTU = temperature, pressure and humidity, Sonic = sonic anemometer). Middle: Radiation setup (CM21 = shortwave radiation, CG4 = longwave radiation, CM11 (9 $\times$ ) = narrowband pyranometers, Eppley PIR2 = incoming longwave radiation, Hukseflux = short- and longwave radiation, CNR1 = short- and longwave radiation). The inset shows a setup for diffuse radiation using a CM21 pyranometer and a shadow ring. Bottom: Spectroradiometer setup.

samples were transported to the cold laboratory of the Institute for Snow and Avalanche Research in Davos, Switzerland, and cut into thin slices. Applying stereological methods to digital photographs of these sections yields a measure for snow grain size in the snowpack.

## 1.7 This thesis

In this thesis, radiative transfer modelling in the atmosphere and the snowpack has been combined with field observations to learn more about the role of snow, ice and clouds in the solar radiation budget of glaciers and ice sheets.

In **chapter 2**, a radiative transfer model is introduced for accurate computation of shortwave radiative transfer in the snow-atmosphere system. The originally monochromatic model is modified for calculations in the entire solar spectrum using the so-called correlated- $k$  technique. The details of this model adaptation are documented in this chapter, and the broadband radiative transfer model is validated using both a model intercomparison and a comparison between model calculations and observations of solar radiation made in Cabauw, The Netherlands.

**Chapter 3** describes how the model presented in the previous chapter is extended with the possibility to include snow and cloud layers. In a series of model experiments, the influence on snow characteristics, solar elevation, and clouds on the albedo of a snow surface is demonstrated.

In **chapter 4**, the model presented in chapters 2 and 3 is applied to solar radiation data that were collected by automatic weather stations in Antarctica between 1998 and 2001. Using the radiative transfer model, the attribution of several processes to variations in snow surface albedo is investigated.

Clouds have a considerable impact on the radiation balance of the snow surface, depending on their optical thickness. Using concurrent observations of incoming solar radiation and albedo from different measurement locations in Greenland and Antarctica, a technique to retrieve cloud optical thickness is presented in **chapter 5**.

**Chapter 6** deals with the energy budget of the snowpack, particularly focusing on solar radiation that penetrates into the snow and causes subsurface heating as it is absorbed below the surface. Meteorological and radiation observations made during SURE '07 are used in a model that reconstructs the energy budget of the snow. Radiative transfer model calculations are used to investigate the role of radiation penetration.

This thesis is concluded with **chapter 7**, in which concurrent observations of the structure and spectral albedo of the snow surface during SURE '07 are combined and compared to model calculations. This chapter shows the effect of the structure of the uppermost snow layer on the optical properties of the snowpack.



## Broadband radiative transfer

### Summary

Using the correlated  $k$ -distribution method for gaseous absorption, the originally monochromatic doubling-adding radiative transfer model DAK (Doubling Adding KNMI) has been adapted for calculations of broadband atmospheric radiative transfer. The model can now calculate the solar broadband irradiances reflected and transmitted by the atmosphere, as well as the internal irradiances within the atmosphere. In a model intercomparison study, DAK broadband diffuse and direct irradiances agree well with results from the parameterized radiative transfer model SMARTS (Simple Model for Atmospheric Radiative Transfer of Sunshine). Agreement is best for a purely Rayleigh-scattering atmosphere, with maximum 1% difference for direct irradiance, and 3.5% for diffuse irradiance. In an atmosphere containing aerosols, model difference is less than 1% for direct irradiance, but slightly larger for diffuse irradiance (approximately 6%), presumably due to the parameterization in SMARTS. It is very important to treat the aerosol optical properties dependent on wavelength in DAK. By doing so in a radiative closure study at the site of Cabauw, The Netherlands, excellent closure was obtained for 72 cases of clear-sky global (+0.3% mean deviation), direct (+0.8%) and diffuse (+0.2%) irradiance.

---

This chapter is based on (1) Kuipers Munneke, P., C. H. Reijmer, M. R. van den Broeke, P. Stammes, G. König-Langlo and W. H. Knap (2008), Analysis of clear-sky Antarctic snow albedo using observations and radiative transfer modeling, *J. Geophys. Res. (D)*, **113**, D17,118, doi:10.1029/2007JD009653. (2) Wang, P., W. H. Knap, P. Kuipers Munneke and P. Stammes (2008), Clear-sky atmospheric radiative transfer: a model intercomparison for shortwave irradiances, in *IRS 2008: Current problems in atmospheric radiation*. (3) Wang, P., W. H. Knap, P. Kuipers Munneke and P. Stammes (2009), Clear-sky shortwave radiative closure for the Cabauw Baseline Surface Radiation Network site, the Netherlands, *J. Geophys. Res. (D)*, **114**, D14,206, doi10:1029/2009JD011978.

## 2.1 Introduction

This thesis is devoted to the subject of radiative transfer of sunlight in the snow-atmosphere system. In this chapter, we will lay out the physical framework for a model that describes radiative transfer of sunlight in a clear-sky atmosphere. This is the first important ingredient for a proper description of radiative transfer in an atmosphere that contains clouds, and is bounded below by a snow surface.

We will start with introducing single-scattering properties of a volume element in the atmosphere (section 2.2). As the atmosphere consists of many scatterers (particles, aerosols, clouds), we will extend the theory of single scattering to multiple scattering in section 2.3. In section 2.4, we will present the technique of *doubling-adding* as a numerical method to compute multiple scattering in atmospheric radiative transfer.

The optical properties of the atmosphere differ widely for different wavelengths. For a proper description of broadband solar radiation in the snow-atmosphere system, it is therefore necessary to take into account this wavelength dependence. The doubling-adding method is therefore extended with the correlated- $k$  method for the efficient computation of broadband radiative transfer of sunlight in the atmosphere. This is treated in section 2.5. The implementation of the correlated- $k$  method is verified in a model intercomparison (section 2.6) and a radiative closure study, using observations from a site in The Netherlands during a period of clear-sky conditions (section 2.7).

## 2.2 Single scattering

First, we will define the quantities *radiance* and *irradiance*, which form the basis of the description of radiative transfer. Consider a radiant flux  $\Phi$  [W] through a surface  $A$  [m<sup>2</sup>] (see figure 2.1). *Irradiance* (also called flux density) is then defined as:

$$E = d\Phi/dA \quad (2.1)$$

in [W m<sup>-2</sup>]. Spectral irradiance is the irradiance between wavelength  $\lambda$  [nm] and  $\lambda + d\lambda$ :

$$E_\lambda = d^2\Phi/dAd\lambda \quad (2.2)$$

expressed in [W m<sup>-2</sup> nm<sup>-1</sup>]. Let a beam travel in the direction making an angle  $\theta$  with the unit normal of the surface  $A$  (figure 2.1). The radiant flux in a beam per unit projected area  $dA \cos \theta$  and solid angle  $d\omega$  of that beam is called *radiance*  $I$ :

$$I = \frac{d^2\Phi}{dA \cos \theta d\omega} \quad (2.3)$$

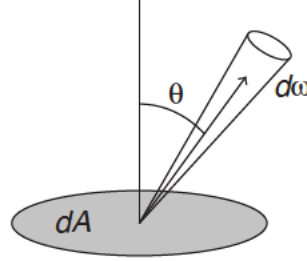


**Figure 2.1:** Radiance is the radiant flux in a beam per unit projected area  $dA \cos \theta$  and solid angle  $d\omega$ .

expressed in units  $[\text{W m}^{-2} \text{sr}^{-1}]$ . Finally, the *spectral radiance* (or spectral intensity)  $I_\lambda$  is the radiance between wavelength  $\lambda$  and  $\lambda + d\lambda$ :

$$I_\lambda = \frac{d^3\Phi}{dA \cos \theta d\omega d\lambda} \quad (2.4)$$

These quantities are interrelated as follows: radiance is the integral of spectral radiance over all wavelengths. Likewise, irradiance is the integral of spectral irradiance over all wavelengths. Furthermore, irradiance is the integral of radiance over all solid angles, and spectral irradiance is the integral of spectral radiance over all solid angles.

Consider a beam of light,  $I_\lambda$ , traversing a volume element (figure 2.2). As the beam travels through the volume element, it will be subject to extinction by the matter contained in the volume element. The rate of extinction,  $-dI_\lambda$ , is linearly dependent on  $I_\lambda$  and on the amount of matter along its path  $ds$ . This is commonly referred to as the law of Lambert-Beer-Bouguer:

$$dI_\lambda(\text{extinction}) = -k_{ext} I_\lambda ds \quad (2.5)$$

The quantity  $k_{ext}$  is called the extinction coefficient  $[\text{m}^{-1}]$ , which depends on the medium and on wavelength. We will not take into account thermal emission by the medium.

The extinction that is described by the Lambert-Beer-Bouguer law consists of both *scattering* and *absorption* of the beam:

$$k_{ext} = k_{abs} + k_{sca} \quad (2.6)$$

where  $k_{sca}$  is the scattering coefficient  $[\text{m}^{-1}]$  and  $k_{abs}$  the absorption coefficient  $[\text{m}^{-1}]$ . The extinction coefficient is related to the particle density  $\mathcal{N}$  [number of particles  $\text{m}^{-3}$ ] and the extinction cross-section  $\sigma_{ext}$  [ $\text{m}^2$  per particle]:

$$k_{ext} = \sigma_{ext} \mathcal{N} \quad (2.7)$$

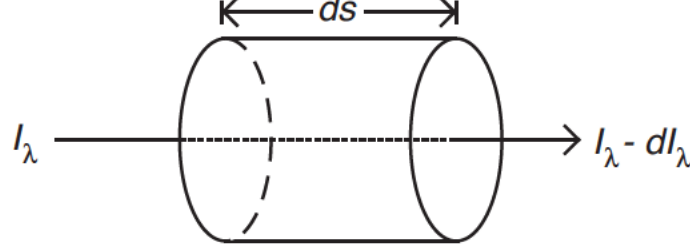


**Figure 2.2:** Extinction of a beam of light  $I_\lambda$  by a volume element, following the Lambert-Beer-Bouguer law for extinction. After having traversed the volume element, the extinction of the beam along its path  $ds$  is  $-dI_\lambda$ .

In literature,  $\mathcal{N}$  is usually expressed in number of particles per  $\text{cm}^3$ , and  $\sigma_{ext}$  in  $\text{cm}^2$  per particle.

The single scattering albedo  $\omega$  is defined as the fraction of the extinction that consists of scattering:

$$\omega = \frac{k_{sca}}{k_{abs} + k_{sca}} \quad (2.8)$$

The Lambert-Beer-Bouguer law from equation 2.5 can be integrated to yield the Lambert-Beer-Bouguer extinction law:

$$I_\lambda = I_{\lambda 0} e^{-\tau} \quad (2.9)$$

where  $I_{\lambda 0}$  is the intensity of the radiation beam before it encounters the volume element. The quantity  $\tau$  [unitless] is referred to as the optical distance, or optical depth, and it equals  $\int k_{ext} ds$ . In order to relate  $\tau$  to extinction processes in an atmosphere, we will have to define a suitable coordinate system.

A useful approximation for modelling atmospheric radiative transfer is to represent the atmosphere by a series of stacked, parallel layers. Such a configuration is referred to as a plane-parallel atmosphere. A coordinate system for a plane-parallel atmosphere is conveniently defined using  $z$  as a vertical coordinate, normal to the plane of the atmospheric layers (figure 2.3). The quantity  $z$  [m] then represents the altitude in the atmosphere. We can now define  $\tau$  in terms of altitude and vertical distribution of particle density  $\mathcal{N}(z)$ :

$$\tau = \int_z^\infty k_{ext} dz' = \int_z^\infty \sigma_{ext} \mathcal{N}(z') dz' \quad (2.10)$$

So far, we have ignored the angular dependence of scattering. A beam of radiation that traverses a volume element, as depicted in figure 2.2, will partly be scattered, but not necessarily equally in all directions. The angular distribution of scattered radiation is captured by the *scattering function* (also called phase scattering function). Before we can define the

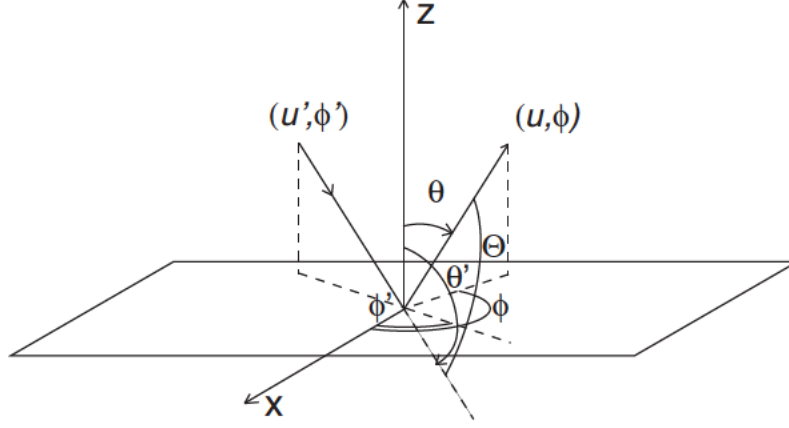


**Figure 2.3:** Coordinate system of the plane-parallel model atmosphere. The zenith angle  $\theta$  and azimuth angle  $\phi$  are defined with respect to an  $x, y, z$ -space with  $z$  extending in the vertical direction. Radiation arriving from direction  $(u', \phi')$  (where  $u' = \cos \theta'$ ) is scattered in the observation direction  $(u, \phi)$ . Since the plane-parallel atmosphere is homogeneous in the horizontal plane, only the relative azimuth angle  $\phi - \phi'$  is relevant.

scattering function, we will have to introduce a complete angular geometry of the medium.

The vertical coordinate  $z$  of a plane-parallel atmosphere was defined above, in the direction of the normal to the plane of the atmospheric layers. The zenith angle  $\theta$  is the angle with this normal, and  $\phi$  is the azimuth angle. It is convenient to define the zenith angle in terms of its cosine,  $u = \cos \theta$ . Furthermore, we define  $\mu = |u|$ . The direction of the incident radiation is defined as  $(u', \phi')$ , and the direction of observation is  $(u, \phi)$  (see figure 2.3). The *scattering angle*,  $\Theta$ , is then given as:

$$\cos \Theta = uu' + \sqrt{1-u^2}\sqrt{1-u'^2}\cos(\phi - \phi') \quad (2.11)$$

The scattering function,  $F(\cos \Theta)$ , defines the angular distribution of scattered radiation, and is normalized to unity, i.e.:

$$\frac{1}{2} \int F(\Theta) \sin \Theta d\Theta = 1 \quad (2.12)$$

An example of a scattering function is provided in chapter 3, where we will introduce the scattering of sunlight by cloud and snow particles. To conclude, we will introduce the asymmetry parameter,  $g$ , defined as:

$$g = \langle \cos \Theta \rangle \quad (2.13)$$

If  $g = 1$ , the scattering is completely forward. For  $g = -1$ , the scattering is completely backward. In the case that  $g = 0$ , the scattering is symmetric around  $\cos \Theta = 0$ , a special case

being isotropic scattering.

## 2.3 Multiple scattering

In the previous section, we have developed a set of quantities with which we are able to describe single-scattering processes from a volume element embedded in the atmosphere. The atmosphere consists of numerous of these volume elements, and radiation is also scattered *between* these volume elements. This process is called *multiple scattering*.

Equivalent to extinction, scattering and absorption coefficients for individual particles, we can define the *optical thickness* of an atmospheric layer,  $b$ , to characterize its optical properties. Separating extinction by aerosols or cloud particles (superscript  $a$ ) and molecules (superscript  $m$ ), we can write:

$$b = b_{sca}^m + b_{abs}^m + b_{sca}^a + b_{abs}^a \quad (2.14)$$

where  $b$  is the total or extinction optical thickness,  $b_{abs}^a$  and  $b_{abs}^m$  are the absorption optical thicknesses for aerosols and molecules, and  $b_{sca}^a$  and  $b_{sca}^m$  the scattering optical thicknesses for aerosols and molecules. In fact,  $b$  equals  $\tau$  (equation 2.10), but now for the entire layer or the entire atmosphere. The single-scattering albedo that holds for individual particles is also valid for these layer properties:

$$\omega = \frac{b_{sca}^a + b_{sca}^m}{b} \quad (2.15)$$

In an atmosphere, there is both loss of radiation due to scattering and absorption, and gain due to thermal emission and multiple scattering. Of these emission processes, we will neglect thermal emission, since we consider shortwave (solar) radiation only. The total change in radiation is:

$$dI_\lambda = dI_\lambda(\text{extinction}) + dI_\lambda(\text{emission}) = -k_{ext}ds(I_\lambda - J_\lambda) \quad (2.16)$$

where  $J_\lambda$  is a source function for emission. Since  $ds$  is in the traveling direction of radiation, thus making an angle  $\theta$  with the  $z$ -direction, we can use  $dz = -uds$  to get:

$$dI_\lambda = -k_{ext} \frac{dz}{-u} (I_\lambda - J_\lambda) \quad (2.17)$$

and, employing the relation  $d\tau = -k_{ext}dz$ :

$$u \frac{dI_\lambda}{d\tau} = -I_\lambda + J_\lambda \quad (2.18)$$

Both  $I_\lambda$  and  $J_\lambda$  depend on  $(\tau, u, \phi)$ . Equation 2.18 is the time-independent radiative transfer equation (RTE) for a plane-parallel atmosphere. This equation is valid if radiative fluxes are

stationary, and changes in the properties of the medium are sufficiently slow. In planetary radiative transfer problems, these conditions are easily met.

For the particular case of a plane-parallel atmosphere that is illuminated from above with incident sunlight having spectral irradiance  $E_{\lambda 0}$ , and without taking into account thermal emission of radiation, we can express the RTE as:

$$\begin{aligned} u \frac{dI_{\lambda}(\tau, u, \phi)}{d\tau} &= -I_{\lambda}(\tau, u, \phi) \\ &+ \frac{\omega}{4\pi} \int_0^{2\pi} \int_{-1}^1 F(\tau, u, u', \phi - \phi') I_{\lambda}(\tau, u', \phi') du' d\phi' \\ &+ \frac{\omega}{4\pi} F(\tau, u, u_0, \phi - \phi_0) e^{-\tau/\mu_0} E_{\lambda 0} \end{aligned} \quad (2.19)$$

where  $(u_0, \phi_0)$  is the direction of the incident sunlight. The source function  $J$  contributing to the direction  $(u, \phi)$  consists of (1) radiation that is scattered from all directions  $(u', \phi')$ , which is the second term on the right-hand side of equation 2.19, and (2) the scattering of the attenuated solar source  $e^{-\tau/\mu_0} E_{\lambda 0}$ , which is the third term on the right-hand side.

The RTE is presented here as a conservation law. Its derivation as sketched above is rather phenomenological, and it does not explain *why* or *how* particles are scattered. In other words, the physical basis of this derivation is uncertain. Only recently, the RTE has been derived from a unified microphysical approach, evolving directly from Maxwell's equations for macroscopic electromagnetic scattering [Mishchenko *et al.*, 2006; Mishchenko, 2008]. These papers discuss elastic scattering of electromagnetic waves by random many-particle groups, and show that the RTE is rooted in Maxwell's equations, thereby providing a solid physical understanding of radiative transfer in particulate media.

## 2.4 Doubling-adding method

Solving the RTE (equation 2.18) analytically is only possible under rather strict assumptions [see e.g. Thomas and Stamnes, 1999; Liou, 2002]. Under more complex conditions, and fully accounting for multiple scattering processes (as in equation 2.19), the RTE can only be solved using numerical methods. Various mathematical techniques have been developed to provide a formal solution of the RTE. One of these methods, which was first developed by Van de Hulst [1963], is the technique of doubling-adding. In fact, the doubling-adding method is not based directly on the RTE, but it is an intuitive, physical approach to calculate multiple scattering. The starting point for doubling-adding calculations of multiple scattering is a very thin layer, the reflection and transmission of which can be computed analytically from single and double scattering theory (requiring  $b$ ,  $\omega$  and  $F(\Theta)$ ). This thin layer is then doubled repeatedly until the desired optical thickness of the layer is reached. At each 'doubling' step, the internal radiation field is calculated at the layer boundaries, both in downward ( $D$ ) and upward

( $U$ ) directions, by computing the repeated reflections between the two layers. The doubling procedure is repeated for each of the  $N$  atmospheric layers. Finally, the ‘adding’ procedure, which is the same as the doubling procedure but for layers with different optical properties, is invoked to combine these layers to compute the radiation field of the entire atmosphere. The diffuse downward field at the lowermost boundary is the transmission function  $T$  and the diffuse upward field at the upper boundary is the reflection function  $R$ .

The model for the research in this thesis is based on the DAK model (Doubling Adding KNMI), version 2.5.1 (2005). Its mathematical foundations and numerical approach are described in *De Haan et al.* [1987]; *Stammes et al.* [1989]; *Hovenier et al.* [2004]. In DAK, a plane-parallel atmosphere consisting of molecules and particles (aerosols, cloud droplets or ice crystals) is considered. This atmosphere is illuminated from above by a parallel beam of monochromatic, unpolarized solar radiation  $E_{\lambda,0}$  traveling in direction  $(\mu_0, \phi_0)$ , where  $\mu_0 \neq 0$ . The atmosphere is bounded below by a reflecting surface with surface albedo  $\alpha(\lambda)$ . Inhomogeneity of the atmosphere is approximated by a stack of  $N$  homogeneous layers. DAK computes the polarized internal radiation field of the atmosphere. Emission of solar radiation by the atmosphere is not considered, i.e. it is assumed that there are no internal radiation sources in the shortwave spectrum [*Stammes et al.*, 1989].

The DAK model is capable of taking into account full polarization of radiation. We neglect polarization in this thesis, and we will therefore not use the matrix notation encountered in all literature on polarized doubling-adding [*De Haan et al.*, 1987; *Stammes et al.*, 1989; *Stammes*, 2001; *Hovenier et al.*, 2004] for which DAK is regularly used. For comparison however, we briefly show how the scalar quantities in this thesis are related to the matrix quantities in full polarized radiative transfer. In that case,  $I$  (omitting the subscript  $\lambda$ ) is the first element of the Stokes vector  $\mathbf{I} = [I, Q, \mathcal{U}, V]$ , where  $Q$  and  $\mathcal{U}$  describe linear polarization, and  $V$  represents circular polarization [*Chandrasekhar*, 1950]. The internal radiation field is then described by the  $4 \times 4$ -matrices  $\mathbf{R}$ ,  $\mathbf{T}$ ,  $\mathbf{U}$  and  $\mathbf{D}$ . These correspond to  $R$ ,  $T$ ,  $U$  and  $D$  in this thesis. The scattering function  $F(\Theta)$  mentioned above is equal to the  $F_{11}(\Theta)$ -element of the  $4 \times 4$  scattering matrix  $\mathbf{F}(\Theta)$ , and also to the element  $Z_{11}(\Theta)$  of the  $4 \times 4$  phase matrix  $\mathbf{Z}(\Theta)$  [*Hovenier et al.*, 2004].

DAK is a 1-D model in the sense that the spatial coordinate in the vertical direction is the only one considered: it describes a plane-parallel atmosphere, in which all properties of the layers are assumed to be homogeneous in the horizontal directions. At each model layer however, the radiation field is computed three-dimensionally — as a function of zenith and azimuth angles  $\theta$  and  $\phi$ .

In DAK, the scattering function  $F(\Theta)$  is specified for molecular ( $F^m(\Theta)$ ) and aerosol or cloud particles ( $F^a(\Theta)$ ) scattering. The computation of  $F^a(\Theta)$  for cloud particles (water droplets or ice crystals), is explained in section 3.2.

Molecular scattering ( $b_{sca}^m$ ) in DAK is confined to elastic Rayleigh scattering, which depends strongly on wavelength and air density [*Stam et al.*, 2000]. Aerosol scattering and absorption

$b_{sca}^m$  and  $b_{abs}^m$  are prescribed in DAK. Molecular absorption  $b_{abs}^m$  is a function of the absorption cross sections of the gases in the atmosphere, which are strongly dependent on wavelength, pressure, and temperature. The calculation of  $b_{abs}^m$  is central in the correlated- $k$  method for broadband calculations, which is treated in section 2.5.

## 2.5 Correlated $k$ -distribution method

DAK originally is a monochromatic radiative transfer model: it calculates the internal radiation field at a single wavelength only. All parameters determining the radiation field in the atmosphere can vary strongly with wavelength, e.g. the surface albedo  $\alpha(\lambda)$ , molecular scattering  $b_{sca}^m(\lambda)$ , and most importantly, absorption by gas molecules, represented by the molecular absorption optical thickness  $b_{abs}^m(\lambda)$ . The latter is also dependent on the temperature and pressure of the gases constituting the atmosphere. If the entire shortwave spectrum ( $250 < \lambda < 4000$  nm) is to be analyzed at a resolution sufficient to capture the irregular patterns of gas absorption bands, it would require several thousands of monochromatic line-by-line calculations. To avoid this computationally costly approach, we have implemented the correlated  $k$ -distribution method for gaseous absorption in DAK.

The correlated  $k$ -distribution allows for the computation of gas absorption of an entire wavelength interval using only a few radiative transfer calculations. The key aspect of the  $k$ -distribution method is to rearrange the absorption cross-sections in a wavelength interval in order of increasing magnitude, instead of by wavelength. In order to make this arrangement valid, the scattering properties of the atmosphere are assumed to be constant over the wavelength interval. Mathematically, this can be elucidated as follows:

Consider the direct transmission  $\mathcal{T}(v)$  in a wavelength interval  $\Delta\lambda$  (Lambert-Beer-Bouguer extinction law):

$$\mathcal{T}(v) = \frac{1}{\Delta\lambda} \int_{\Delta\lambda} e^{-k(\lambda)v} d\lambda, \quad (2.20)$$

where  $v$  is the column density [number of absorbing particles  $\text{m}^{-2}$ ] along the path of the light beam, and  $k(\lambda)$  the absorption cross-section [ $\text{m}^2$  per particle]. For a slant path,  $v$  is the slant column density; for a vertical path,  $v$  is the vertical column density. Note that  $k(\lambda)$  has the unit [ $\text{m}^2$ ] like  $\sigma_{ext}$  in equation 2.7, while the coefficients  $k_{ext}$ ,  $k_{sca}$  and  $k_{abs}$  used in section 2.2 have the unit [ $\text{m}^{-1}$ ]. Although we could have chosen a different symbol for  $k(\lambda)$  for clarity, we have decided to follow closely the notation in correlated- $k$  literature. With this notation, the absorption optical thickness  $b_{abs}^m(\lambda)$  is given by  $b_{abs}^m(\lambda) = k(\lambda)v$ , where  $v$  is the vertical column density.

As mentioned above, the integrand in equation (2.20) is highly irregular due to the complex pattern of absorption lines as a function of wavelength. It is now possible to rearrange the absorption cross sections without changing the integral in equation 2.20. If we define the

distribution function  $f(k)$ , being the probability of occurrence of a specific value of  $k$  in the wavelength interval  $\Delta\lambda$ , the transmission in that wavelength interval becomes:

$$\mathcal{T}(\nu) = \int_0^{\infty} f(k)e^{-k\nu} dk \quad (2.21)$$

The integrand is no longer dependent on wavelength  $\lambda$ . Mathematically, the quintessence of the  $k$ -distribution method is to turn this integrand into a smooth function by reordering the absorption cross-sections  $k$  in order of increasing magnitude, and defining the cumulative probability function  $g(k)$  [see *Lacis and Oinas*, 1991]:

$$g(k) = \int_0^k f(k') dk' \quad (2.22)$$

Upon inversion of  $g(k)$ , we get

$$\mathcal{T}(\nu) = \int_0^1 e^{-k(g)\nu} dg. \quad (2.23)$$

Since the integrand in equation (2.23) is now a smooth function in  $g$ -space by definition, the integral of equation (2.23) can be adequately approximated by a numerical Gaussian quadrature method involving only a few (typically 5-16) quadrature points, i.e. monochromatic radiative transfer calculations. In a formula, this Gaussian integral approximation becomes

$$\mathcal{T}(\nu) = \sum_{j=1}^n a_j e^{-k(g_j)\nu} \quad (2.24)$$

which is a summation over  $n$  Gaussian quadrature points, using absorption cross-sections  $k$  at coordinate  $g_j$ , and their corresponding weights  $a_j$ .

By using the same Gaussian quadrature for every atmospheric layer, the  $k$ -distribution method is said to be ‘correlated’. The interested reader is referred to the overview given by *Thomas and Stamnes* [1999, Ch. 10] for a thorough mathematical treatment.

The determination of all  $k(g_j)$  and  $a_j$  does initially require many line-by-line calculations for each wavelength interval. This has been done by *Kato et al.* [1999] using the HITRAN 1992 database. The correlated- $k$  absorption cross-sections are available through the libRadtran software package (<http://www.libradtran.org>). *Kato et al.* [1999] subdivided the shortwave spectrum into 32 wavelength intervals that closely follow absorption bands of the gases CO<sub>2</sub>, O<sub>2</sub>, O<sub>3</sub> and H<sub>2</sub>O. These wavelength intervals are shown in an example transmission spectrum in figure 2.4. For each gas in each wavelength interval, *Kato et al.* [1999] generated lookup tables of absorption cross-sections  $k$  as a function of temperature and pressure, for each Gaussian quadrature point. The absorption cross-sections of water vapour are also dependent on the water vapour concentration itself.

In table 2.1, we present the 32 wavelength intervals of the correlated- $k$  method. In the fourth

Band	Wavelength [nm]			$E_{\lambda 0}$ [W m <sup>-2</sup> ]	Absorbing gases			
	min	max	central		H <sub>2</sub> O	O <sub>3</sub>	O <sub>2</sub>	CO <sub>2</sub>
1	240	272	256	3.98		1		
2	272	283	278	2.28		1		
3	283	307	295	11.44		1		
4	307	328	317	15.53		1		
5	328	363	345	34.03		1		
6	363	408	385	55.51		1		
7	408	452	430	80.40		1		
8	452	518	485	132.80		1		
9	518	540	529	41.42		1		
10	540	550	545	18.78	5	1		
11	550	567	558	31.49		1		
12	567	605	586	67.96	6	1		
13	605	625	615	33.74		1		
14	625	667	646	65.89	6	1		
15	667	684	675	25.33		1		
16	684	704	694	28.67	6	1	6	
17	704	743	724	52.56	6			
18	743	791	767	58.70			6	
19	791	844	818	57.65	6			
20	844	889	867	43.25	5			
21	889	975	932	72.39	8			
22	975	1046	1010	50.70	6			
23	1046	1194	1120	84.23	7			
24	1194	1516	1355	121.98	8			
25	1516	1613	1565	25.46	6			7
26	1613	1965	1789	61.56	11			
27	1965	2153	2059	19.99	6			6
28	2153	2275	2214	9.64	5			
29	2275	3001	2639	31.74	8			16
30	3001	3635	3319	11.46	7	14		
31	3635	3991	3813	3.68	5			6
32	3991	4606	4298	3.82	6			18

**Table 2.1:** Properties of each of the 32 wavelength intervals for the correlated-k method. The rightmost four columns indicate the number of Gaussian quadrature points used for the calculation of absorption by H<sub>2</sub>O, O<sub>3</sub>, O<sub>2</sub> and CO<sub>2</sub>, respectively. If there is no number, absorption of that gas is not calculated in that interval.

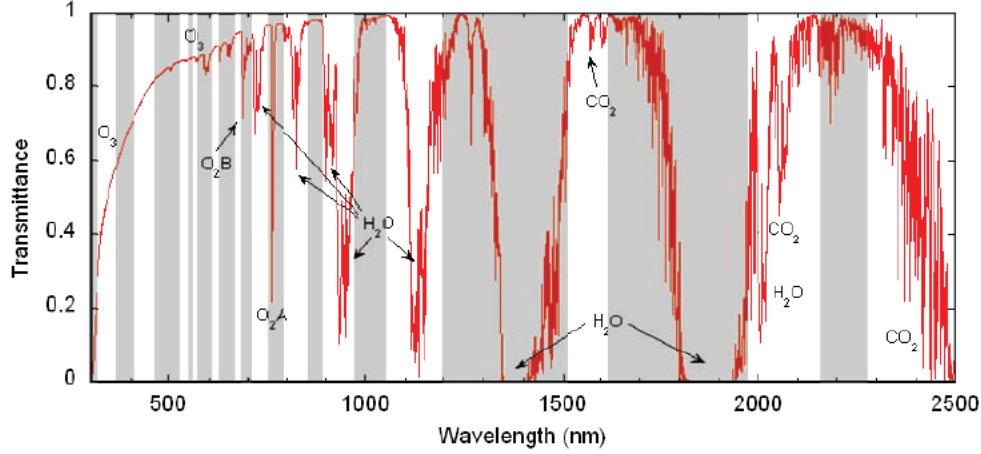


**Figure 2.4:** Example of a typical transmission spectrum for shortwave radiation measured at the Earth's surface, calculated by the Moderate resolution radiative Transfer model MODTRAN, for a standard atmosphere at sea level. The major absorption bands have been labeled with the corresponding gases. The wavelength intervals defined by Kato *et al.* [1999], ranging from 250 to 4,000 nm, are shown as alternating grey and white backgrounds. These bands are also used in DAK.

column, the top-of-atmosphere irradiance  $E_0$  [ $\text{W m}^{-2}$ ] per wavelength interval is given, based on the solar irradiance spectrum by Gueymard [2004]. In the rightmost four columns, the number of Gaussian quadrature points  $n$  are given for each gas. For bands 1–16, absorption by ozone is calculated with only one Gaussian quadrature point, so that the vertical transmission due to ozone in each band is simply  $\mathcal{T} = e^{-k\nu} = e^{-b_{abs}^m}$ .

If we consider a wavelength interval with only one absorbing gas (e.g. band 17 with only  $\text{H}_2\text{O}$  absorption), then the internal radiation field is calculated as follows:

For each layer  $l$ , the absorption cross-section  $k(g_j)$  is retrieved from the lookup tables by Kato *et al.* [1999], using the temperature, pressure and water vapour concentration of each layer. Together with the vertical column density  $\nu(l)$  (of  $\text{H}_2\text{O}$  in this case), the molecular absorption optical thickness is calculated for each layer:

$$b_{abs}^m(j, l) = k(g_j) \cdot \nu(l) \quad (2.25)$$

Using these values for  $b_{abs}^m$ , the entire internal radiation field is calculated as if it were a monochromatic calculation for the entire atmosphere. For every Gaussian quadrature point  $g_j$ , this yields a reflection and transmission function  $R_j$  and  $T_j$  for the atmosphere, and the internal radiation field functions at the layer boundaries  $U_j$  and  $D_j$ . At the end of the calculations for the  $n$  Gaussian quadrature points, the total  $R$ ,  $T$ ,  $U$  and  $D$  are calculated using the

weights  $a_j$ :

$$R = \sum_{j=1}^n a_j R_j \quad (2.26)$$

$$T = \sum_{j=1}^n a_j T_j \quad (2.27)$$

$$U = \sum_{j=1}^n a_j U_j \quad (2.28)$$

$$D = \sum_{j=1}^n a_j D_j \quad (2.29)$$

In some bands, radiation is absorbed by more than one gas species (e.g. band 25 with both H<sub>2</sub>O and CO<sub>2</sub> absorption). Assuming that absorption by two different species is uncorrelated [Kato *et al.*, 1999], the molecular absorption optical thickness is calculated for each layer as:

$$b_{abs}^m(j_1, j_2, l) = k(g_{1,j_1})v_1(l) + k(g_{2,j_2})v_2(l) \quad (2.30)$$

where subscripts 1 and 2 denote the two gas species. If there are  $n_1$  and  $n_2$  Gaussian quadrature points for species 1 and 2, there will be  $n_1 \cdot n_2$  calculations of the internal radiation field for that wavelength interval. The resulting reflection  $R$  for the wavelength interval is calculated as:

$$R = \sum_{j_1}^{n_1} \sum_{j_2}^{n_2} a_{1,j_1} a_{2,j_2} R_{j_1 j_2} \quad (2.31)$$

and similarly,  $T$ ,  $U$  and  $D$  are computed. In general, for  $p$  overlapping gases,

$$R = \sum_{j_1}^{n_1} \sum_{j_2}^{n_2} \dots \sum_{j_p}^{n_p} \left[ R_{j_1 j_2 \dots j_p} \left[ \prod_{q=1}^p a_{q,j_q} \right] \right] \quad (2.32)$$

and again, similar relations hold for  $T$ ,  $U$  and  $D$ . In equations 2.31 and 2.32,  $R_{j_1 j_2}$  and  $R_{j_1 j_2 \dots j_p}$  are in fact similar to  $R_j$  in equation 2.27, but with multiple subscripts for the different gases.

In the correlated- $k$  distribution method implemented in DAK, all other properties of the atmosphere and surface, e.g. molecular (Rayleigh) scattering, are taken at the central wavelength of each wavelength interval (see table 2.1).

## 2.6 Validation I: Model intercomparison

The radiative transfer model outlined in sections 2.4 and 2.5 needs a proper validation before it is applied to radiative transfer studies in the snow-atmosphere system. Although an obvious validation setup would be to compare model output to a ‘laboratory’ setting in which all relevant parameters are accurately known, radiative transfer in the atmosphere is not easily captured in such a laboratory environment. As a surrogate, we will present a comparison of DAK with another radiative transfer model in this section, and a radiative closure study in section 2.7. The aim of the model intercomparison is to put certain confidence in the output of DAK, although an intercomparison study can never *prove* model correctness — after all, both models could be equally wrong yet show excellent agreement. The radiative closure study in section 2.7 however, serves two important purposes. First of all, it is meant to demonstrate the ability of the model to simulate atmospheric radiative transfer (but again, not *prove* model correctness). Secondly, a very important implication of good closure results is that we can describe radiative transfer in a real atmosphere with the processes that are included in the model, and therefore *understand* all processes in atmospheric radiative transfer.

In this section, we subject the broadband version of DAK to a comparison with the parameterized radiative transfer model SMARTS (Simple Model for Atmospheric Radiative Transfer of Sunshine, [Gueymard, 2001]), also documented in Wang *et al.* [2008]. SMARTS deploys parameterizations that are based on calculations with the Moderate resolution radiative Transfer model MODTRAN [Berk *et al.*, 1998]. In a publication by Michalsky *et al.* [2006], SMARTS is one of the models that was used in an attempt to attain radiative closure for direct and diffuse shortwave radiation under clear-sky conditions during a large aerosol intensive observation period at the Southern Great Plains site (near Billings, Oklahoma, United States) in May 2003. It was found that direct-beam calculations by SMARTS were accurate to within 0.1%, whereas diffuse radiation calculations differed by 1.9% on average. This result is within the estimated uncertainty of the direct (8–12%) and diffuse (4%) irradiance measurements and much better than previous clear-sky closure studies.

For the clear-sky irradiance model intercomparison between DAK and SMARTS, the input was prepared identically for both models. The atmospheric profile is a standard mid-latitude summer atmosphere, describing vertical profiles of temperature, pressure, H<sub>2</sub>O, O<sub>3</sub>, and O<sub>2</sub>. The CO<sub>2</sub> mixing ratio was set at 370 ppmV, well-mixed throughout the atmosphere. The solar spectrum was adopted from the SMARTS model [Gueymard, 2004], adding up to a total solar irradiance at the top-of-atmosphere of 1366 W m<sup>-2</sup>, perpendicular to the beam. The SMARTS model computed irradiances for solar zenith angles between 0° and 90° with intervals of 1°, while DAK calculations were done at 0, 30, 45, 60, 70 and 80° for computational reasons. The results of this comparison are shown in figure 2.5, showing DAK and SMARTS direct, diffuse and global irradiances in panel (a) and their differences in panel (b). Global irradiance — also called total irradiance — is here defined as the sum of direct and diffuse irradiances. The absolute differences in both direct and diffuse irradiance are small

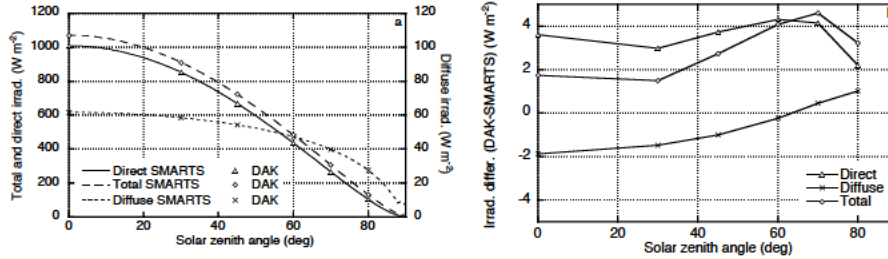


**Figure 2.5:** (a) DAK and SMARTS simulated direct, diffuse and total irradiances for an atmosphere without aerosols, as a function of solar zenith angle SZA; (b) differences DAK – SMARTS as a function of SZA.

(<  $5 \text{ W m}^{-2}$ ), and in a relative sense, differences are up to 3.5% for diffuse irradiance and 1% for direct and global irradiance.

At closer inspection of the spectral irradiances at  $\theta_0 = 30^\circ$  (figure 2.6), the agreement between DAK and SMARTS for spectral diffuse irradiance is excellent (<  $0.5 \text{ W m}^{-2}$  difference in each wavelength interval), and the agreement between DAK and SMARTS global irradiances is very good, with maximum absolute differences of  $2 \text{ W m}^{-2}$  in the 1613–1965 and 2275–3001 nm wavelength bands.

Additionally, three cases with the inclusion of LOWTRAN (Low resolution radiative Transfer model [Kneizys *et al.*, 1988]) aerosols (urban, rural and maritime) are considered in the model intercomparison. For all cases, the aerosol optical thickness  $b^a$  is taken 0.2 at  $\lambda = 500 \text{ nm}$ . Intercomparison results (not shown here, see Wang *et al.* [2008]) show that DAK and SMARTS agree very well on direct irradiances (maximum difference  $2 \text{ W m}^{-2}$ , < 1%), but less so on diffuse irradiances (maximum difference  $10 \text{ W m}^{-2}$ ). The models agree well on direct irradiance as it depends largely on  $b^a$ , which is prescribed equally in both models. The small discrepancy for diffuse irradiance is difficult to trace, since SMARTS uses parameterizations for aerosol optical properties that are based on tabulated LOWTRAN data, whereas in DAK, the LOWTRAN tables were used directly. Furthermore, the difference in diffuse irradiance could partly be explained by the fact that DAK performs full multiple-scattering calculations, while SMARTS only approximates the effect of multiple scattering using a parameterization.

Concluding, the agreement between both models is excellent for an aerosol-free atmosphere, both for direct and diffuse, broadband and spectral irradiances. In case aerosols are included, a proper wavelength-dependent treatment of  $b^a$ ,  $\omega$  and  $g$  is required.

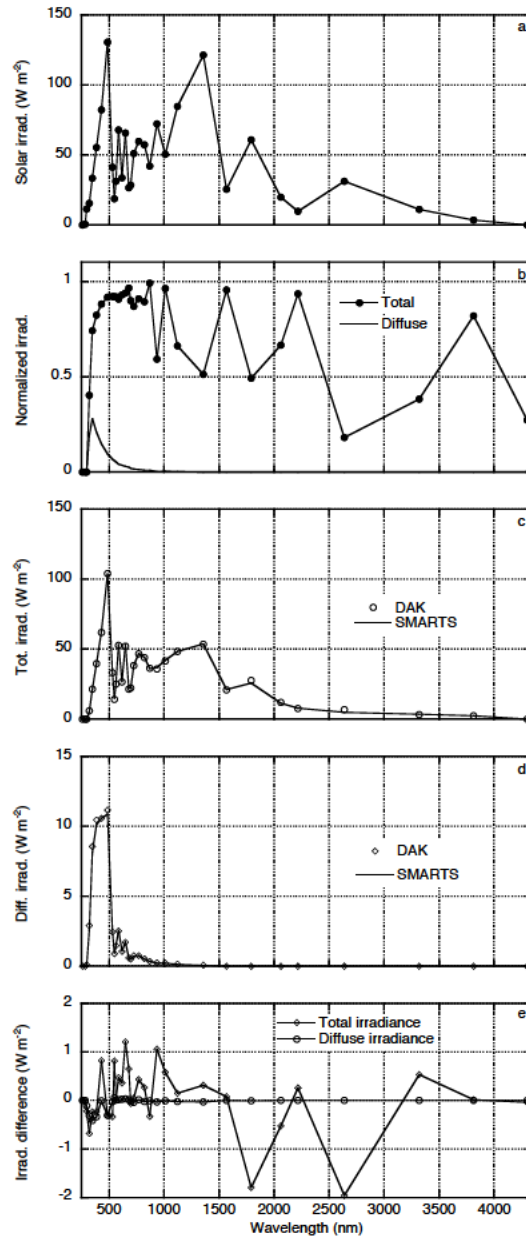


**Figure 2.6:** (a) Solar irradiance spectrum at top of atmosphere (TOA) in the 32 DAK wavelength bands; (b) DAK simulated total (= global) and diffuse irradiance spectra, normalized to incident TOA radiation; (c) DAK and SMARTS simulated irradiance spectra at the surface for total irradiance at the surface; (d) idem for diffuse irradiance spectra; (e) differences between DAK and SMARTS. All the simulated spectra are at  $\theta_0 = 30^\circ$ .

## 2.7 Validation II: Clear-sky radiative closure study

Although the model intercomparison in section 2.6 gives confidence in the performance of DAK, the model is put to the test by comparing model output to clear-sky measurements of direct, diffuse and global irradiances at the surface. During the last two decades, several attempts have been made to achieve agreement between clear-sky broadband irradiance models and surface measurements of direct and diffuse irradiance [Henzing *et al.*, 2004]. Such an agreement is called closure. In general, models and measurements agreed well for the direct component, but agreement for diffuse irradiances remained problematic. Due to improved instrumentation and model input specification, Michalsky *et al.* [2006] were able to present better results than previously achieved. The authors report biases between models and measurements of generally less than 1% for direct irradiance and less than 1.9% for diffuse irradiance. In general, the number of studies reporting a satisfactory degree of closure for both direct and diffuse irradiance is still limited.

For the comparison under consideration here, we deployed the measurements made at Cabauw, The Netherlands (51.97 °N, 4.93 °E), during the May 2008 IMPACT (Intensive Measurement Period At the Cabauw Tower) measurement campaign, performed in the framework of EU-CAARI (European Integrated project on Aerosol Cloud Climate and Air Quality Interactions) [Wang *et al.*, 2009]. Although IMPACT produced a wealth of data, it was decided to use only routine measurements from the Baseline Surface Radiation Network (BSRN) and the Aerosol Robotic Network (AERONET, [Dubovik *et al.*, 2000]), supplemented with radiosonde observations. The rationale for this approach is the possibility of performing similar closure studies at other locations or for other periods.

In section 2.6, it was already shown that a closure study of measured and modelled shortwave radiation would benefit from taking into account the wavelength dependence of aerosol optical properties. In order to prescribe appropriate aerosol optical thickness  $b_{tot}^a \equiv b_{abs}^a + b_{sca}^a$ , data was extracted from AERONET Level 1.5 data for Cabauw. These data are available at wavelengths of 440, 675, 870 and 1020 nm. Between 440 and 1020 nm, values for single scattering albedo  $\omega$ , asymmetry parameter  $g$  and  $b_{tot}^a$  are interpolated to the DAK wavelength grid. Outside this part of the spectrum,  $\omega$  and  $g$  were taken from the continental aerosol model of WCP-55 [Deepak and Gerber, 1983]. Outside the 440–1020 nm range,  $b_{tot}^a$  was extrapolated using the four AERONET values.

Temperature, pressure and humidity were taken from radiosonde launches and regridded to the DAK vertical layer profile of 32 layers, each being 1 km thick up to a height of 25 km. All vertical profiles of water vapour were scaled to the AERONET water vapour column. The total ozone column was taken from Ozone Monitoring Instrument (OMI) retrievals. A typical spectral albedo curve for grassland was used as a lower boundary condition.

Cabauw is a location that participates in the worldwide Baseline Surface Radiation Network (BSRN) [Ohmura *et al.*, 1998] and measures direct, diffuse and global irradiance according

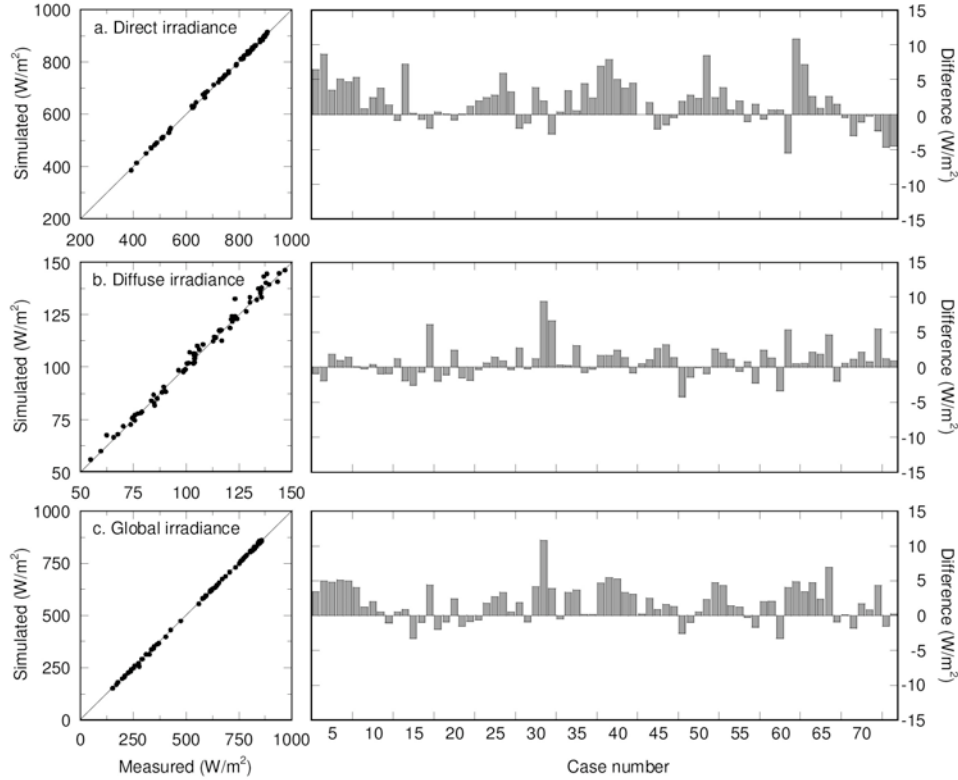


**Figure 2.7:** (a) Left panel: scatterplot of DAK simulations versus BSRN measurements of direct irradiance, right panel: differences between DAK simulations and BSRN measurements for each of the 72 cases; (b) *idem* for diffuse irradiance; (c) *idem* for global irradiance. Measurements were performed in Cabauw, The Netherlands, between 5 and 11 May, 2008.

to the highest standards. Direct irradiance was obtained from a Kipp & Zonen CH1 pyrhe-liometer; diffuse and global irradiances were measured using Kipp & Zonen CM22 pyra-nometers. Operational uncertainties for the Southern Great Plains, a site similar to Cabauw, are  $14 \pm 6 \text{ W m}^{-2}$  for direct irradiance and  $9 \pm 3 \text{ W m}^{-2}$  for diffuse irradiance [Shi and Long, 2002]. During a period of exceptionally fine, cloudless weather between 5 and 11 May 2008, 72 cases were selected for the comparison. During these cases,  $b_{tot}^a$  at 555 nm ranges from 0.08 to 0.27, the water vapour column varies between 0.65 and 1.72 cm. Furthermore,  $\omega$  is between 0.85 and 0.99, and  $g$  ranges from 0.61 to 0.71.

The left panels in figure 2.7(a)–(c) show scatterplots of all DAK simulations versus BSRN measurements of direct, diffuse and global irradiance. These plots, with the one-to-one lines indicated, show that there are excellent correlations for the three components. The sample

standard deviations are small:  $3 \text{ W m}^{-2}$  for direct irradiance,  $2 \text{ W m}^{-2}$  for diffuse irradiance, and  $3 \text{ W m}^{-2}$  for global irradiance. The differences between DAK simulations and BSRN measurements are also shown in the right panels of Figure 2.7(a)–(c). The absolute range in model-measurement difference is between  $-5$  and  $+11 \text{ W m}^{-2}$  for direct irradiance, between  $-4$  and  $+9 \text{ W m}^{-2}$  for diffuse irradiance, and between  $-3$  and  $+11 \text{ W m}^{-2}$  for global irradiance. The ranges of relative differences are  $-1.4$  to  $+1.6\%$ ,  $-3.9$  to  $+8.5\%$ , and  $-1.4$  to  $+2.7\%$ , respectively. The mean differences are  $2 \text{ W m}^{-2}$  ( $+0.2\%$ ) for direct irradiance,  $1 \text{ W m}^{-2}$  ( $+0.8\%$ ) for diffuse irradiance, and  $2 \text{ W m}^{-2}$  ( $+0.3\%$ ) for global irradiance.

The good results can partly be explained by the proper specification of the DAK model input and the high quality of the BSRN measurements. The simulation of direct irradiance is sensitive to values for aerosol optical properties. Since these parameters are wavelength dependent, a correct description of their spectral behaviour is crucial for good closure results.

Considering the operational measurement uncertainties, the DAK simulations are well within the uncertainty range of the BSRN measurements. Even if only calibration uncertainties are considered, there is, on average, near-perfect agreement between the DAK simulations and BSRN measurements. Moreover, if one takes into account that the DAK simulations also carry a certain degree of uncertainty, the general conclusion is that excellent closure was obtained between model and measurements of shortwave irradiances.

The strength of this closure study lies in the use of operational measurements (BSRN and AERONET), and in its relative simplicity. Around the world, 15 more BSRN stations also perform AERONET measurements, so the method presented here opens up possibilities for many more closure studies for different radiative and aerosol climates.

## 2.8 Conclusions

In this chapter, we have presented a radiative transfer model that can be used to study solar radiation in an atmosphere containing water vapour, other gases, and aerosols. Using the correlated- $k$  method, we expanded the originally monochromatic DAK model into a model for the entire solar spectrum. The model has been compared to another radiative transfer model (SMARTS), and to field measurements of direct, diffuse and global irradiance during a period of clear-sky occurrence at Cabauw. Given the fact that these comparisons yielded close agreement of DAK with both SMARTS and the field measurements, we can be fairly certain that the model is capable of accurately simulating radiative transfer in a clear-sky atmosphere. This is an important step towards studying the problem of radiative transfer in the snow-atmosphere system. We will now need to incorporate, in some way, the effects of clouds and snow on the radiation field. In the mathematical framework of the model, it means that we have to find a way to calculate scattering functions  $F^a$  for snow and cloud layers. This will be the subject of chapter 3.



## Modelling radiative transfer in the snow-atmosphere system

### Summary

In this chapter, we demonstrate the ability of the DAK model, which was introduced in the previous chapter, to calculate radiative transfer through clouds and within a snowpack. In DAK, clouds and snow are represented as layers with a scattering function. These scattering functions are calculated using a ray tracing program that requires shape and dimensions of an ice crystal, and a volume absorption coefficient as input. Soot in the snowpack can be included using scattering and absorption coefficients that are taken from the OPAC data set (Optical Properties of Aerosols and Clouds). For a clear sky over a snowpack, the effects of solar zenith angle, atmospheric optical thickness, and snow grain size on both spectral and broadband snow surface albedo can be simulated adequately. Clouds increase the broadband clear-sky albedo of snow, and annihilate the effect of solar zenith angle on broadband albedo. In the presence of clouds, the spectral albedo of snow equals that under a clear sky with a solar zenith angle of about  $50^\circ$ . Model results presented in this chapter agree well with results published elsewhere.

---

The snow model has been published in Kuipers Munneke, P., C. H. Reijmer, M. R. van den Broeke, P. Stammes, G. König-Langlo and W. H. Knap (2008), Analysis of clear-sky Antarctic snow albedo using observations and radiative transfer modeling, *J. Geophys. Res. (D)*, **113**, D17,118, doi:10.1029/2007JD009653.

### 3.1 Introduction

The clear-sky atmospheric part of the radiative transfer model DAK has been described and tested in the previous chapter. In order to perform radiative transfer calculations in and above a snowpack, snow layers have to be included in the model. In section 3.2, we will demonstrate how optical properties of snow are defined in the model. In section 3.3, we show that the model is able to calculate radiative transfer in the presence of a snow layer but no clouds, to which we will refer as clear-sky conditions. Several snow properties are varied and the resulting spectral and broadband surface albedos are examined.

Clouds that overlay the snowpack can also be accounted for. The optical properties of clouds are computed in exactly the same way as those of a snowpack (section 3.2). In section 3.4, we present results of radiative transfer calculations in situations in which a cloud overlays the snowpack.

### 3.2 Optical properties of snow and clouds

In DAK, both snow and clouds are treated as particulate media consisting of mutually independent ice crystals, or water droplet in the case of water clouds. The ice crystals can be either of spherical or (imperfect) hexagonal shape. Water droplets attain a spherical shape. The optical properties of a snow or cloud layer are captured with a volume absorption coefficient  $b_{abs}^a$  and a scattering function,  $F^a(\Theta)$ . A value for  $b_{abs}^a$  is derived using the imaginary part  $\Im$  of the refractive index of ice  $m_i$  [Wiscombe and Warren, 1980], updated with data from Warren *et al.* [2006] for the UV/visible range:

$$b_{abs}^a = 4\pi\lambda^{-1}\Im(m_i(\lambda)) \quad (3.1)$$

The single scattering albedo  $\omega$  for a snow or cloud layer is calculated using equation 2.15, now including scattering by snow or cloud particles.

$F^a(\Theta)$  of the ice crystals is calculated using SPEX [Hess *et al.*, 1998a]. SPEX is a Monte Carlo-type raytracing computer program — a large number ( $\sim 10^7$ ) of photons are released in a parallel beam from a randomly chosen initial position, and the reflections, refractions and absorption of each photon is then computed using geometric methods. The result is the scattering function  $F^a(\Theta)$ , a function that describes the distribution of the scattered photons over all angles. An example scattering function is shown in figure 3.1.  $F^a(\Theta)$  is consequently expanded in generalized spherical harmonics following the method by De Rooij and van der Stap [1984], since these are, in a mathematical sense, easily integrated in the reflection and transmission functions in DAK.

The scattering of solar radiation by ice crystals and water droplets typically found in clouds and snow, is dominantly in the forward direction. Since it is numerically daunting to deal with

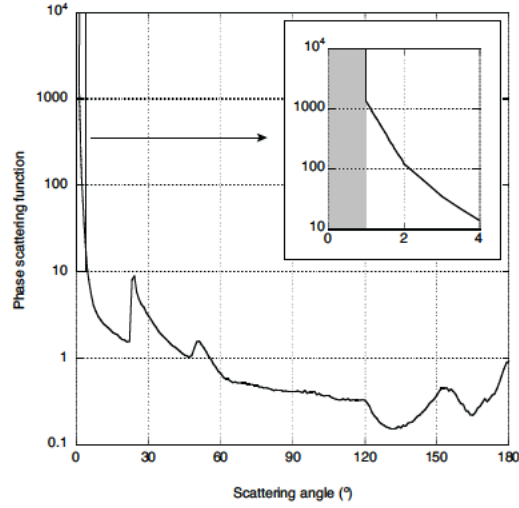


**Figure 3.1:** Example scattering function as a function of scattering angle, for a beam of wavelength  $\lambda = 345$  nm impinging on a hexagonal-plate shaped crystal with thickness  $c = 0.2436$  mm and side length  $a = 0.0974$  mm (giving  $r_e = 0.10$  mm). The inset shows a magnification of the scattering function between  $0-4^\circ$ . The gray area shows the  $1^\circ$ -cutoff for the delta approximation, and represents a Dirac- $\delta$  function for the interval  $0-1^\circ$ .

such strongly forward-peaked functions,  $F^a(\Theta)$  is converted using the delta approximation [Potter, 1970] with a cutoff angle of  $1^\circ$ . It means that photons that deviate less than  $1^\circ$  from their original direction of propagation after scattering, are treated as if no scattering had taken place at all. In a mathematical sense, the scattering function between  $0-1^\circ$  is replaced by a Dirac- $\delta$  function (illustrated in figure 3.1). This leads to a decrease in both absorption and optical thickness. To compensate for this decrease,  $F^a(\Theta)$  is scaled outside this  $1^\circ$ -peak. It was found that results of radiative transfer calculations through a snowpack do not change significantly when the cutoff angle is decreased to less than  $1^\circ$ .

For the calculation of the albedo of a snowpack, the lowermost  $n_l$  layers of DAK are given optical properties of a snow layer by assigning the snow optical properties  $F^a(\Theta)$ ,  $b^a$ , and  $\omega_a$  (figure 3.2). The  $n_l$  snow layers together are chosen to be so opaque that virtually no radiation arrives at the lower model boundary (for a 10 m snow layer,  $b^a > 2 \times 10^6$ , depending on wavelength). The requirement to prescribe a surface albedo to the lower model boundary has become irrelevant in this way: the surface albedo of the snowpack can now be studied independently by looking at the up- and downward radiation fluxes at the uppermost boundary of the  $n_l^{\text{th}}$  layer [see also Aoki *et al.*, 1999]. In the remainder of this section, the calculation of snow surface albedo at this boundary is formalized.

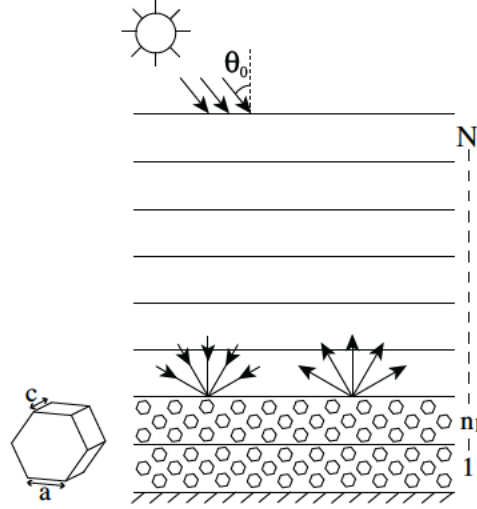


**Figure 3.2:** Schematic setup of the DAK model for studying spectral and broadband snow surface albedo. Solar radiation incident at the top of atmosphere has a solar zenith angle  $\theta_0$ . The lowermost  $n_s$  layers are filled with snow, consisting of hexagonal ice crystals with dimensions  $c$  and  $a$ . The snow surface albedo is calculated from the radiation field at the upper boundary of the  $n_s^{\text{th}}$  layer. The total number of layers for the atmosphere including snow layers is  $N$ .

The radiation field (described by the spectral intensity  $I_\lambda$  as in equation 2.4) in a medium is a function of zenith angle  $\theta$ , azimuth angle  $\phi$ , and wavelength  $\lambda$ . The amount of radiation of wavelength  $\lambda$  arriving at the snow surface  $E_{\lambda\downarrow}$  (monochromatic irradiance) can be expressed in terms of the radiation field at the surface:

$$E_{\lambda\downarrow} = \int_0^{\frac{\pi}{2}} \int_0^{2\pi} I_\lambda(\theta, \phi) \sin\theta \cos\theta d\phi d\theta \quad (3.2)$$

Similarly, the reflected radiation  $E_{\lambda\uparrow}$  can be defined. The spectral surface albedo  $\alpha_\lambda$  is then defined as the ratio of reflected and incoming spectral irradiance:

$$\alpha_\lambda = \frac{E_{\lambda\uparrow}}{E_{\lambda\downarrow}} \quad (3.3)$$

Broadband shortwave radiation is denoted in this thesis as  $SW$ . It is defined here as the spectral irradiance  $E_\lambda$  between  $\lambda_1$  and  $\lambda_2$ . Incoming broadband shortwave radiation is defined as:

$$SW_{\downarrow} = \int_{\lambda_1}^{\lambda_2} E_{\lambda_{\downarrow}} d\lambda \quad (3.4)$$

Analogously, the reflected broadband shortwave radiation  $SW_{\uparrow}$  is defined using  $E_{\lambda_{\uparrow}}$ . Depending on the application, the values of  $\lambda_1$  and  $\lambda_2$  will vary a bit, but generally, they are in the range of 250 and 4000 nm. The albedo for broadband shortwave radiation  $\alpha$  (hereafter referred to as broadband albedo) is given by:

$$\alpha = \frac{SW_{\uparrow}}{SW_{\downarrow}} = \frac{\int_{\lambda_1}^{\lambda_2} E_{\lambda_{\downarrow}} \alpha_{\lambda} d\lambda}{\int_{\lambda_1}^{\lambda_2} E_{\lambda_{\downarrow}} d\lambda} \quad (3.5)$$

From the above, it is clear that the broadband albedo of the snow surface is *not* an inherent property of the snow. It depends on the radiation field arriving at the surface, which may in turn depend on the zenith angle of the sun, the absorption and scattering by atmospheric gases, aerosols and clouds. This is exactly the reason why the atmospheric part of DAK, as presented in chapter 2, is crucial in modelling snow surface albedo.

### 3.3 Clear-sky snow albedo

The first comprehensive and physically consistent model for the albedo of snow was put forward by *Wiscombe and Warren* [1980]. Using Mie theory for single scattering properties of ice crystals, and the delta-Eddington approximation for the description of multiple scattering, the authors demonstrated the effect of solar zenith angle ( $\theta_0$ ), snow grain size (radius  $r_e$ ), and cloud cover on the albedo of a snow surface. Moreover, they discussed the effects of close packing of snow grains, and nonsphericity of snow grains. The same authors also explored the effects of impurities contained in the snow on the surface albedo [*Warren and Wiscombe*, 1980]. In the following sections (3.3.1–3.3.2, and 3.4), we will briefly present the well-accepted theory of *Wiscombe and Warren* [1980] and *Warren and Wiscombe* [1980] and show that DAK, with the inclusion of the snow model as illustrated in figure 3.2, mimics all of its aspects.

Throughout this chapter, the snowpack is assumed to consist of ice crystals shaped like irregular hexagonal plates. The aspect ratio  $\Gamma$  ( $= c/2a$ ) is fixed at 0.2, where  $c$  is the central axis of the plate (its ‘thickness’), and  $a$  the length of each of the sides of the hexagon (figure 3.2). Irregularity refers to some distortion of the crystal faces. It is obtained by, within limits, changing the surface normal randomly while performing the ray-tracing calculations [see *Macke et al.*, 1996; *Hess et al.*, 1998a; *Knap et al.*, 2005]. Its effect is to smoothen the scattering function  $F^a(\Theta)$  somewhat.

To facilitate comparison with other literature, snow grain size will be expressed by the quantity  $r_e$ , best described as the optically equivalent snow grain size [e.g. *Nolin and Dozier, 2000; Legagneux et al., 2006; Matzl and Schneebeli, 2006*]. It refers to the radius of a spherical particle that has the same volume-to-surface ratio as the hexagonal ice plate. It has been hypothesized [*Wiscombe and Warren, 1980*] and demonstrated [*Grenfell and Warren, 1999; Neshyba et al., 2003*] that the scattering and absorptive properties of any type of crystal can be approximated by those of a spherical particle, as long as the volume-to-surface ratio is conserved. In order to achieve this, the number of particles must be scaled.

Since the volume-to-surface ( $V/A$ ) ratio of a sphere of radius  $r$  is  $r/3$ , the optically equivalent snow grain radius is

$$r_e = 3 \frac{V}{A} \quad (3.6)$$

The number of spheres  $n_s$ , relative to the number of nonspherical particles  $n$  is

$$\frac{n_s}{n} = \frac{3V}{4\pi r_e^3} \quad (3.7)$$

In the case of hexagonal plates [*Neshyba et al., 2003*], equation 3.6 becomes

$$r_e = \frac{3\sqrt{3}ac}{4c + 2\sqrt{3}a} \quad (3.8)$$

or, using  $\Gamma (= c/2a)$ :

$$r_e = \frac{3\sqrt{3}a\Gamma}{4\Gamma + \sqrt{3}} \quad (3.9)$$

and

$$\frac{n_s}{n} = \frac{(4\Gamma + \sqrt{3})^3}{36\pi\Gamma^2} \quad (3.10)$$

### 3.3.1 Pure snow

In this section, we present results of various numerical experiments simulating clear-sky conditions, in which the snow grain size  $r_e$ , and the solar zenith angle  $\theta_0$  are varied. All experiments in this section were carried out using a standard subarctic summer atmosphere [*Anderson et al., 1986*]. Similar results, using spherical ice particles only, have been presented by *Aoki et al. [1999]* and *Wiscombe and Warren [1980]*. The difference between the

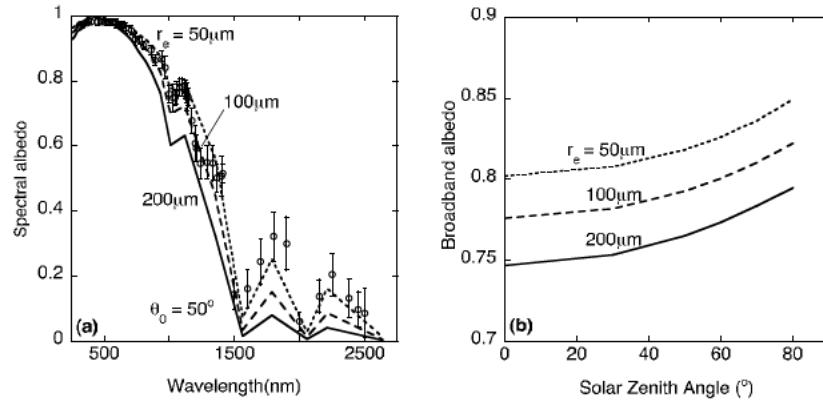


**Figure 3.3:** (a) Spectral albedo as a function of wavelength, for snow particles with different effective radii  $r_e$ . Circles and corresponding error bars are measurements of spectral albedo reported by Grenfell et al. [1994] for Antarctic snow. (b) Broadband albedo as a function of solar zenith angle for the same snow particles as in (a).

latter and our study is the atmospheric part of DAK determining the irradiances arriving at the snow surface.

In figure 3.3, we show the spectral and broadband albedos of snow for different  $r_e$  and  $\theta_0$ , as calculated by DAK. An examination of various sources done by Wiscombe and Warren [1980] suggests that fine, new snow has a radius of 20–100  $\mu\text{m}$ . Older, fine-grained snow has a radius of 100–300  $\mu\text{m}$ . Here we present results for  $r_e = 50, 100$  and  $200 \mu\text{m}$ .

Mie scattering theory predicts that the larger a particle, the more of the scattered light is directed in the forward direction. Snow consisting of large grains will scatter the incoming solar radiation further into the snowpack than snow consisting of small grains. Effectively, the path length of the radiation through the snowpack increases for larger grains. As the radiation passes through more ice when the path length is increased, the albedo will drop, both spectral and broadband. This behaviour is reproduced by our ray-tracing snowpack, both for spectral (figure 3.3(a)) and broadband (figure 3.3(b)) albedo. The decrease of the spectral albedo as a function of  $r_e$  is most notable in the near-infrared (IR) above 800 nm. The broadband albedo for a given  $\theta_0$  is about 0.06 higher for  $r_e = 50 \mu\text{m}$  than for  $r_e = 200 \mu\text{m}$ .

We compare our spectral albedo curves with measurements on Antarctic snow done by Grenfell et al. [1994] in figure 3.3(a). For a grain size of 100  $\mu\text{m}$ , the visible part of the model albedo agrees well with their measurement data. The near-IR albedos are somewhat underestimated however. Grenfell et al. [1994] and Flanner et al. [2007] noted exactly the same

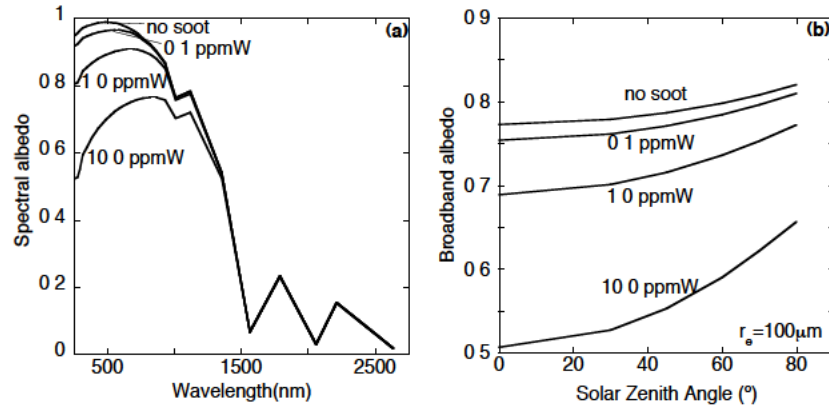


**Figure 3.4:** (a) Spectral albedo as a function of wavelength, for different soot concentrations in a snowpack with  $100 \mu\text{m}$  radius snow grains. (b) Broadband albedo as a function of solar zenith angle for the same snow particles as in (a).

discrepancy and found that the inclusion of a sub-millimeter layer of very small snow grains ( $30 \mu\text{m}$ ) can resolve the difference. They argue that vertical heterogeneity in snow grain size can have strong influence on different spectral regions of albedo. Without such a sub-millimeter layer, a vertically constant  $r_e$  can match a measured broadband albedo, but it will likely underestimate visible albedo and overestimate near-IR albedos somewhat. In chapter 7, we will further investigate this subject.

The solar zenith angle  $\theta_0$  has two effects on both the spectral and broadband albedo. First, for large  $\theta_0$ , the incoming solar radiation is less likely to penetrate deep into the snow, so the path length through the snow is shortened, increasing the albedo. Second, at very large  $\theta_0$ , the radiation becomes almost exclusively diffuse. Diffuse radiation has an effective  $\theta_0$  of about  $50^\circ$  [Wiscombe and Warren, 1980]. This second effect counteracts the first one, but only at  $\theta_0 > 80^\circ$  [Wiscombe and Warren, 1980]; it is not visible in figure 3.3(b). In section 3.4, dealing with clouds, we will see this effect much more clearly at all zenith angles.

### 3.3.2 Soot-contaminated snow

Soot, produced by incomplete combustion of carbon-containing materials, is known to have a possibly large impact on the spectral and broadband albedo of snow [e.g. Warren and Wiscombe, 1980, 1985; Clarke and Noone, 1985; Flanner et al., 2007]. Soot particles are highly absorptive especially in the visual range of solar radiation, where the solar flux is greatest.

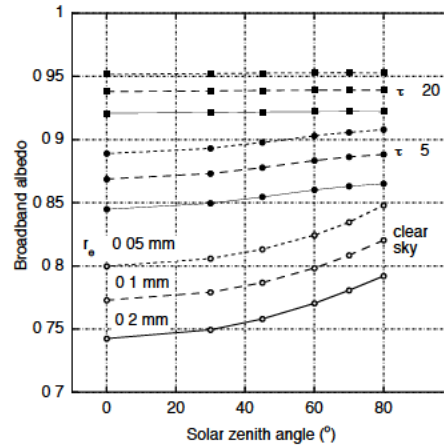


**Figure 3.5:** Broadband snow albedo as a function of solar zenith angle, for three snow grain radii (50, 100 and 200  $\mu\text{m}$ ), for clear sky (open circles), overcast with a cloud of  $\tau = 5$  (solid circles), and overcast with a cloud of optical thickness  $\tau = 20$  (solid squares).

Even a small concentration of soot particles in the snowpack can therefore have a profound effect on the surface albedo, both spectral and broadband. The optical effects of soot have been incorporated into our model by taking scattering and absorption coefficients of soot ( $b_{sca}^a$  and  $b_{abs}^a$ ) from the OPAC (Optical Properties of Aerosols and Clouds) database [Hess *et al.*, 1998b], and using these values to calculate the optical thickness  $b$  and single scattering albedo  $\omega$ , as shown in equations 2.14 and 2.15.

Results of prescribing various concentrations of soot in the DAK snowpack are shown in figure 3.4, using a snow grain size of 100  $\mu\text{m}$ . In the left pane, it is evident that soot has the most pronounced influence on spectral albedo in the visible part of the spectrum, but for larger concentrations, also extending somewhat into the near-IR region. A concentration of 0.1 ppmW (mass fraction), which is typical for seasonal snow cover in much of Eurasia and North America [Flanner *et al.*, 2007], lowers the broadband albedo by 0.015 to 0.02, depending on  $\theta_0$ . At a larger concentration of 1.0 ppmW, occurring in strongly industrialized areas like Eastern China, the reduction of albedo is much more dramatic — up to 0.09 depending on  $\theta_0$ . For most of the polar snow cover, soot concentrations amount to no more than 0.01 ppmW and thus, soot has a very small direct effect on broadband snow albedo.

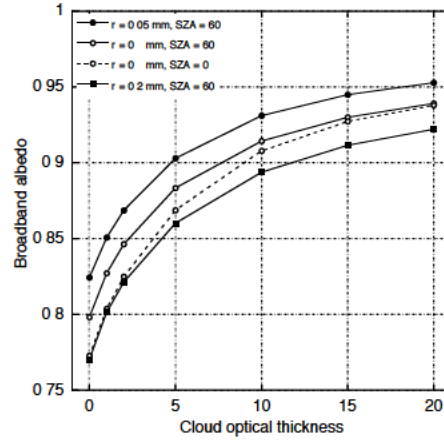


**Figure 3.6:** Broadband snow albedo as a function of cloud optical thickness ( $\tau$ ), for three snow grain radii and a solar zenith angle of  $60^\circ$  (solid lines), and for  $r_e = 100 \mu\text{m}$  and  $\theta_0 = 0^\circ$  (dashed line).

### 3.4 Cloudy-sky snow albedo

As the broadband surface albedo of snow is dependent on the spectral composition of the incoming radiation, it should not be surprising that snow albedo is affected strongly by the presence of clouds. *Liljequist* [1956] and *Rusin* [1961] already reported that snow albedo increases if clouds are present, based on their observations at different sites in Antarctica. Various studies describe how clouds alter the albedo [*Liljequist*, 1956; *Grenfell and Maykut*, 1977; *Wiscombe and Warren*, 1980], namely (1) by making direct radiation diffuse, and (2) by changing the spectral composition of the solar radiation arriving at the snow surface. Regarding (1), diffuse radiation has an effective zenith angle of about  $50^\circ$  [*Wiscombe and Warren*, 1980], and following the model experiments in section 3.3.1, snow albedo should therefore decrease in the presence of clouds for  $\theta_0 > 50^\circ$ , and increase for  $\theta_0 < 50^\circ$ . The second (spectral) effect, however, dominates over the first effect for all  $\theta_0$ . Clouds consist of water and/or ice particles, and is therefore optically similar to snow for solar radiation. Clouds filter out exactly those wavelengths for which the spectral albedo of snow is low. The broadband albedo, integrated over all wavelengths, increases as a result. Results from DAK with a cloud layer over the snow surface are shown in figures 3.5 and 3.6.

Figure 3.5 shows that clouds of increasing optical thickness ( $\tau$ ) increase the broadband albedo of snow, for all solar zenith angles. The dependence of broadband albedo on solar zenith angle largely disappears for thicker clouds, as a larger fraction of the radiation at the surface will be

diffuse. At a given solar zenith angle, the difference between albedo for different snow grain radii also becomes somewhat smaller (see also figure 3.6). For an optically thick cloud cover, albedos can easily exceed 0.9, and even 0.95.

In figure 3.6, broadband snow albedo is plotted against cloud optical thickness, for a given solar zenith angle  $\theta_0$  of  $60^\circ$  (solid lines). As cloud optical thickness increases, broadband albedo tends to an asymptotic value. The dashed line in figure 3.6, representing broadband albedo for  $\theta_0 = 0^\circ$ , once more illustrates that the  $\theta_0$ -dependence of albedo vanishes as  $\tau$  increases.



## Analysis of clear-sky Antarctic snow albedo

### Summary

The radiative transfer model DAK has been applied to radiation data (1998–2001) from weather stations in different climate regimes in Antarctica. The novel approach of applying the model to multiple-year field data of clear-sky albedo from five locations in Dronning Maud Land, Antarctica, reveals that seasonal clear-sky albedo variations (0.77–0.88) are dominantly caused by strong spatial and temporal variations in snow grain size ( $r_e$ ). Modelled summer season averages of  $r_e$  range from 22  $\mu\text{m}$  on the Antarctic plateau to 64  $\mu\text{m}$  on the ice shelf. Maximum monthly values of  $r_e$  are 40–150% higher. Other factors influencing clear-sky broadband albedo are the seasonal cycle in solar zenith angle (at most 0.02 difference in summer and spring/autumn albedo), and the spatial variation in optical thickness of the cloudless atmosphere (0.01 difference between ice shelves and plateau). The seasonal cycle in optical thickness of the atmosphere was found to be of minor importance ( $<0.005$  between summer and spring/autumn).

---

This chapter is based on Kuipers Munneke, P., C. H. Reijmer, M. R. van den Broeke, P. Stammes, G. König-Langlo and W. H. Knap (2008), Analysis of clear-sky Antarctic snow albedo using observations and radiative transfer modeling, *J. Geophys. Res. (D)*, **113**, D17,118, doi:10.1029/2007JD009653.

## 4.1 Introduction

In chapters 2 and 3, we have presented a combined snow-atmosphere model that we can use to study spectral and broadband radiative transfer of sunlight in an atmosphere that contains absorbing and scattering gases, clouds, and aerosols, and that is bounded below by a snow surface. In this chapter, we will apply this model to four years of continuous field observations gathered at Neumayer station, and by four automatic weather stations (AWSs) situated at locations in various climatic regimes in Dronning Maud Land, Antarctica (see map in figure 4.1).

From these observations, we know that the broadband albedo of the snow surface  $\alpha$  is highly variable throughout the year. Despite the high values of snow albedo in Antarctica (typically 0.78–0.86), the shortwave radiation balance plays a dominant role in the summer energy budget of the snow surface [e.g. *Van As et al.*, 2005b]. The amount of absorbed shortwave radiation, being proportional to  $1 - \alpha$ , is very sensitive to small changes in the snow albedo. It is therefore vital to understand what factors have a strong influence on snow albedo and which have not. The central goal of this chapter is to identify and quantify these factors, using the radiative transfer model DAK. This provides a deeper understanding of the most relevant causes of observed variations in snow albedo.

## 4.2 Data and methods

### 4.2.1 Data sets

We selected the radiation data available from five different locations in Dronning Maud Land, Antarctica. One of these locations is Station Neumayer, which has been delivering high-quality, year-round measurements to the Baseline Surface Radiation Network (BSRN) [*Ohmura et al.*, 1998] since 1994. The other four locations are automatic weather stations (AWSs) that have been collecting both radiation and meteorological data autonomously since 1998 [*Van den Broeke et al.*, 2004a].

Station Neumayer, an Antarctic base operated by Germany since 1981, is situated in Dronning Maud Land (70°37' S, 8°22' W), on the Ekström Ice Shelf at 42 m above sea level (figure 4.1). The Ekström Ice Shelf has a homogeneous and flat surface with a very small slope upward to the south. A thorough description of the climatology of Neumayer is available in *König-Langlo et al.* [1998].

IMAU has been employing more than 10 AWSs (numbered AWS 1, 2, etc.) in Antarctica over the past decade. We chose a set of four of these that cover distinct climatic regions in Dronning Maud Land, and that have a data record of appreciable length:

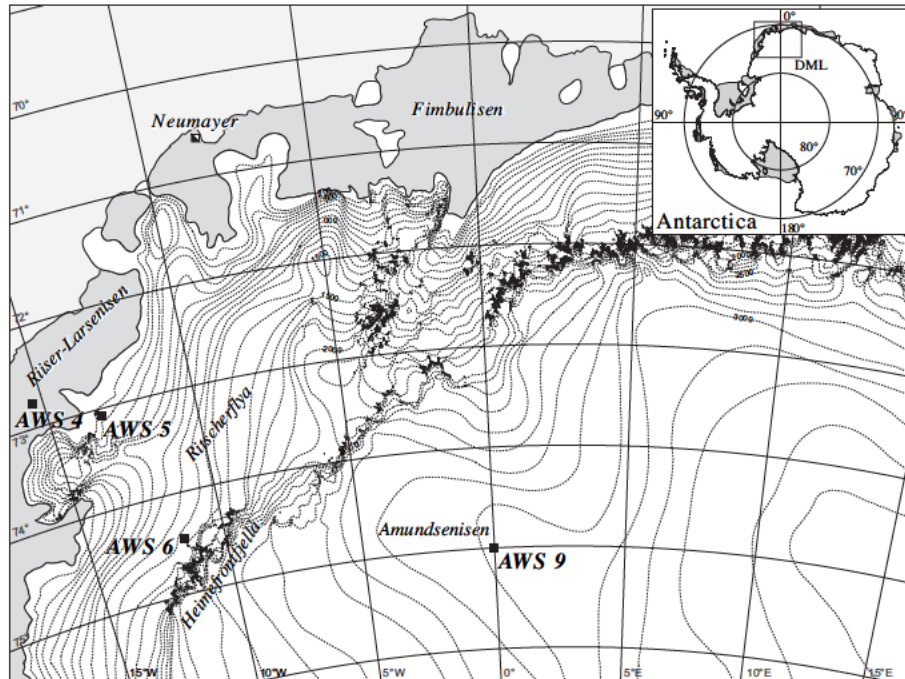


**Figure 4.1:** Location of Station Neumayer and the four AWSs, Dronning Maud Land, East Antarctica. Elevation contours are plotted at 100 m intervals.

1. AWS 4 ( $72^{\circ}45.2' \text{ S}$ ,  $15^{\circ}29.9' \text{ W}$ , 34 m a.s.l.) on the Riiser-Larsen Ice Shelf, about 80 km from the ice shelf front,
2. AWS 5 ( $73^{\circ}06.3' \text{ S}$ ,  $13^{\circ}09.9' \text{ W}$ , 363 m a.s.l.) just inland of the Riiser-Larsen Ice Shelf grounding line on the coastal slope of the East Antarctica Ice Sheet,
3. AWS 6 ( $74^{\circ}28.9' \text{ S}$ ,  $11^{\circ}31.0' \text{ W}$ , 1160 m a.s.l.) in the escarpment region near Heimefrontfjella, characterized by persistent katabatic winds,
4. AWS 9 ( $75^{\circ}00.2' \text{ S}$ ,  $0^{\circ}00.4' \text{ E}$ , 2892 m a.s.l.) on the East Antarctic Plateau (Amundsenisen).

Surface melt only occurs at Station Neumayer and AWSs 4 and 5, very infrequently between November and February, usually for only one day or a few days at a time. Surface melt at AWS 4 and 5 amounts to  $19 \text{ mm w.e. a}^{-1}$  for the period 1998–2001 [Van den Broeke *et al.*, 2004b]. One short event was observed at AWS 6 in the four years considered here, in mid-January 1999.

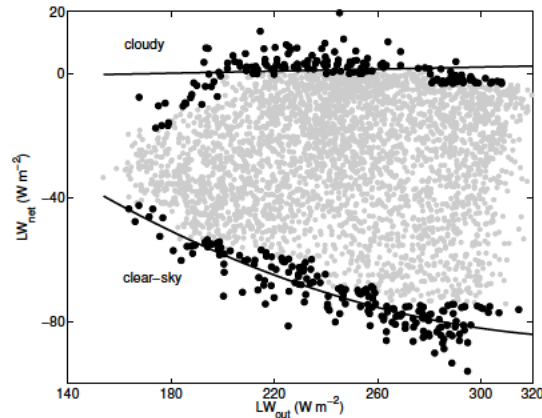


**Figure 4.2:** Diurnal averages of net longwave radiation  $LW_{net}$  at the surface versus upwelling longwave radiation  $LW_{\uparrow}$  for the dataset of Station Neumayer. A straight line and a parabola was fitted to the 95<sup>th</sup> and 5<sup>th</sup> percentile respectively, binned in  $20 W m^{-2}$  intervals of  $LW_{\uparrow}$ .

For this study, data from 1 January 1998 to 31 December 2001 (4 years) were selected. Post-2001 data from the AWSs used in this study have not yet been analysed thoroughly enough for inclusion in this study. Hourly values of meteorological observations and radiation measurements are available for all measurement locations [e.g. König-Langlo and Herber, 1996; Van den Broeke et al., 2004a]. From Neumayer, year-round, three-hourly synoptic observations of the meteorological conditions according to WMO standards are available, including a description of snow drift. We exclude data between April and September, when the solar elevation is so low that the quality of the data and model performance are challenged.

It should be noted that the data from Neumayer, being a year-round manned research station, is considered superior to the data from the AWSs, which collect data autonomously and get serviced only once a year. Various data processing techniques have been applied to improve the AWS data sets [Van den Broeke et al., 2004c], and especially daily and monthly averages of data are considered to be of good quality.

#### 4.2.2 Radiation data and selection of clear days

The observed incoming and outgoing shortwave radiation at the surface have a considerable variability at hourly resolution. This is mainly due to rapid changes in cloud cover, windspeed and associated snow drift. Moreover, the pyranometers have a poor cosine response at very large  $\theta_0$ , reducing their reliability above  $\theta_0 = 80^\circ$ . Especially when calculating the surface

albedo using individual pairs of hourly  $SW_{\uparrow}$  (reflected shortwave radiation) and  $SW_{\downarrow}$  (global shortwave radiation), the errors in the albedo values become rather large at higher  $\theta_0$ . We therefore resorted to daily averages, whereby the albedo averaged over 24 h is calculated using the daily accumulated  $SW$ -fluxes.

Daily averages of cloud cover  $N_e$  are estimated using the longwave ( $LW$ ) fluxes, for consistency also at Neumayer where synoptic observations are being carried out. Despite extreme care, synoptic observations do suffer from some subjectiveness. Moreover, synoptically obtained cloud cover may not always reflect the governing radiation balance, e.g. when the sky is fully covered with very thin clouds through which the sun disk is still visible, or when a thin layer of fog is present close to the surface.

We calculated 24 h-averaged cloud cover by plotting  $LW_{net}$  ( $= LW_{\uparrow} + LW_{\downarrow}$ ) against  $LW_{\uparrow}$  (see figure 4.2). Positive fluxes are defined towards the surface. We fit a parabola and a straight line to the 5<sup>th</sup> and 95<sup>th</sup> percentile of daily averaged  $LW_{\uparrow}$  [see also *Van den Broeke et al.*, 2004c, 2006]. The highest percentile corresponds to the most cloudy days ( $N_e = 1$ ), as the snow surface is in thermal equilibrium with the warm cloud base under cloudy conditions — then  $LW_{net}$  is approximately zero. The lowest percentile of the data points correspond to the days with clearest sky ( $N_e = 0$ ). A linear interpolation between the two fitted lines gives an estimate of the fractional cloud cover for all data points. From the total data set, a clear-sky ( $N_e < 0.2$ ) subset is distilled, which are from now on referred to as clear days, or as clear-sky conditions. The choice for  $N_e = 0.2$  is arbitrary from a physical point of view, but necessary for a data set of sufficient size.

### 4.2.3 Water vapour column sensitivity

Before the model is applied to field data, the sensitivity of modelled albedo to the atmospheric composition — and most notably the water vapour column — must be investigated. Throughout the year, water vapour is the most strongly varying absorbing gas in the (polar) atmosphere. Measurements on Antarctica [e.g. *Van den Broeke et al.*, 2004a] reveal a factor 5 to 10 difference between summer and winter surface specific humidity. This is primarily due to the strong dependence of water vapour concentration on temperature through the Clausius-Clapeyron relation. As water vapour absorption bands are concentrated in the near-IR, the broadband (spectrally integrated) albedo at the ground may increase when the water vapour column is thicker. The magnitude of this effect is modelled using DAK, and demonstrated in figure 4.3 as the two solid lines, showing two model runs with a standard subarctic summer and subarctic winter atmosphere [*Anderson et al.*, 1986]. For all  $\theta_0$ , the difference in broadband albedo is about 0.013.

This effect can also be caused by differences in surface elevation. High on an ice sheet plateau, the atmosphere contains far less water vapour than in coastal regions or on ice shelves.

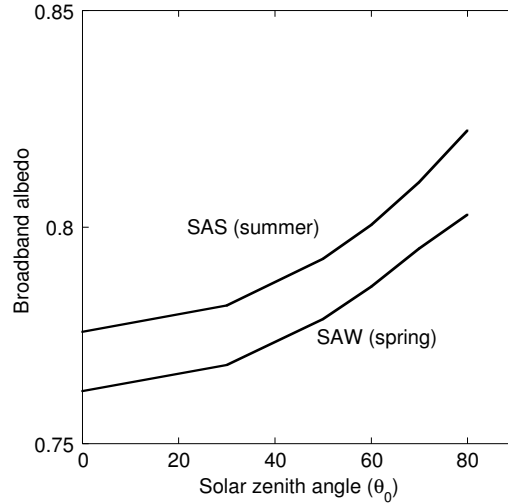


**Figure 4.3:** Broadband albedo as a function of solar zenith angle. SAS = standard subarctic summer atmosphere, SAW = standard subarctic winter atmosphere. The SAW atmosphere may be assumed to represent Antarctic spring conditions.

#### 4.2.4 Vertical atmospheric profiles

The vertically-integrated water vapour content in the atmosphere varies strongly from month to month, due to its strong dependence on air temperature. In order to take into account the resulting seasonally varying optical thickness of the atmosphere, a vertical profile of temperature, pressure, and specific humidity is prescribed for each month for each location. These vertical profiles are extracted from the 25-year model run with RACMO2/ANT, a regional atmospheric climate model at  $\sim 55$  km horizontal resolution, adapted to Antarctic conditions [Van den Berg *et al.*, 2006]. To select only clear-sky profiles, vertically-integrated cloud content from the RACMO2/ANT model was used as a selection criterion.

Thus, we have a set of clear days from the field data, and another set of clear days from the atmospheric model output. These days are not necessarily the same, but it is assumed that monthly averaged vertical profiles are well comparable: in figure 4.4, temperature and specific humidity from the model is compared with monthly averages of clear-sky weather balloon launches at Neumayer. Absolute differences between model and balloon profiles are also plotted. Profiles of temperature and specific humidity at other locations in other months show similar agreement. The balloon and model profiles of temperature differ by at most 3.1 K, and water vapour concentrations by 270 ppmV at the surface. Broadband surface

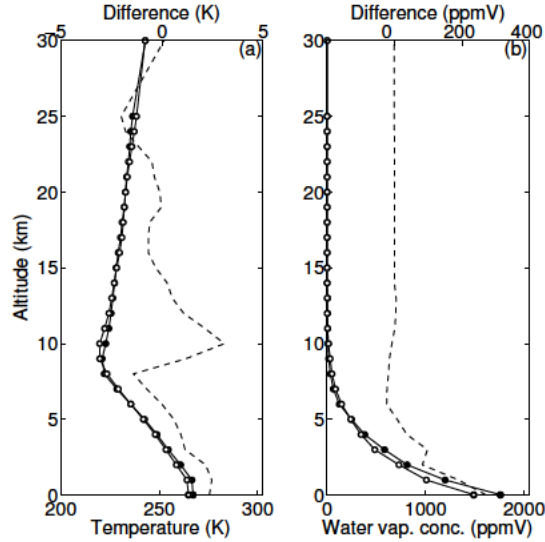


**Figure 4.4:** Monthly averaged vertical atmospheric profiles of temperature (a) and water vapour (b) from Neumayer balloon data (solid dots) and RACMO2/ANT model output (open dots). The dashed lines are the difference between balloon and RACMO2/ANT data, with corresponding scales on the upper x-axes. Shown here are the average January profiles for clear days.

albedo calculated with the balloon sounding data is only 0.001 larger than in the case with RACMO2/ANT model profiles, so application of the model profiles is justified.

## 4.3 Results

### 4.3.1 Observed monthly averaged albedo

Monthly averages of observed broadband clear-sky albedo for all locations are plotted in figure 4.5. To a varying extent, the albedo decreases from October to January and increases from January to March. Part of this behaviour can be explained by the annual cycle in daily averaged  $\theta_0$ , but there are other effects playing a potentially important role: (1) in summer it will be warmer, so that snow metamorphism can take place faster. Moreover, temperature gradients in the snowpack are likely larger, which has been shown to be of key importance for snow metamorphism too [Flanner and Zender, 2006]. The average snow grain size could therefore vary strongly, which influences albedo (we will show in section 4.3.2 that this is a major effect); (2) the vertical water vapour column in the atmosphere increases in the summer months, which is a counteracting effect as it increases albedo in the summer months. Using

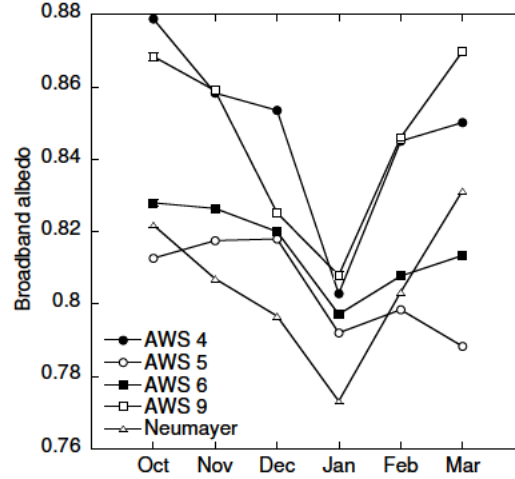


Figure 4.5: Average monthly values of observed clear-sky broadband albedo.

DAK for the snow and atmosphere, we can disentangle the effects of variations in  $\theta_0$ ,  $r_e$  and water vapour content on the observed albedo, as described in the following section.

### 4.3.2 Albedo variations and the role of snow grain size

Taking the atmospheric profiles from RACMO2/ANT, and calculating the monthly averaged  $\theta_0$  for every location, we can calculate the model broadband surface albedo. Monthly values of  $\theta_0$  are calculated by averaging hourly values of  $\theta_0$  weighted by  $SW_{\downarrow}$ .

First, we assess what the influence of the annual variation in water vapour concentration is on the surface albedo. This is shown in figure 4.6 as solid squares (AWS 6) and dots (AWS 4). The solid squares and dots represent model calculations in which monthly averaged atmospheric profiles from RACMO2/ANT are adopted. The lines in figure 4.6 represent theoretical surface albedo at AWS 6 for a standard subarctic summer (SAS) and winter (SAW) atmosphere and a constant  $r_e$  of  $100 \mu\text{m}$ . The albedos calculated with RACMO2/ANT atmospheres are lower than the SAS and SAW atmospheres since the water vapour column in the RACMO2/ANT atmospheres is thinner. The fact that the RACMO2/ANT curve is flatter than the SAS and SAW curves shows the effect of seasonal variations in water vapour concentration — which is only minor ( $< 0.005$ ). The spatial effect (thicker atmospheres and lower  $\theta_0$  at the coast than inland) is larger (0.005–0.01), as is shown by the solid dots in the

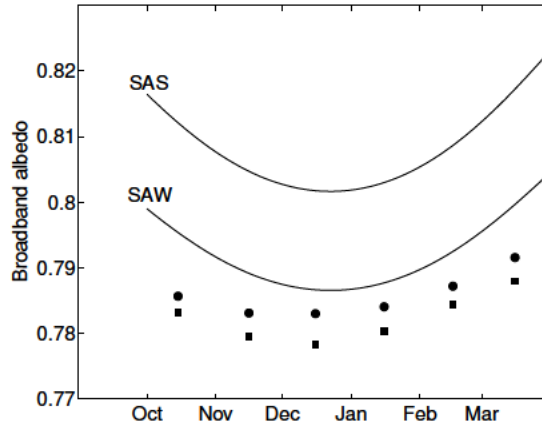


**Figure 4.6:** Modelled broadband albedo as a function of month (and hence,  $\theta_0$ ). The solid lines represent calculations for a constant standard subarctic summer (SAS) and subarctic winter (SAW) atmosphere. The solid squares (AWS 6) and dots (AWS 4) are model calculations using RACMO2/ANT monthly averaged atmospheres. Snow grain size is constant at  $100 \mu\text{m}$  in this figure.

same figure for AWS 4.

Secondly, the influence of the snow grain size  $r_e$  is assessed. For a range of snow grain sizes, model calculations of albedo have been made using location-specific atmospheric profiles and  $\theta_0$ . An example of these calculations is shown in figure 4.7 for Neumayer. The curves shown in figure 4.7 would be the broadband albedo at Neumayer if  $r_e$  would remain constant. Now that  $\theta_0$  and the state of the atmosphere have been fixed, there is only one variable in the model that can be adjusted to make the model and observations agree: the snow grain size  $r_e$ . We can deduce the snow grain size for each measured value of monthly averaged albedo by varying  $r_e$  until model result and observation are the same. The result for all locations is shown in figure 4.8. A common feature is the seasonal variation in  $r_e$  at all stations, with higher values of snow grain size in January. This is likely due to enhanced snow metamorphosis at higher temperatures. From Neumayer via AWS 5 and 6 to AWS 9, there is a decrease in snow grain size from the coast to the plateau. A peculiar exception to this is AWS 4. The high albedo there may be attributed to a combination of very frequent snow fall (totalling  $\sim 390 \text{ mm w.e. a}^{-1}$ ), rime formation on the surface due to frequent fog, and fairly low temperatures due to its southward location well away from the coast. All these conditions hint to the fact that snow grain sizes may be very low on average.

The albedo at AWS 5 and 6 does not rise after January, and this implies larger snow grains even in late summer. This may be coincidental: snowfall accumulation is confined to a few

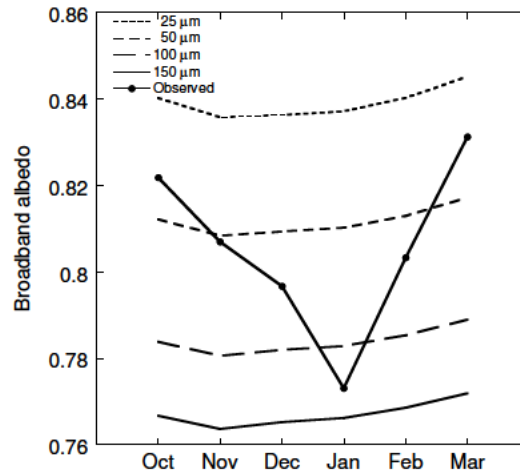


**Figure 4.7:** Calculated seasonal cycle of broadband albedo for Neumayer for several constant values of snow grain size  $r_e$ . The variation in atmospheric conditions and solar zenith angle have been taken into account. The solid line with dots represent measured values of monthly-mean clear-sky albedo at Neumayer.

big events per year, and from 1998 to 2001, these events did not occur between January and March [Van den Broeke *et al.*, 2004b]. The surface snow grains will therefore continue to grow.

## 4.4 Discussion

In analyzing the drivers of snow albedo variations, some assumptions have been made. Some of these assumption were necessary due to the design of the radiative transfer model (e.g. that the surface is flat) and some were made because they are judged to make no significant changes to the main conclusions (e.g. that soot concentrations are negligibly small). We will briefly touch upon various of these assumptions.

### 4.4.1 Soot

Soot concentrations have been assumed to be negligible. Soot concentrations are allegedly low in Antarctic snow, except perhaps downwind from research stations where locally pro-

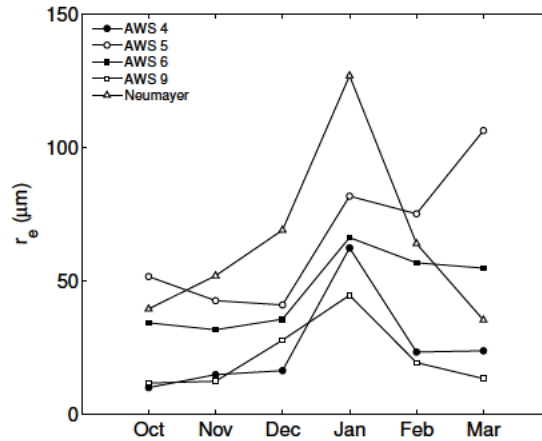


**Figure 4.8:** Average monthly values of snow grain size  $r_e$  ( $\mu\text{m}$ ) determined from observed clear-sky albedo. With these values for  $r_e$ , model and observations are in agreement, taking into account the effects of seasonally varying  $\theta_0$  and atmospheric profiles.

duced soot may have contaminated the snowpack [e.g. Warren and Clarke, 1990]. Atmospheric concentrations of black carbon (BC) measured at Neumayer are very low (in the order of  $2 \text{ ng m}^{-3}$  [Rolf Weller, *personal communication*]), suggesting that neglecting any impurities in the snowpack is reasonable, certainly for the remote AWSs.

#### 4.4.2 Sastrugi and wind ripples

When the sun azimuth is aligned perpendicular to wind ripples and sastrugi at the snow surface, measured values of albedo can differ up to 4% from the situation in which sastrugi and solar azimuth are aligned parallel [Carroll and Fitch, 1981]. This effect tends to average out when sufficiently large spatial and temporal averages are considered [Grenfell et al., 1994]. In our case, sastrugi are relatively small-scale features in comparison to the field-of-view of the pyranometers (typically  $600 \text{ m}^2$  for an instrument level of 2.5 m above the surface). Moreover, sastrugi constantly change their location and orientation. Sunlit and shadowed fractions of the surface due to sastrugi will be evenly represented in the instrument field-of-view for monthly averages of albedo as we use in this study.

### 4.4.3 Inclination of the snow surface

A small inclination of the surface can have a large impact on measured albedo, especially at large  $\theta_0$ . In the case of daily or monthly averages, only the tilt component in the North-South direction is affected (see *Grenfell et al.* [1994] for example calculations). Large-scale tilt at all stations happens to be approximately in the North-South direction, varying from very small ( $< 0.1^\circ$  at Neumayer, AWS 4 and 9) to  $1.5^\circ$  at AWS 6. However, these are values derived from large-scale digital elevation maps, and only true on scales of several kilometers. Actual values for the surface in the sensor field-of-view are in fact unknown, but likely smaller than  $1^\circ$  in any direction, because any larger slope would be clearly detectable in the field. As a worst-case scenario calculation, we suppose a slope of  $1^\circ$  and  $\theta_0 = 80^\circ$ . The daily mean albedo is then off by 1.8% and errors in the inferred values of  $r_e$  would, in this case, be roughly 40%. This error decreases rapidly for lower  $\theta_0$  and flatter surfaces. For a slope of  $0.1^\circ$  and  $\theta_0 = 80^\circ$ , the error in albedo decreases to 0.2% and the error in  $r_e$  would be 4%.

### 4.4.4 In-situ validation of snow grain size

Although the seasonal variation in snow grain size that we found is realistic and plausible, it turns out to be very difficult to independently verify whether this annual variation in snow grain size is realistic – information about  $r_e$  at the measurement locations is non-existent. Recent accounts of snow grain sizes in the area are found in *Gay et al.* [2002] and *Kärkäs et al.* [2002], but are not readily convertible to an optically equivalent snow grain size due to different measurement techniques or different definitions of snow grain size.

Recent work from *Scambos et al.* [2007], using radiances from the MODIS satellite sensors to retrieve snow grain size, suggests that summer-averaged (December–February) grain sizes range from  $76 \mu\text{m}$  at AWS 9 to  $213 \mu\text{m}$  at Neumayer. A comparison between our results and the MODIS-derived snow grain sizes (both averages for the Dec – Feb period) is shown in figure 4.9. Although there is a good correlation between the two, the MODIS-derived  $r_e$  is more than twice as large. The MODIS product calculates one value for  $r_e$  from images obtained throughout the summer — it therefore implicitly assumes that  $r_e$  is constant throughout the year. It could therefore be that *Scambos et al.* [2007] obtain larger snow grains when there is a bias towards January scenes; or that in the months in which the MODIS product was acquired (Dec 2003 – Feb 2004), snow grains were on average larger. More research is required to explain the discrepancy.

## 4.5 Summary and conclusions

In this chapter, we have used a radiative transfer model DAK for calculating the albedo of snow surfaces. The radiative transfer model has been applied to a 4-year data set of solar

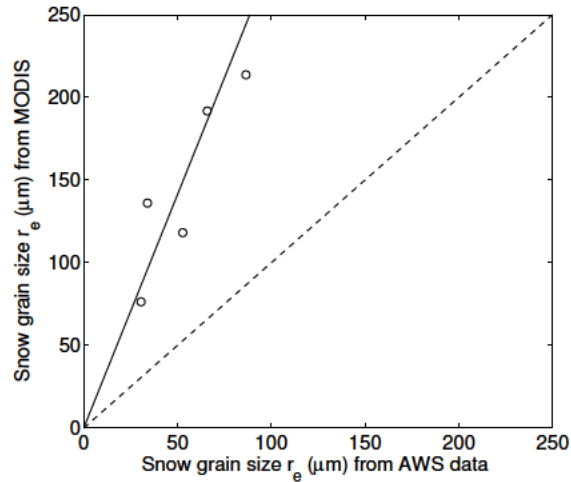


**Figure 4.9:** Snow grain sizes obtained from AWS data (Dec–Feb averages) on the horizontal axis, compared to MODIS-derived snow grain sizes (vertical axis). The solid line, having a slope of 2.81, is a linear fit to the data points forced through the origin.

radiation and snow albedo, recorded at Station Neumayer and four AWSs in Dronning Maud Land, Antarctica. From these data sets, clear-sky subsets were extracted using the longwave radiation balance as a selection criterion. Application of the model has revealed that the annual cycle in observed broadband snow surface albedo at clear days cannot be explained by variations in the solar zenith angle alone, but that varying snow grain size must have influenced the temporal differences in albedo. These temporal differences are a robust finding. The seasonal variation in water vapour concentration at a given location turns out to play a minor role. Spatial differences in atmospheric composition (water content) can cause more significant differences in albedo, however.

An inherent limitation in our current application of the model is that reasonably, only longer timescale variability can be assessed and interpreted. If the model is to be used on short time scales (daily or even hourly variations), better and more measurements (e.g. higher-quality shortwave radiation measurements, cloud cover observations) need to be available in a high temporal resolution. For all radiation measurements, and for unmanned AWSs even more so, it is difficult if not impossible to quantify the effects of wind and snow drift on the radiation balance. One improvement in the model snowpack would however be the incorporation of snow metamorphism laws, on the lines of *Flanner and Zender* [2006]. It would make the model more effective on the short time scales.

The application of this method is not strictly limited to East Antarctica — it does apply to dry-snow surfaces in general, as long as reliable shortwave radiation measurements are available.

Soot and dust concentrations can be prescribed. Practical applications will include East and West Antarctica, the dry-snow zone of Greenland, and spring snow cover on other ice caps and tundras, but exclude surfaces with melt, heavy undulations, patchy snow, or ice surfaces.

With a growing contribution of remote sensing to the study of solar radiation in the snow-atmosphere system, it is of great importance to apply a uniform method of ground-truthing of snow properties. In the absence of this, we have shown that estimates of, and trends in, snow grain size can be obtained by combining model calculations with field measurements of radiative fluxes. A next step would therefore be to apply DAK to a data set where all parameters relevant to albedo variations, *including* direct measurements on snow grain sizes, are measured simultaneously. In this way, a 'closure' of the model can be achieved.

## Cloud properties from radiation measurements over snow and ice

### Summary

We critically review and improve a simple method to extract year-round records of cloud optical thickness from radiation measurements made by automatic weather stations (AWSs) over snow and ice surfaces. A ‘longwave-equivalent cloudiness’,  $N_{\epsilon}$ , obtained from longwave radiation measurements, is combined with the effective cloud optical thickness,  $\tau$ , from shortwave data, to obtain consistent, year-round information on cloud properties. The method is applied to radiation data from six AWSs in Dronning Maud Land, Antarctica, and the ablation area of the West-Greenland ice sheet. The good correlation between daily-mean  $N_{\epsilon}$  and  $\tau$  for all locations ( $0.73 < r < 0.91$ ) shows that shortwave radiative properties of clouds can be inferred using longwave radiation even in the absence of solar radiation itself. An error analysis shows that retrievals of  $\tau$  are sensitive to the quality of the input data, but accurate within 7.5% for a 2% uncertainty in clear-sky incoming solar radiation. As three applications of the method, we discuss the influence of clouds on the radiation budget (Application I), the relation between cloud cover and broadband albedo (II) at the six AWS locations, and we demonstrate the possibility to detect trends in  $\tau$  in longer data series (III). About 1/3 of the attenuation of solar radiation by clouds is compensated by multiple reflections between the high-albedo surface and the cloud base (Appl. I). Cloudy-sky surface albedo is higher than the clear-sky albedo for snow surfaces but not for ice (Appl. II): over snow surfaces, clouds deplete near-infrared radiation and thus increase the broadband albedo. Ice surfaces, have a much lower albedo for visible radiation, weakening this enrichment of visible radiation and thus the increase of broadband albedo. The method is used to detect a trend of decreasing  $\tau$  in the long time series from Neumayer in the period 1995–2004 (Appl. III).

---

This chapter is based on Kuipers Munneke, P., C. H. Reijmer and M. R. van den Broeke (2009), Assessing the retrieval of cloud properties from radiation measurements over snow and ice. *Submitted to Int. J. Climatol.*

## 5.1 Introduction

The influence of Earth's climate on glaciers and ice sheets is enforced through the surface energy budget (SEB), whose dominant terms are the longwave and shortwave radiative fluxes. The SEB strongly influences the summer surface mass balance of glaciers and ice sheets in their ablation areas, as it largely determines the rate and amount of melt. If meltwater runoff exceeds mass gain by precipitation, sea level will rise. Small glaciers have been contributing to sea-level rise in this way already since the Little Ice Age [e.g. *Dyurgerov and Meier*, 2005]. Recent studies indicate that the Greenland ice sheet is also contributing to sea-level rise [*Shepherd and Wingham*, 2007], both by means of a decreasing surface mass balance [*Box et al.*, 2006] and through ice-dynamical effects that are possibly triggered by meltwater input [*Rignot et al.*, 2008]. Knowledge of the SEB of glaciers and ice sheets is therefore important.

The SEB is greatly altered in the presence of clouds. The longwave radiation emitted to the surface will increase, since the emissivity of clouds is higher than that of a clear sky. The shortwave radiation field is rather complex in the presence of clouds, especially over highly reflective surfaces such as snow and ice. First of all, clouds reduce the incoming radiation flux by reflection and absorption. Secondly, the radiation that passes through the cloud will be subject to multiple reflections between the surface and the cloud base [*Ångström and Tryselius*, 1934; *Schneider and Dickinson*, 1976; *Shine*, 1984]. Since the spectral albedo of snow (and ice) and the absorption of radiation by clouds are both strongly dependent on wavelength [*Liljequist*, 1956; *Wiscombe and Warren*, 1980], the magnitude of cloud effects is also very much wavelength-dependent — clouds not only alter the intensity, but also the spectral composition of the solar radiation arriving at the surface. At the same time, spectrally-integrated (broadband) albedo has been observed to increase in the presence of clouds [*Liljequist*, 1956; *Ambach*, 1974]. All these phenomena have competing effects on the shortwave radiation budget of the snow surface.

An outstanding problem in the study of clouds is the lack of cloud observations over ice sheets. From satellite data, it is difficult to infer properties of clouds because clouds and snow appear very similar both in the solar spectrum as in their thermal properties [e.g. *Town et al.*, 2007]. This hampers the study of clouds over ice sheets. The increasing amount of Automatic Weather Stations (AWS) on glaciers and ice sheets [*Stearns and Wendler*, 1988; *Allison et al.*, 1993; *Van den Broeke et al.*, 2004a, 2008a] are a possibly valuable source of information from remote locations, that could make more data on cloud properties available.

The attempt to obtain cloud properties in polar regions using ground-based measurements is not new. *Mahesh et al.* [2001] use a Fourier transform interferometer to determine cloud optical thickness at South Pole station. *Long and Ackerman* [2000] present a method to estimate cloud fraction ( $N$ ) using global and diffuse solar radiation measurements, which limits the application to daytime periods, and to locations where diffuse shortwave radiation is measured. *Marty and Philipona* [2000] present the Clear-Sky Index to separate clear and

cloudy skies using longwave radiation measurements, the derivation of which is to a large extent based on *Konzelmann et al.* [1994]. *Dürr and Philipona* [2004] extend the Clear-Sky Index to an algorithm that retrieves  $N$  from downwelling longwave measurements. A caveat of the traditional cloud fraction  $N$ , be it observed by a meteorologist or retrieved using an algorithm, is that it does not necessarily provide an accurate description of the radiative properties of the cloud cover.

In the method central in this chapter, a ‘longwave-equivalent’ cloudiness  $N_{\epsilon}$  is determined from the apparent emissivity of the sky and surface temperature. Similarly, shortwave radiation measurements can be used to obtain the cloud optical thickness,  $\tau$  [*Stephens*, 1984], following a parameterization developed by *Fitzpatrick et al.* [2004]. Cloud optical thickness is defined in terms of cloud microphysical parameters and represents a measure for the amount of radiation that is attenuated by the cloud. Combining the parameterization by *Fitzpatrick et al.* [2004] and the retrieval of  $N_{\epsilon}$ , a simple method is obtained that makes use of radiation measurements from AWSs over snow and ice surfaces to gain knowledge about year-round radiative cloud properties. This method was first used by *Van den Broeke et al.* [2008a] to determine cloud optical properties over Greenland stations, and by *Giesen et al.* [2009] for Mittaldalsbreen and Storbreen, two glaciers in southern Norway.

In this chapter, we will review the method, present some improvements, and subject the method to a critical review of potential uncertainties. As a final part, we demonstrate the versatility of the method in three different applications (section 5.4). The method can be useful (a) to those that wish to extend the amount of information that can be gained from their AWSs, and (b) to those that are looking for validation data of satellite retrievals of cloud optical thickness.

## 5.2 Data and methods

### 5.2.1 Description of data

We use data from six locations, five of which are continuously recording AWSs — three in Greenland and two in Antarctica — and the sixth is the manned BSRN (Baseline Surface Radiation Network, [*Ohmura et al.*, 1998]) station Neumayer in Antarctica (figure 5.1). A short characterization of each of these locations and corresponding data sets is given in Table 5.1. The AWSs, which are part of a larger network of sites [*Van den Broeke et al.*, 2004a, 2008a], were selected for their continuous data sets of radiation, without data gaps caused by e.g. sensor riming, frost accretion, snow accumulation, or instrument malfunction. The three Antarctic locations Neumayer, AWS 5 and AWS 6 (figure 5.1(a)) are located in Dronning Maud Land (East Antarctica) on the ice shelf, the coastal ice sheet and the escarpment region, respectively [*Van den Broeke et al.*, 2004a]. The three Greenlandic stations (figure 5.1(b)) are part of the Kangerlussuaq transect (K-transect), located at the western edge of the Greenland

**Table 5.1:** Specifications for the data sets used in this study.

	Antarctica			Greenland		
	Neumayer	AWS 5	AWS 6	S5	S6	S9
Latitude	70°37' S	73°06' S	74°29' S	67°06' N	67°05' N	67°03' N
Longitude	8°22' W	13°10' W	11°31' W	50°07' W	49°23' W	48°14' W
Altitude (m a.s.l.)	42	363	1160	490	1020	1520
Ice edge dist. (km)	5	105	280	6	38	88
Temperature (°C)	-15.9 <sup>a</sup>	-16.4 <sup>b</sup>	-16.6 <sup>b</sup>	-5.5 <sup>c</sup>	-9.8 <sup>c</sup>	-12.6 <sup>c</sup>
Pyranometer	K&Z <sup>d</sup> CM11	K&Z CM3	K&Z CM3	K&Z CM3	K&Z CM3	K&Z CM3
Pyreometer	Eppley PIR	K&Z CG3	K&Z CG3	K&Z CG3	K&Z CG3	K&Z CG3
Sampl. period (min)	1/60	6	6	6	6	6
Averag. period (min)	1	120	120	60	60	60
Start date of set	1 Jan 1995	1 Jan 1998	1 Jan 1998	28 Aug 2003	1 Sep 2003	1 Sep 2003
End date of set	31 Dec 2004	31 Dec 2001	31 Dec 2001	27 Aug 2007	31 Aug 2007	31 Aug 2007

<sup>a</sup> Annual avg at 2 m level<sup>b</sup> Annual avg at instr level (approx 2 m)<sup>c</sup> Annual avg at instr level (approx 6 m)<sup>d</sup> K&Z = Kipp & Zonen

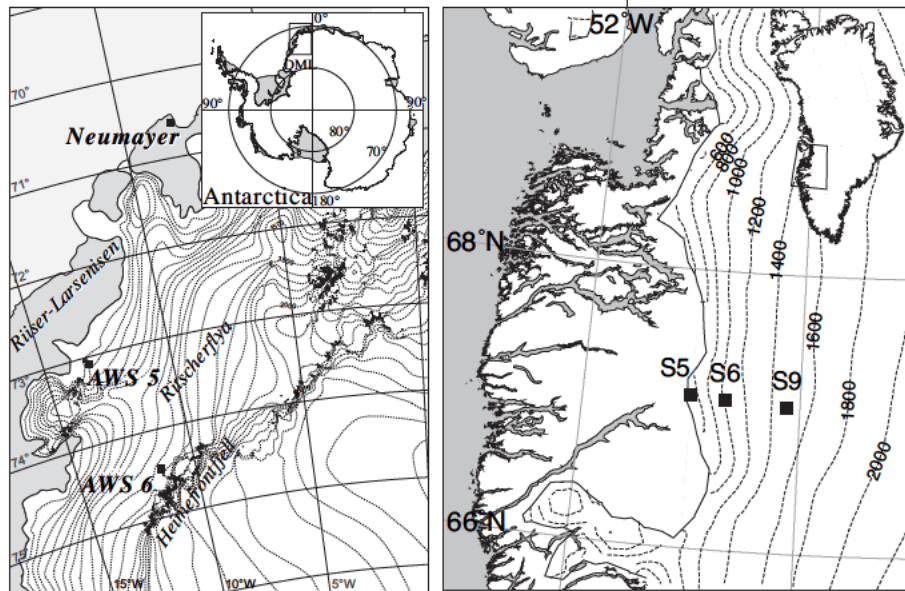


**Figure 5.1:** Map showing the locations of the AWSs and Neumayer Station on Antarctica and Greenland. In Antarctica, 100 m height contours are plotted. In Greenland, 200 m height contours are plotted.

ice sheet [Van den Broeke *et al.*, 2008a]. Stations S5 and S6 are in the lower and middle ablation area respectively, whereas S9 is located close to the equilibrium line.

At all AWS locations, Kipp & Zonen (K&Z) CNR1 radiometers measure all the radiation fluxes. A CNR1 houses four instruments: two CM3 pyranometers measure the incoming and reflected shortwave radiation,  $SW_{\downarrow}$  and  $SW_{\uparrow}$ , and two CG3 pyrgeometers measure downwelling and upwelling longwave radiation,  $LW_{\downarrow}$  and  $LW_{\uparrow}$ . At Neumayer, K&Z CM11 pyranometers and Eppley PIR pyrgeometers are used. Hourly averages are analyzed in this study, apart from AWS 5 and 6 where two-hourly data are used.

Energy considerations make ventilation of the AWS pyranometers unfeasible — but a steady katabatic flow of undersaturated air prevents riming of the sensors [Van den Broeke *et al.*, 2004c]. Some corrections, such as for sensor tilt, have been applied to the radiation data [Van den Broeke *et al.*, 2004a,c, 2008a].

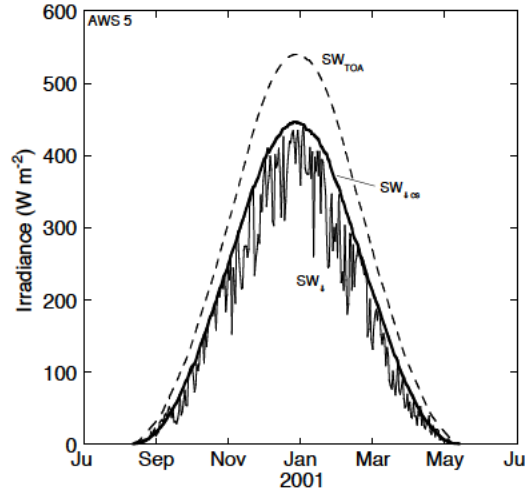


**Figure 5.2:** Daily averages of  $SW_{\downarrow,TOA}$  and  $SW_{\downarrow}$  at AWS 5 in the austral summer of 2000/2001. The maximum incoming radiation at the surface,  $SW_{\downarrow,cs}$ , is calculated as explained in the Data and Methods section (5.2).

### 5.2.2 Cloud optical thickness ( $\tau$ )

The amount of shortwave radiation arriving at the surface,  $SW_{\downarrow}$ , is lower than the amount of downward shortwave radiation at the top of atmosphere (TOA),  $SW_{\downarrow,TOA}$ , due to scattering and absorption of radiation by the atmosphere and by clouds. In order to isolate the scattering and absorption due to clouds from clear-sky scattering and absorption, we use the cloud transmission,  $trc$ , which is the ratio of shortwave incoming radiation at the surface in the presence of clouds,  $SW_{\downarrow}$ , to the amount of radiation that would arrive at the surface without clouds,  $SW_{\downarrow,cs}$

$$trc = \frac{SW_{\downarrow}}{SW_{\downarrow,cs}}. \quad (5.1)$$

This should not be confused with atmospheric transmission, which is the ratio of  $SW_{\downarrow}$  and  $SW_{\downarrow,TOA}$ .

For the calculation of  $trc$ , a value for clear-sky shortwave radiation,  $SW_{\downarrow,cs}$ , is required. For that, we follow the method of *Greuell et al.* [1997], who used expressions from *Meyers and Dale* [1983]. This method relates  $SW_{\downarrow}$  to a series of transmission coefficients that account for Rayleigh scattering, and absorption by water vapour, other molecular gases, and aerosols. The transmission coefficient for aerosol absorption is used to tune the calculated

daily-averaged  $SW_{\downarrow,cs}$  to measured values of  $SW_{\downarrow}$  at clear days. An example of the result of this procedure is shown in figure 5.2 for AWS 5 data. The curve for  $SW_{\downarrow,cs}$  fits as an envelope around the measurements of  $SW_{\downarrow}$ . Data from other stations are not shown but give similar results.

When characterizing the effect of clouds on the surface shortwave radiation budget, it is important to describe a cloud with a quantity that is not dependent on the radiation field itself. In several previous studies [Konzelmann *et al.*, 1994; Bintanja and van den Broeke, 1996], cloud transmission, as defined in Equation 5.1, has been used to characterize the optical properties of the cloud. But, as pointed out by e.g. Shine [1984] and Fitzpatrick *et al.* [2004], cloud transmission is strongly dependent on the zenith angle of the radiation (determining the path length of radiation through the cloud) and on the albedo of the surface: a high surface albedo gives rise to multiple reflections of radiation between the surface and the cloud base. The quantity  $trc$  is therefore not inherent to the cloud. A quantity that *is* inherent to the cloud is the cloud optical thickness,  $\tau$ . Fitzpatrick *et al.* [2004] successfully developed a parameterization for  $trc$  that depends on  $\tau$ , the broadband surface albedo,  $\alpha$ , and the solar zenith angle,  $\theta_0$ :

$$trc = \frac{a(\tau) + b(\tau) \cos \theta_0}{1 + (c - d\alpha)\tau}, \quad (5.2)$$

where  $a$  and  $b$  are functions of  $\tau$ , and  $c$  and  $d$  are constants. This parameterization has been derived using a spectral multiple-scattering radiative transfer model where clouds are prescribed in terms of a cloud droplet distribution and an optical thickness. It doesn't matter that the actual cloud droplet distribution is unknown, since Fitzpatrick *et al.* [2004] achieved a good fit between the radiative transfer model and the parameterization for several cloud droplet distributions. We use the values for  $a$ ,  $b$ ,  $c$  and  $d$  that belong to an equivalent homogeneous clouds with an effective droplet radius of  $8.6 \mu\text{m}$ , as given by Fitzpatrick *et al.* [2004]. As we do not have information on actual cloud microphysical parameters, the  $\tau$  in this paper characterizes the transmission of shortwave radiation and should not be used to infer cloud microphysical properties.

The multiple-scattering radiative transfer model that Fitzpatrick *et al.* [2004] used to derive the parameterization of equation 5.2 is not exactly equal to the DAK model described in chapters 2 and 3. Most notably, Fitzpatrick *et al.* [2004] prescribed spectral albedos instead of calculating them using an optical model for the snowpack, as presented in chapter 3. Nevertheless, it was decided not to try and rederive the parameterization from Fitzpatrick *et al.* [2004] as we do not expect DAK to find significantly different results.

In order to obtain hourly values of  $\tau$ , we use observed hourly values of  $trc$  (from equation 5.1),  $\theta_0$  and  $\alpha$ , and search for a value of  $\tau$  that satisfies Equation 5.2. The retrieved value for  $\tau$  is unique since  $trc$  is a monotonically decreasing function of  $\tau$  for  $\tau \geq 0$ . Next, we calculate daily averages of  $\tau$  when more than 12 hourly values with  $\theta_0 < 85^\circ$  are available.

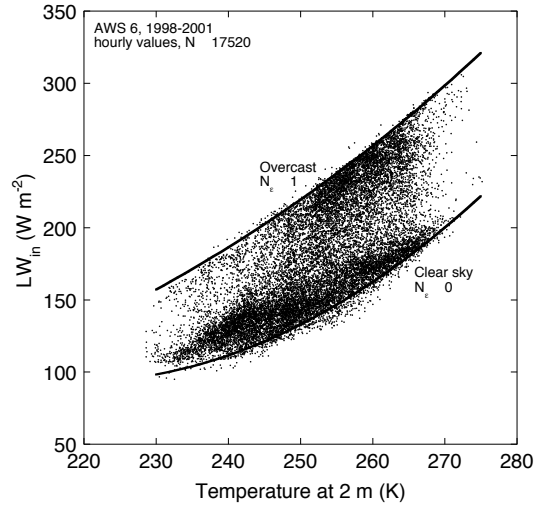


**Figure 5.3:** Scatter plot of air temperature at 2 m against downwelling longwave radiation  $LW_{\downarrow}$ , for hourly data of AWS 6, Antarctica. The upper bound coincides with  $LW_{\downarrow} = \sigma T_{2m}^4$ , the lower bound is a fitted polynomial of second degree. Longwave-equivalent cloudiness  $N_{\epsilon}$  is obtained by linearly interpolating between the two bounds for a given  $T_{2m}$ .

### 5.2.3 Longwave-equivalent cloudiness ( $N_{\epsilon}$ )

The longwave radiation balance measured by an AWS can also be used to obtain a consistent and physically meaningful measure for cloud cover, which we will call ‘longwave-equivalent cloudiness’,  $N_{\epsilon}$  [Van den Broeke *et al.*, 2004c]. It is based on differences in emissivity of a clear atmosphere and a cloudy one. In short, hourly values of downwelling longwave radiation  $LW_{\downarrow}$  are plotted against 2-meter air temperature  $T_{2m}$  for the entire data set of each location (figure 5.3). The upper limit of the scatter plot coincides with  $LW_{\downarrow} = \sigma T_{2m}^4$  (with  $\sigma = 5.67 \times 10^{-8} \text{ W m}^{-2} \text{ K}^{-4}$ , the Stefan-Boltzmann constant) and represents an entirely cloudy sky emitting as a blackbody radiator (emissivity  $\epsilon \approx 1$ ). The lower limit of the scatter plot, which can be approximated by a second-order polynomial, represents clear-sky conditions, characterized by the lowest possible atmospheric emissivities. The lower bound in figure 5.3 is described by a polynomial rather than using a constant clear-sky emissivity, because in polar regions, surface inversions occur frequently, particularly during clear-sky conditions at nighttime and in winter, which makes surface temperature less representative for the vertical temperature structure. A constant emissivity for clear-sky conditions would therefore not hold.

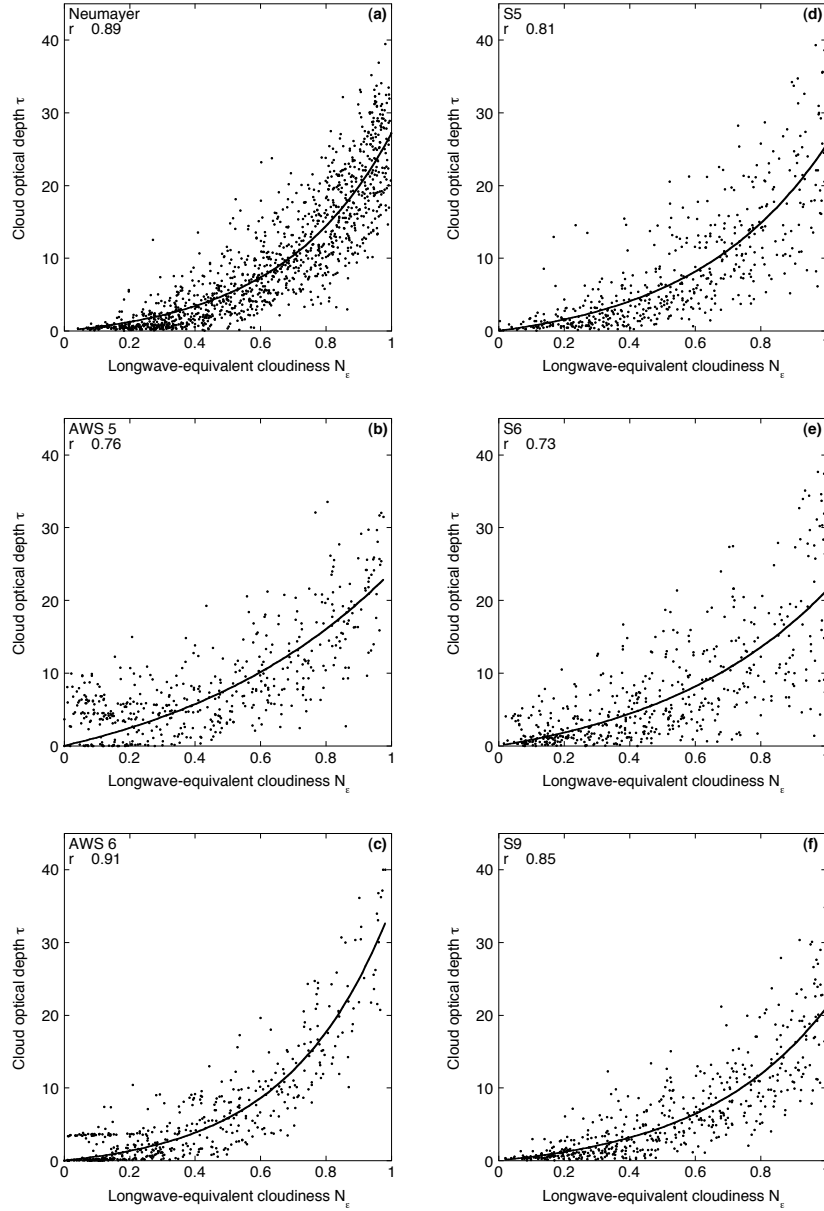


**Figure 5.4:** Longwave-equivalent cloudiness  $N_\epsilon$  against cloud optical thickness  $\tau$  for daily averages of (a) Neumayer (1995-2004), (b) AWS 5 (1998-2001), (c) AWS 6 (1998-2001), (d) S5 (2003-2007), (e) S6 (2003-2007) and (f) S9 (2003-2007). Least-squares regressions, using only days for which average  $\theta_0 < 80^\circ$ , are shown as the solid curves. The functional form of the fits is given in equation 5.3. The correlation coefficient  $r$  for each fit with the data is given in the upper-left corner of each panel, as well as in table 5.2.

**Table 5.2:** Coefficients used in Equation 5.2 to relate cloud optical thickness  $\tau$  to longwave-equivalent cloudiness  $N_\varepsilon$ . Correlation coefficient  $r$  is given in the rightmost column.

Station	$c_1$	$c_2$	$r$
Neumayer	1.53	2.93	0.89
AWS 5	7.16	1.47	0.76
AWS 6	1.46	3.21	0.91
S5	2.48	2.42	0.81
S6	4.13	1.81	0.73
S9	1.77	2.55	0.85

Linearly interpolating between these limits yields a value for  $N_\varepsilon$  between 0 and 1. From the hourly values, daily averages are calculated, which are used in a regression with  $\tau$  in section 5.3.

It should be stressed that the longwave-equivalent cloudiness ( $N_\varepsilon$ ) is not a cloud cover or cloudiness in the usual meteorological sense ( $N$ ), expressed in eights (octas) or tenths, which is based on visual observation. Instead, it is closely tied to sky emissivity and thus to the net longwave cloud forcing.

## 5.3 Results

In this section, we will apply the methods from the previous section to the AWS data sets described before. We will show that there is a correlation between  $N_\varepsilon$  and  $\tau$ , which allows for the calculation of cloud optical thickness throughout the year for all locations. Uncertainties in this procedure will be discussed.

### 5.3.1 Correlating $N_\varepsilon$ and $\tau$

In an independent way, both the longwave and the shortwave radiation balances yield objective measures for cloud cover. These can be expected to correlate, since a low value for  $\tau$  should imply a low value for  $N_\varepsilon$ , and a high  $\tau$  should coincide with a high  $N_\varepsilon$  as well. Figures 5.4(a)–(f) show scatter plots of  $\tau$  against  $N_\varepsilon$  at all locations, for all daily-averaged values of  $\theta_0 < 80^\circ$ . Least-squares regressions of the form

$$\tau = c_1(e^{c_2 N_\varepsilon} - 1) \quad (5.3)$$

show a correlation coefficient  $r$  between 0.73 and 0.91 (shown in the upper left corners of figures 5.4(a)–(f) as well as in Table 5.3). Values of  $c_1$  and  $c_2$  are also given in Table 5.2.

Although there is no clear physical argument, the form of equation (5.3) is chosen as it intersects the origin, is monotonically increasing and uses a minimum of fit coefficients while still exhibiting the exponential behaviour seen in the observations.

The correlation is second-highest for Neumayer, the station with the longest data series and the highest quality of measurements. Furthermore, the correlation is on average lower for the Greenland stations than for the Antarctic stations, since shortwave radiation measurements over melting surfaces inherently pose more problems with sensor tilt, thus impacting the retrieval of  $\tau$ . We will expand on this below in section 5.3.3.

The good correlations between  $N_e$  and  $\tau$  provide a means to calculate optical properties of clouds even in absence of solar radiation (at night or in winter), as we will show further in this section. A year-round record of cloud characteristics is an application that may be useful in assessing the wintertime performance of numerical weather prediction models over ice sheets using AWS data.

### 5.3.2 Cloud climatology from observations

Cumulative probability distributions of summertime daily values of  $\tau$  in Greenland and Antarctica are shown in figures 5.5(a)–(b). Only data for which daily-averaged  $\theta_0 < 80^\circ$  are used. In Greenland (figure 5.5(b)), differences between the stations are small, since they are in relatively close proximity to each other (the distance between S5 and S9 is only 82 m). At S5,  $\tau > 10$  for 33% of the time, whereas at S6 and S9, this is 25 and 24%, respectively. The occurrence of very thick clouds  $\tau > 20$  is lowest at S9 (< 6%). The explanation for the landward decrease in  $\tau$  is that, at higher altitudes, the amount of precipitable water decreases, thereby making clouds optically thinner.

In Antarctica, differences are larger, partly due to the larger distances between the stations. AWS 6 stands out as by far the sunniest station, with the most clear-sky occurrence. Clouds at AWS 6 are also thinner than at AWS 5 and Neumayer. At Neumayer, thick clouds occur most frequently. Again, a smaller precipitable water amount with increasing altitude can explain the thinning of clouds towards the interior.

Using the regression curves shown in figures 5.4(a)–(f), we calculated monthly averages for  $\tau$  throughout the year for all locations (figure 5.6). The spread around the fits in figures 5.4(a)–(f) leads to an uncertainty in the retrieval of  $\tau$  from  $N_e$ . Assuming that the residuals of each fit are normally distributed around the fit, the standard deviation of each daily value was used to calculate 95% confidence intervals ( $2\sigma$ ) of the monthly means in figure 5.6. In figure 5.6, the confidence intervals are plotted as error bars for AWS 6 and S5. At Neumayer (long data series), AWS 6 and S9 (good fits), the 95% confidence intervals are smallest (0.47, 0.59 and 0.64 resp.). Figure 5.6(b) resembles figure 10 in *Van den Broeke et al.* [2008a], and is shown here to update the values from that paper, originating from slightly different fit functions.

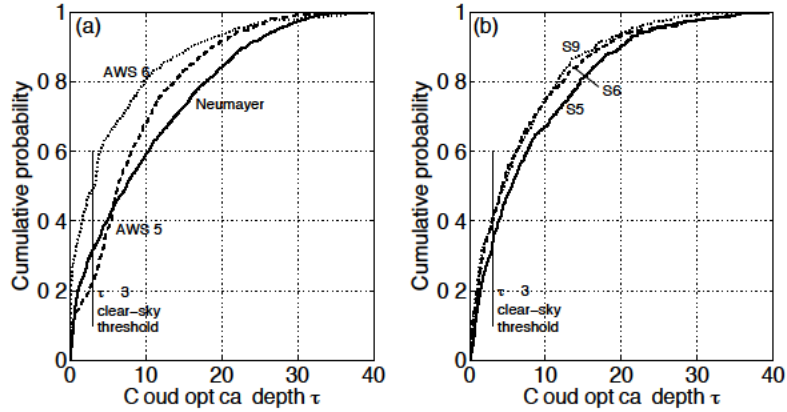


**Figure 5.5:** Cumulative probability distributions of daily-averaged cloud optical thickness  $\tau$  for all data where  $\theta_0 > 80^\circ$  for (a) all Antarctic stations; (b) all Greenland stations.

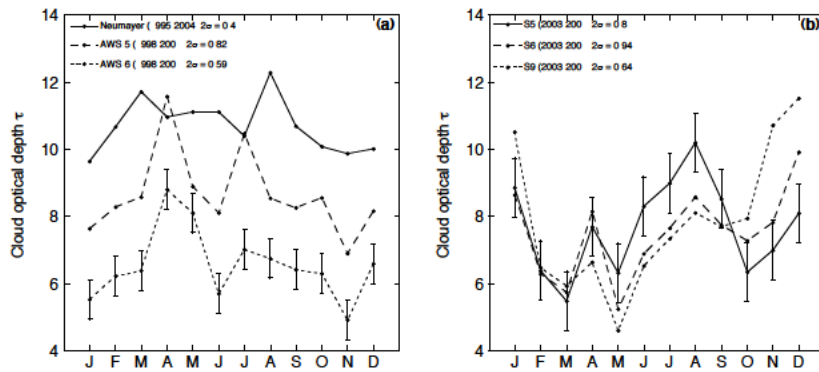


**Figure 5.6:** Monthly averages of  $\tau$  throughout the year for the entire data period, obtained from a regression with  $N_e$ ; for (a) Antarctica, and (b) Greenland. The reported  $2\sigma$  values are derived from the RMSE values of the fits in Fig. 5.4a-f, and represent the 95% confidence interval for the monthly averages. Interannual variability is not shown but discussed in the text.

**Table 5.3:** Interannual variability of  $\tau$  at Neumayer, for 1995-2004 (10 years) per month, expressed as a standard deviation from the mean of each month.

Month	$\sigma$	Month	$\sigma$
January	2.9	July	2.8
February	2.4	August	2.6
March	2.6	September	2.0
April	1.7	October	2.8
May	1.6	November	2.6
June	2.5	December	2.4

Comparison with  $\tau$  retrievals by *Ricchiazzi et al.* [1995] over Palmer Station, Antarctica, reveals that the cumulative probability function of  $\tau$  at Palmer Station is very similar to those of Neumayer and AWS 5. Since these stations are all in coastal regions, the retrieved values of  $\tau$  seem reasonable. The range of  $\tau$ -values at the Antarctic coast contrasts strongly with values reported over the Antarctic interior at South Pole [*Mahesh et al.*, 2001], but the cloud climatology over the interior is very different, with fewer and thinner clouds, and a much smaller water vapour column.

At the locations in Greenland, an increase in  $\tau$  is apparent in the summer, between May and August [*Van den Broeke et al.*, 2008a]. This feature appears robust and concurrent at all locations. The same has been observed at Summit, Greenland [*Hoch*, 2005]. It is likely that the increased water vapour budget in the atmosphere increases the average cloud cover, and therewith the monthly average  $\tau$ . It means that the impact of lower albedos on the net short-wave radiation is reduced by thicker overlying clouds. Monthly averages of cloud fraction at the nearby locations DYE 2 and DYE 3 clearly show the same pattern of an increased cloud cover throughout summer [*Griggs and Bamber*, 2008].

At the Antarctic stations,  $\tau$  also increases at all stations in the summer months (Nov–Mar), although this finding is less robust than over Greenland as it is not observed consistently for every year.

The interannual variability of  $\tau$  is high at all stations, but the AWS data records are too short to present meaningful statistics. The increase of  $\tau$  in Greenland in the summer months is, however, a yearly recurrent feature. To give insight on the magnitude of the interannual variability, we present standard deviations from the mean of the detrended 10-year Neumayer data set in Table 5.3. It ranges from 1.6 (March) to 2.7 (October), and doesn't show a clear pattern.

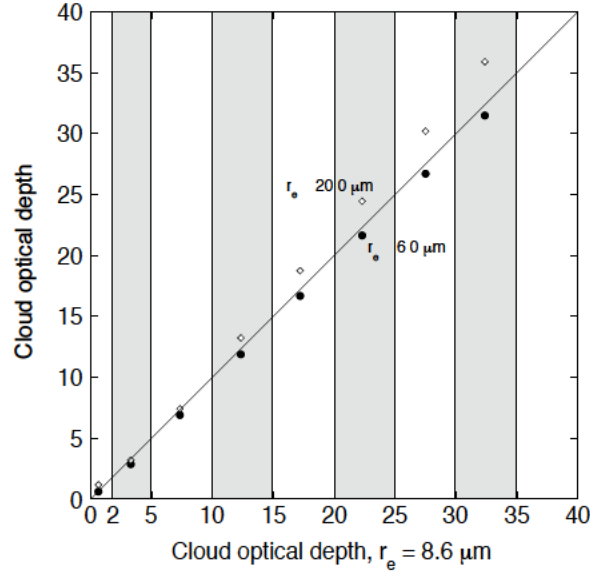


**Figure 5.7:** Uncertainty in retrieved  $\tau$  at S5 due to assuming a constant droplet size distribution (with effective droplet radius  $r_e$ ) in the parameterization of  $\tau$  by Fitzpatrick *et al.* [2004]. The average  $\tau$  is plotted for each bin of 5 for the  $r_e = 6.0 \mu\text{m}$  (black dots) and  $20.0 \mu\text{m}$  (open diamonds) distributions, against the default  $r_e = 8.6 \mu\text{m}$  distribution. The 0-5 bin has been separated into a 0-2 and a 2-5 bin.

### 5.3.3 Uncertainties

In the retrieval of  $\tau$  using equation 5.2, the main sources of error are (a) the measurement of incoming solar radiation  $SW_{\downarrow}$ , as it influences both  $\alpha$  and  $trc$ ; (b) the calculation of  $SW_{\downarrow,cs}$ , which influences  $trc$ ; and (c) the use of a constant cloud droplet size and distribution in the method by Fitzpatrick *et al.* [2004] for the retrieval of  $\tau$ . Below, we will discuss each of these sources of uncertainty.

The main errors in  $SW_{\downarrow}$  are due to sensor tilt, rime formation, and the cosine response of the pyranometer. The correction that we applied for sensor tilt of the AWSs is based on a constant tilt angle that is measured annually upon each maintenance visit. Since the Greenland AWSs are free-standing structures that move downward with the melting surface, the tilt angle may not be constant in time. Tilt angle will be most variable at S5 and S6 where summer melt can amount up to several meters. With few or very thin clouds, tilt may over- or underestimate  $trc$  and  $\alpha$ , thus limiting the accuracy of the retrieval of  $\tau$ . In overcast situations, the error in  $trc$  and  $\alpha$  is much smaller, since errors in  $SW_{\downarrow}$  are very small for diffuse incident radiation.

**Table 5.4:** Influence of uncertainty in  $SW_{\downarrow,cs}$  ( $W m^{-2}$ ) on retrieved  $trc$  and  $\tau$ , from daily averages at Neumayer. The ‘reference’ column contains values from the the fit of  $SW_{\downarrow,cs}$  that was considered best.

Quantity	Reference	$SW_{\downarrow,cs} - 2.0\%$		$SW_{\downarrow,cs} + 2.0\%$	
		abs	rel	abs	rel
$SW_{\downarrow,cs}$	355.60	348.49	-2.0%	362.71	+2.0%
$trc$	0.802	0.818	+1.9%	0.786	-2.0%
$\tau$	9.22	8.55	-7.3%	9.91	+7.5%
$\tau < 5$	1.81	1.50	-16.7%	2.15	+18.8%
$5 < \tau < 15$	9.63	8.80	-8.6%	10.50	+9.0%
$\tau > 15$	20.25	19.22	-5.1%	21.26	+5.0%

The spread in  $\tau$  for small  $N_e$  in Greenland (figures 5.4(d)–(f)) can partly be explained in this way. At Neumayer, where instruments tilt is checked daily, the spread of  $\tau$  for low  $N_e$  is much smaller. Furthermore, the K&Z CM11 pyranometers at Neumayer have a better cosine response than the K&Z CM3 pyranometers of the AWSs, also attributing to smaller spread for low  $N_e$ . The effect of an error in  $trc$  on the error in  $\tau$  is illustrated in the paper by *Fitzpatrick et al.* [2004] (their figure 6). For  $\tau > 20$ , an albedo of 0.80 and  $\theta_0 = 78^\circ$ , a 2% error in  $trc$  typically leads to a 5% error in retrieved  $\tau$ . This error decreases for lower  $\tau$ .

Another main source of error,  $SW_{\downarrow,cs}$ , leads to an uncertainty in the values for  $trc$ . As explained above,  $SW_{\downarrow,cs}$  is determined by fitting an envelope around the graph of daily averages of  $SW_{\downarrow}$  (figure 5.2). The quality of this fit is determined by eye and can introduce errors in the retrieved  $\tau$ . To quantify this effect, we varied annually averaged  $SW_{\downarrow,cs}$  at Neumayer by +2 and -2% with respect to a reference value, which is comparable to the accuracy of the fit by eye. The results of this error sensitivity analysis are given in table 5.4. Values of  $trc$  change by only -2.0% and +1.9%, but annually-averaged  $\tau$  changes by -7.3% and +7.5%, respectively (-0.67 and +0.69 in absolute values). The relative effect is greatest for small values of  $\tau$  (-16.7% and +18.8%), whereas the absolute effect is greatest for large values of  $\tau$  (-1.03 and +1.01). At AWS 5 and 6, there is an offset of  $\tau$  visible at low  $N_e$  (figures 5.4(b)–(c)). This also affects the cumulative probability distributions in figure 5.5. We have tried to resolve this but found no plausible explanation with the available information.

The third source of uncertainty in the retrieval of  $\tau$  comes from the assumption in the method by *Fitzpatrick et al.* [2004] that the cloud droplet distribution of all clouds is the same. As explained above, *Fitzpatrick et al.* [2004] show that a good parameterization of  $\tau$  can be obtained using several cloud droplet distributions, but each parameterization will lead to slightly different values for  $\tau$ . In figure 5.7, we show these differences for station S5. The values for  $\tau$  that we obtained with the default cloud droplet distribution, with an effective cloud droplet radius  $r_e = 8.6\mu m$ , are binned in intervals of  $\Delta\tau_{8,6} = 5$ . The average  $\tau_{8,6}$  in each bin is then

compared to the average  $\tau_{6.0}$  and  $\tau_{20.0}$ . For large  $\tau_{8.6}$ , values of  $\tau_{20.0}$  deviate most from  $\tau_{8.6}$ , the average  $\tau_{20.0}$  being 3.5 larger (11%). The largest relative difference is in the clear-sky bin ( $0 < \tau_{8.6} < 2$ ), where  $\bar{\tau}_{8.6} = 0.64$  and  $\bar{\tau}_{20.0} = 1.17$ , meaning that the amount of clear-sky data becomes somewhat dependent on the choice of the parameterization for  $\tau$ .

Errors in  $N_\varepsilon$  are assumed to be small, since both the K&Z CG3 pyrgeometers of the AWSs and the Eppley PIRs at Neumayer are reliable instruments with continuous data records.

## 5.4 Applications

The inferred values of  $\tau$  can be used to distinguish between clear and cloudy days. From the daily averages of  $\tau$ , we have extracted a subset of clear days ( $\tau < 3$ ) and a subset of fully overcast days ( $\tau > 14$ ). To test the clear-sky threshold of  $\tau = 3$ , we applied the *Marty and Philipona* [2000] method to construct alternative clear-sky data sets, and found out that the average  $\tau$  of those data sets was 2.3, suggesting that a maximum value of 3 is a reasonably strict criterium compared to existing methods. As three applications of the method presented above, we discuss the influence of clouds on the radiation budget (Application I), the relation between cloud cover and broadband albedo (Application II) at the six AWS locations, and we demonstrate the possibility to detect trends in  $\tau$  in longer data series (Application III).

### 5.4.1 Application I: Clouds and multiple reflections

Clouds shield the surface from solar radiation by reflecting it back to space, and by absorption. Over highly reflective surfaces however, a cloud will compensate a part of this loss of solar radiation through the effect of multiple reflection between the surface and the cloud base. As an application, the magnitude of this effect can be calculated simply by inserting  $\alpha = 0$  into equation 5.2, so that multiple reflections by clouds are ignored. The incoming radiation with and without multiple reflection is plotted for station S6 in figure 5.8 as an example. For the cloudy data sets, the effect enhances  $SW_\downarrow$  by more than a factor of 2 in May and decreases to a factor of 1.5 from July onwards when the ice surface appears.

The enhancement is thus strongest at locations with a high-albedo and frequent cloud cover. Averaged over all summer days, multiple reflection enhances the monthly incoming flux strongest at Neumayer (29%). The effect is weakest at S5 (18%) in Greenland due to lower surface albedos of ice in summer. At S6, shown in figure 5.8, the incoming flux is enhanced by 25%. The effect of a particular cloud on  $SW_{net}$  is thus strongly reduced as it moves from a low-albedo surface (like the ocean) over a high-albedo snow or ice surface, even if the cloud does not change physically.

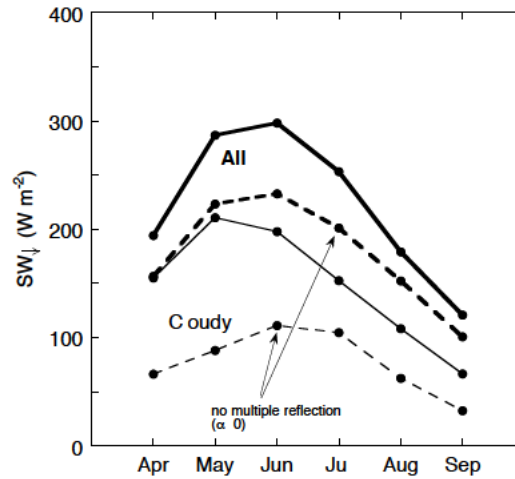


**Figure 5.8:** Incoming shortwave radiation at S6 (monthly averages) for cloudy days (thin lines) and all days (thick lines). Dashed lines are without multiple reflections between surface and cloud base.

#### 5.4.2 Application II: Clouds and albedo

Clouds alter the broadband albedo of a snow surface mainly by filtering out radiation at near-IR wavelengths ( $> 800$  nm) more effectively than radiation in the visible region: the spectral composition of the radiation arriving at the surface changes. As the spectral albedo for visible wavelengths is higher than for near-IR wavelengths, the spectrally-integrated albedo increases. This ‘spectral effect’ is amplified by multiple reflections between the surface and the cloud base: after each reflection, the radiation gets more depleted in near-IR wavelengths [Wiscombe and Warren, 1980].

Daily-averaged albedos are plotted for all stations in figures 5.9(a)–(f). At all stations, the clear-sky albedo,  $\alpha_{cs}$ , varies throughout the year. In Greenland, the most important cause for these variations is snow melt and the subsequent appearance of the ice surface. But even in Antarctica, there is significant albedo variation, primarily due to snow metamorphism (as we saw in chapter 4), but also caused by the seasonal cycle in  $\theta_0$ . At all Antarctic stations (figures 5.9(a)–(c)), the albedo under cloudy sky,  $\alpha_{cl}$ , is larger than  $\alpha_{cs}$  throughout the summer, due to the dominating spectral effect. From the Greenland data, a more complicated picture emerges: at S9, situated at the equilibrium line altitude,  $\alpha_{cl}$  decreases gradually throughout the season until late August, when the superimposed ice horizon surfaces for one to a few weeks. In 2007, the winter snow cover already disappeared in June, seen as a cluster of

**Table 5.5:** Characteristics of the narrowband sensors used in figure 5.10 to illustrate spectral albedo effects under clear and cloudy sky for snow and ice surfaces. MODIS = Moderate Resolution Imaging Spectroradiometer, MISR = Multiangle Imaging SpectroRadiometer, AVHRR = Advanced Very High Resolution Radiometer.

Instrument	Band	Wavelength [nm]		
		min	max	centr
AVHRR	1	574	704	639
MISR	3	663	679	671
MODIS	2	838	875	857

low-albedo data in the box in figure 5.9(f). Generally, clouds enhance broadband albedo throughout the summer at S9. The same is true for the high-albedo spring snow surface at S6, until the snow has melted away and the ice appears. From then on,  $\alpha_{cs}$  and  $\alpha_{cl}$  are no longer discernible (figures 5.9(d)–(e)). At S5, there is almost no snow accumulation, and before the 1<sup>st</sup> of June, there is intermittent snow cover. A consistent feature is that the distinction between  $\alpha_{cs}$  and  $\alpha_{cl}$  disappears when snow cover has completely melted away (which is recorded by a sonic height ranger for measuring snow depth). At S5, this was consistently around the 1<sup>st</sup> of June for the considered period, whereas at S6, this happens somewhere between mid-June and the beginning of July.

Three narrowband pyranometers [Knap *et al.*, 1999; Greuell and Oerlemans, 2004] that operated at S6 in 2004–05 are used to explain why  $\alpha_{cs}$  and  $\alpha_{cl}$  become indiscernible over ice. Two pairs of days were selected: 15 (cloudy) and 17 (clear) May 2005 both had a snow cover at S6, while at the 2<sup>nd</sup> (clear) and 5<sup>th</sup> (cloudy) of August, ice was at the surface. Narrowband albedo from these pyranometers are presented in figure 5.10 for these days.

For the snow cover (15 and 17 May), spectral albedo under clouds is only a bit lower than under a clear-sky, in line with the ‘diffuse radiation effect’ [Wiscombe and Warren, 1980]. The narrowband measurements agree well with theoretical spectral albedo curves obtained by applying the Wiscombe and Warren [1980] model with  $r = 800 \mu\text{m}$ . The directly measured broadband albedo under clouds (0.86) is much higher than for the clear sky (0.73), in accordance with the ‘spectral effect’ as discussed above.

For the ice surface (2 and 5 August), clear-sky narrowband albedos are about 0.10 higher for visible shortwave radiation than albedo under a cloudy sky. This difference is possibly due to different surface conditions. This time however, the directly measured clear-sky broadband albedo (0.47) is only slightly higher than the albedo under clouds (0.44). The reason is that spectral albedo for ice is only 0.4–0.6 in the visible region, so that multiple reflection between surface and cloud is much weaker than for snow. The enrichment of visible radiation that is important for the ‘spectral effect’ ceases to enhance broadband albedo. Even when the spectral albedos are quite different in the visible, the broadband albedo changes hardly. For

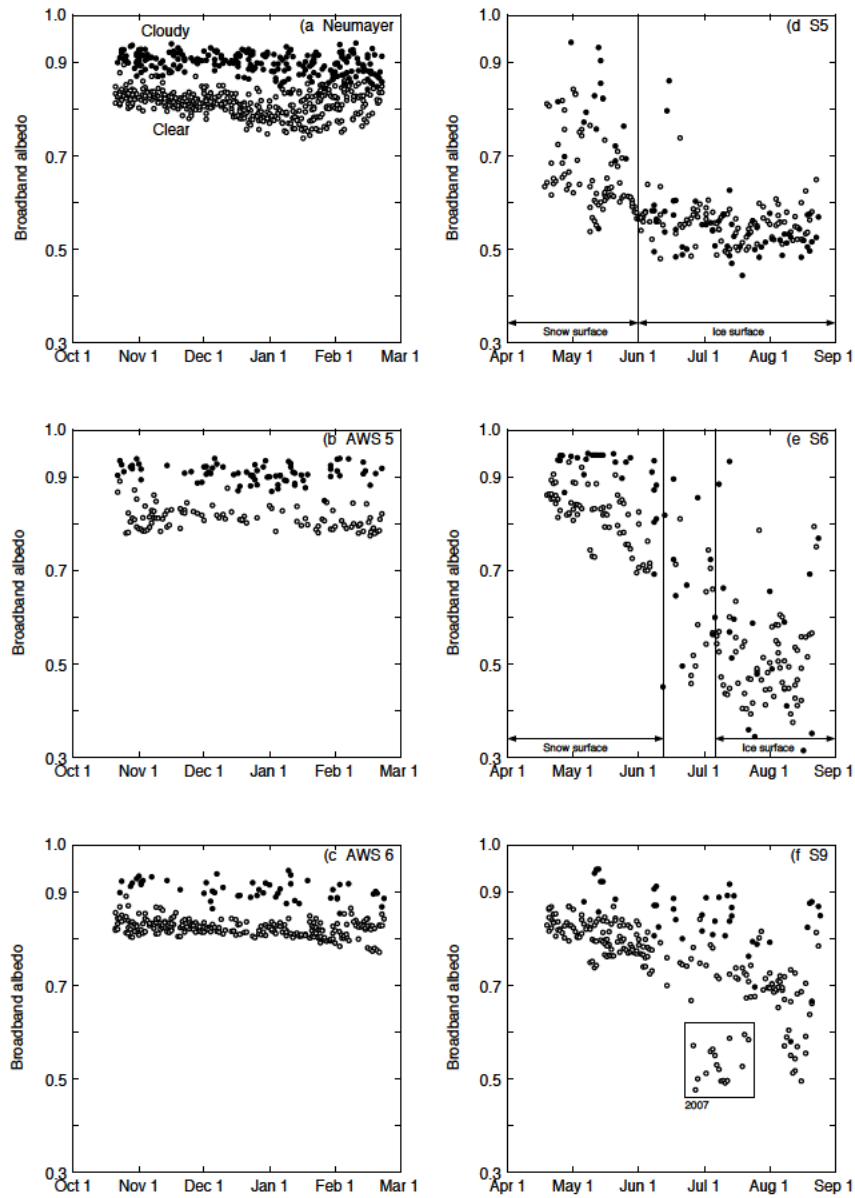


**Figure 5.9:** Daily averages of broadband albedo for clear (open dots) and cloudy (solid dots) days at (a) Neumayer, (b) AWS 5, (c) AWS 6, (d) S5, (e) S6 and (f) S9.

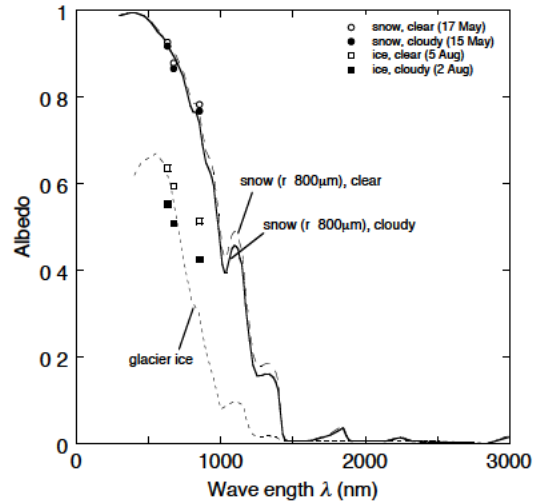


**Figure 5.10:** Narrowband albedos at S6 on a clear (open symbols) and cloudy day (closed symbols) for a snow (circles) and an ice (squares) surface. Narrowband pyranometer central wavelengths are listed in Table 5.5. The solid and the adjacent dashed lines are theoretical snow albedos for a grain size of  $800\ \mu\text{m}$  (calculated using Mie scattering), and the separate dashed line is for glacier ice albedo taken from Zeng *et al.* [1984], extended beyond  $1150\ \text{nm}$  with calculations from very large snow grains ( $> 3\ \text{mm}$ ).

reference, we plotted the albedo curve for glacier ice by Zeng *et al.* [1984] in figure 5.10.

The decrease in visible enrichment also explains observations by Brock *et al.* [2000] at Glacier Haut d’Arolla, Switzerland, and those by Jonsell *et al.* [2003] at Storglaciären, Sweden. Brock *et al.* [2000] found no correlation between ice albedo and  $\theta_0$  or cloud cover. Jonsell *et al.* [2003] also observed only a very weak albedo change under cloudy skies.

### 5.4.3 Application III: Trends at Neumayer

Another useful application of the method is to detect long-term trends in cloud optical thickness from longer data series. The data series at Neumayer are sufficiently long for this purpose. In figure 5.11, we show time series of  $\tau$  at Neumayer for the period 1995–2004. There is a significant trend of  $-0.4\ \text{y}^{-1}$ , indicating that the radiation balance of the snowpack is gradually changing. This is in line with the observed trend in increasing incoming solar radiation of  $+1.24\ \text{W m}^{-2}$  at Neumayer since the 1990s [Wild *et al.*, 2005]. The causes of this increase in solar radiation (and thus, a decrease in  $\tau$ ) are currently under debate, but it is beyond the

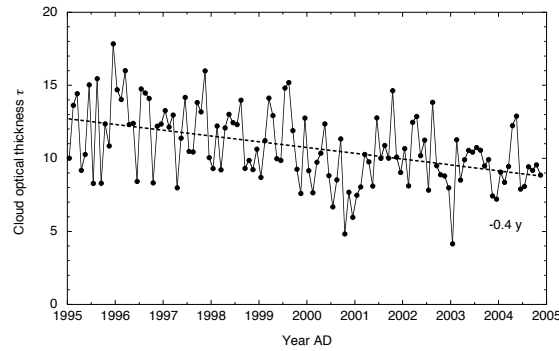


**Figure 5.11:** Monthly values of retrieved cloud optical thickness  $\tau$  between 1995 and 2004, at Neumayer, Antarctica. The dashed line shows the downward trend in  $\tau$  of  $0.4 \text{ y}^{-1}$ .

scope of this chapter to discuss this any further. However, we do show that such trends in the cloud climate of snow- and ice-covered regions can be determined.

## 5.5 Conclusions

In this chapter, we have critically reviewed a method to obtain quantitative information on clouds from radiation measurements made with AWSs over snow and ice surfaces [Van den Broeke *et al.*, 2008a; Giesen *et al.*, 2009]. The longwave radiation balance yields a ‘longwave-equivalent cloudiness’,  $N_e$ , which is closely tied to the emissivity of the sky. For clear skies,  $N_e = 0$  and for overcast skies,  $N_e = 1$ . The shortwave radiation balance can be used to infer the cloud optical thickness,  $\tau$ , using the parameterization by Fitzpatrick *et al.* [2004].

Using data sets from six different climatic regions in Greenland and Antarctica, we have shown that the cloud optical thickness  $\tau$  correlates well with  $N_e$ , which is determined entirely independently from the longwave radiation balance. This correlation for each location can be used to infer shortwave cloud properties even in the absence of solar radiation, an application which may be useful in the validation of weather and climate models over ice sheets during wintertime.

A correct retrieval of  $\tau$  is most sensitive to errors in the incoming shortwave radiation, i.e. when the pyranometer is covered with rime, when it tilts, or when  $\theta_0$  is high. This is true especially for thin cloud cover. The retrieval of  $\tau$  is also dependent on the prescribed value for clear-sky incoming shortwave radiation  $SW_{\downarrow,cs}$ . An error of 2% in  $SW_{\downarrow,cs}$  leads to an error in annually-averaged  $\tau$  of about 7–8%.

We have calculated annual records of cloud optical thickness for each of the six locations

considered in this study. It shows that both in Greenland and Antarctica, cloud become thinner and clear-sky conditions more frequent away from the coast. A smaller precipitable water column at higher altitude and with lower temperatures can explain these findings. Moreover,  $\tau$  increases throughout the summer both in Antarctica and Greenland, which reduces the effect that low ice albedos have on the shortwave radiation balance.

Three applications were presented to demonstrate the versatility of the method. Using  $\tau$  as a selection criterion, it is possible to distinguish between clear and cloudy days, and assess the influence of clouds on e.g. the radiation budget and snow and ice albedo. Although clouds do attenuate shortwave radiation due to reflection and absorption, the incoming solar radiation at the surface is partly compensated for this loss by multiple reflections between the surface and the cloud base. Averaged over all summer days, multiple reflection enhances  $SW_{\downarrow}$  by 18% (S5) to 29% (Neumayer) relative to the situation without multiple reflections. Furthermore, we have shown that over snow surfaces, albedo under cloudy sky is always higher than the clear-sky albedo, due to the ‘spectral effect’ of clouds. Over ice surfaces, this difference ceases, since the visible albedo of ice is so low that the ‘spectral effect’ that dominates over snow is very weak over ice. As a third application, we detected a clear trend of decreasing  $\tau$  from the 1995–2004 Neumayer data series, consistent with a reported increase in incoming solar radiation. The method is thus suitable to detect long-term trends in the optical properties of clouds over snow and ice.

The use of the methods presented in this chapter is not restricted to glaciers and ice sheets. It can be applied to any snow or ice surface, as long as radiation measurements are reasonably reliable. This opens up possibilities to explore data records from seasonally snow-covered regions in the Arctic. Although not tested here, the method could even be applicable to radiation data over any surface. For that, the coefficients derived by *Fitzpatrick et al.* [2004] should be rederived using spectral albedos typical for that surface.

## The energy budget of the snowpack at Summit, Greenland

### Summary

Measurements of the summer surface energy balance at Summit, Greenland, are presented (June 8 – July 20, 2007). These measurements serve as input to an energy balance model that searches for a surface temperature for which closure of all energy terms is achieved. A good agreement between observed and modelled surface temperatures was found, with an average difference of  $0.45^{\circ}\text{C}$  and an RMSE of  $0.85^{\circ}\text{C}$ . It turns out that penetration of shortwave radiation into the snowpack plays a small but important role in correctly simulating snow temperatures. After 42 days, snow temperatures in the first meter are  $3.6\text{--}4.0^{\circ}\text{C}$  higher compared to a model simulation without radiation penetration. Sensitivity experiments show that these results cannot be reproduced by tuning the heat conduction process alone, by varying snow density or snow diffusivity. We compared the two-stream radiation penetration calculations with a sophisticated radiative transfer model and discuss the differences. The average diurnal cycle shows that net shortwave radiation is the largest energy source ( $+61\text{ W m}^{-2}$  on average), net longwave radiation the largest energy sink ( $-42\text{ W m}^{-2}$ ). On average, subsurface heat flux, sensible and latent heat fluxes are the remaining, small heat sinks ( $-5$ ,  $-5$  and  $-7\text{ W m}^{-2}$ , respectively), although these are more important on a subdaily timescale.

---

This chapter is published as Kuipers Munneke, P., M. R. van den Broeke, C. H. Reijmer, M. M. Helsen, W. Boot, M. Schneebeli and K. Steffen (2009), The role of radiation penetration in the energy budget of the snowpack at Summit, Greenland, *The Cryosphere*, **3**, 155-165.

## 6.1 Introduction

The energy balance at the surface of a snowpack is given by

$$SW_{net} + LW_{net} + H_{sen} + H_{lat} + \tilde{G}_s = M \quad (6.1)$$

(all terms in  $[\text{W m}^{-2}]$ ) where the net shortwave radiation,  $SW_{net}$ , is the sum of global shortwave radiation,  $SW_{\downarrow}$ , and reflected radiation,  $SW_{\uparrow}$ ; net longwave radiation,  $LW_{net}$ , is the sum of downwelling longwave radiation,  $LW_{\downarrow}$ , and upwelling longwave radiation,  $LW_{\uparrow}$ ;  $H_{sen}$  is the turbulent sensible heat flux,  $H_{lat}$  is turbulent latent heat flux,  $\tilde{G}_s$  is the subsurface heat flux at the surface, and  $M$  is the amount of melt energy.

In the absence of meltwater percolation, the temperature distribution within the snowpack is governed mainly by heat conduction, which has a diffusive nature. Close to the surface, also non-diffusive processes take place, like subsurface penetration and subsequent absorption of shortwave radiation [Colbeck, 1989b], wind pumping [Colbeck, 1989a], and latent heat transfer by subsurface water vapour transport [Albert and Shultz, 2002]. The latter two processes are known to play a role at high wind speeds. Earlier studies suggested that the subsurface heat production by penetration of shortwave radiation could be significant [Schlatter, 1972], leading to a ‘solid-state greenhouse’ [Matson and Brown, 1989], in which shortwave radiation is absorbed below the surface while longwave radiation is emitted at the surface. Later, it was shown that these studies overestimated this effect as they did not take into account the large variation of the extinction coefficient of snow with wavelength [Brandt and Warren, 1993]. Hence, the latter authors concluded that subsurface heating in Antarctica must be very small. The importance of treating subsurface radiation spectrally is underlined by experimental studies on subsurface radiation fluxes, e.g. by Meirold-Mautner and Lehning [2004] at Summit. Although it was shown that radiation penetration was overestimated previously, Liston and Winther [2005] suggested that no less than 20% of the snow-covered area of Antarctica experiences subsurface melt. Since most of this meltwater refreezes locally, the effect on the mass balance of Antarctica is supposed to be small.

Although the effect was shown to be smaller than presumed before, it potentially affects the subsurface temperature distribution, since energy is transferred below the surface more efficiently than by conduction of heat from the surface layer alone. For ice, it was already demonstrated that radiation penetration plausibly explains observed vertical temperature distributions and vertical melt extent at several sites in the ablation zone of the Greenland ice sheet [Van den Broeke et al., 2008b]. For snow, the influence of radiation penetration on the formation of depth hoar [Alley et al., 1990] and crystal growth [Colbeck, 1989b] has been studied in detail, although the latter did not use a spectral model. Absorption of radiation below the surface leads to strong snow temperature gradients just below the surface. For a correct simulation of the effect of radiation penetration on snow temperature, it is therefore important to use a sufficiently high resolution of the subsurface model [Dadic et al., 2008].

In this chapter, we present detailed and high-quality measurements of the energy budget of the snowpack during two summer months at Summit, Greenland, and show that subsurface absorption of penetrated radiation plays an important role for the temperature distribution in the snowpack. In section 6.2 and 6.3, the data and energy balance model are presented; section 6.4 discusses the results, and the paper is concluded and summarized in section 6.5.

## 6.2 Data

In this section, we present data acquired in a period of 42 days from June 8 to July 20, 2007, during the Summit Radiation Experiment (SURE 07), performed at the Greenland Environmental Observatory at Summit (72°34' N 38°28' W, 3209 m a.s.l.), on top of the Greenland ice sheet.

A single-level automatic weather station (AWS) performed ventilated measurements of air temperature  $T_a$ , air pressure  $p$ , relative humidity  $RH$ , and wind speed  $u$  at 3.85 m above the surface. The specific humidity of air,  $q$ , is calculated from these data. Below the surface, subsurface snow temperatures  $T_{sn,i}$  were measured at depths  $z_i$  using thermistor strings (0.20, 0.30, 0.50, 0.75 and 1.00 m) and thermocouples (spaced 0.02 m up to 0.10 m). AWS data were stored as 5-minute averages on a Campbell CR10X datalogger.

The radiation components of the surface energy balance were measured with a separate installation equipped with high-quality sensors for long- and shortwave radiation.  $SW_{net}$  was measured with a pair of Kipp & Zonen (K&Z) CM21 pyranometers (the upward-looking one being ventilated);  $LW_{net}$  was measured using K&Z CG4 pyrgeometers (again, the upward-looking one being ventilated). The radiation data were stored as 1-minute averages.

The upward-looking pyranometer regularly suffered from rime accretion during clear nights, which was removed manually every morning around 7:15am local time (09:15 GMT).  $SW_{\downarrow}$  data suspected to be corrupted by rime were replaced by parameterized data by linearly interpolating the albedo during the period of the data gap and using  $SW_{\uparrow}$ .

We compared the K&Z CG4  $LW_{net}$  measurements with data acquired by Eppley Precision Infrared Radiometers (PIR) at the nearby candidate-BSRN radiation station [Baseline Surface Radiation Network, *Ohmura et al.*, 1998]. It was found that the CG4  $LW_{\uparrow}$  measurements were systematically overestimated ( $3.5 \text{ W m}^{-2}$  on average, peaking at  $5\text{--}7 \text{ W m}^{-2}$  during daytime). Contrary to the BSRN measurements, the CG4 sensor measuring  $LW_{\uparrow}$  was not ventilated and its measurements were affected by window heating, i.e. heating of the sensor dome by reflected solar radiation. Since the thermal conduction between the dome and the thermopile measuring sensor housing temperature is near-perfect, the thermopile gets too warm and the calculated  $LW$ -fluxes too high. Window heating is less of a problem for the ventilated upward-facing CG4 ( $1.9 \text{ W m}^{-2}$  difference with the Eppley PIR on average), but the BSRN Eppley PIR  $LW_{\downarrow}$  measurements are preferred as they are shielded from direct solar

radiation. Comparison of the  $SW$ -fluxes with those from the BSRN site showed that our measurements have less scatter (presumably due to regular removal of accreted rime). In the remainder of this manuscript, we will therefore use the K&Z CM21  $SW$ -fluxes from our setup and the Eppley PIR  $LW$ -fluxes from the candidate-BSRN station.

The sensible heat flux was measured directly with a Campbell CSAT3 sonic anemometer at a frequency of 20 Hz, and 5-minute averages were stored on a separate Campbell CR10X datalogger. The sonic anemometer was fitted with a Campbell Chromel Constantan 75 micron thermocouple for temperature measurements.  $H_{sen,obs}$  can be deduced from the measurements of vertical wind velocity and potential temperature variations  $w'$  and  $\theta'$ , using the flux-profile relation

$$H_{sen,obs} = \rho_a c_p (\overline{w'\theta'})_{z_{son}}, \quad (6.2)$$

where  $\rho_a$  is the density of air,  $c_p$  the specific heat capacity of dry air, and  $z_{son}$  the sonic anemometer measurement height.

The latent heat flux was not measured directly, but rather computed using the bulk aerodynamic method as explained in section 6.3.

## 6.3 The energy balance model

For the calculation of the energy budget of the snowpack, the model by *Van den Broeke et al.* [2005] was used [see also *Van As et al.*, 2005a; *Giesen et al.*, 2008]. The model calculates the energy fluxes of a skin layer without heat capacity, it employs the bulk aerodynamic method for turbulent fluxes (see section 6.3.1), and it calculates the subsurface temperature profile using the one-dimensional heat-transfer equation (section 6.3.3). Using  $SW_{net}$ ,  $LW_{\downarrow}$  and the AWS measurements as input, the energy balance in equation 6.1 is solved iteratively in order to find a value for  $T_s$  for which the energy budget is closed. As we will see later, this iterative procedure makes the model very robust, and less susceptible to errors in input data: since all fluxes are interrelated, and a change in  $T_s$  has opposing effects on different fluxes, errors in the input are strongly damped. This was also demonstrated in an error analysis by *Van As et al.* [2005a]. The model has a time step of 1 minute.

### 6.3.1 Turbulent fluxes

In the energy balance model, the turbulent fluxes are calculated using

$$H_{sen} = \rho_a c_p u_* \theta_* \quad (6.3)$$

$$H_{lat} = \rho_a L_{v,s} u_* q_* \quad (6.4)$$

where  $L_{v,s}$  is latent heat of vapourization or sublimation, depending on the surface temperature  $T_s$ . The surface friction velocity  $u_*$ , and the turbulent scaling parameters for temperature  $\theta_*$  and specific humidity  $q_*$ , are computed using the bulk method – a method that exploits Monin-Obukhov similarity theory for wind, temperature and moist profiles in the surface layer, and the following assumptions at the surface: at the surface roughness length for momentum  $z_{0,u}$ , wind velocity  $u(z_{0,u}) = 0$ ; at roughness length for temperature  $z_{0,T}$ , air temperature  $T_a(z_{0,T}) = T_s$ ; and at roughness length for moisture  $z_{0,q}$ , the air is saturated:  $q(z_{0,q}) = q_{sat}(z_{0,q})$ . With the Monin-Obukhov length  $L$ ,

$$L = \frac{u_*^2}{\kappa g / \theta [\theta_* + 0.62 \theta q_*]}, \quad (6.5)$$

$u_*$ ,  $\theta_*$  and  $q_*$  can be expressed using measurements of  $u$ ,  $T_a$  and  $q$  at measurement levels  $z_u$ ,  $z_T$  and  $z_q$ :

$$u_* = \frac{\kappa u(z_u)}{\ln\left(\frac{z_u}{z_{0,u}}\right) - \Psi_m\left(\frac{z_u}{L}\right) + \Psi_m\left(\frac{z_{0,u}}{L}\right)} \quad (6.6)$$

$$\theta_* = \frac{\kappa(T_a(z_T) - T_s)}{\ln\left(\frac{z_T}{z_{0,T}}\right) - \Psi_h\left(\frac{z_T}{L}\right) + \Psi_h\left(\frac{z_{0,T}}{L}\right)} \quad (6.7)$$

$$q_* = \frac{\kappa(q(z_q) - q_{sat}(z_{0,q}))}{\ln\left(\frac{z_q}{z_{0,q}}\right) - \Psi_h\left(\frac{z_q}{L}\right) + \Psi_h\left(\frac{z_{0,q}}{L}\right)}. \quad (6.8)$$

In the above equations,  $\kappa = 0.4$  is the Von Kármán constant;  $\Psi_{m,h}$  are vertically-integrated stability correction functions taken from *Holtslag and de Bruin* [1988] for stable conditions and *Dyer* [1974] for unstable conditions (which occur regularly during daytime at Summit [Cullen and Steffen, 2001; Cullen et al., 2007]). Roughness length for momentum,  $z_{0,u}$ , is taken constant at  $3.8 \times 10^{-4}$  m, derived from sonic anemometer measurements. Values for  $z_{0,T}$  and  $z_{0,q}$  are calculated following *Andreas* [1987]. Since  $u_*$  (and  $\theta_*$  and  $q_*$ ) requires the calculation of  $L$ , which is in turn dependent on  $u_*$  (and  $\theta_*$  and  $q_*$ ), the turbulent fluxes are solved iteratively.

### 6.3.2 Radiation penetration

The model includes a module to calculate subsurface radiation penetration of shortwave radiation following the method presented by [Brandt and Warren, 1993]. The model is identical to the one used in *Van den Broeke et al.* [2008b]. This module employs the two-stream approach from *Schlatter* [1972], giving analytical functions for attenuation of shortwave radiation *per wavelength*. The module calculates radiation in 118 wavelength bands covering the solar spectrum, and uses Mie scattering coefficients derived from *Warren* [1984], updated with values from *Warren et al.* [2006] for the UV and visible wavelength range. The two-

stream analytical functions require a constant snow density  $\rho_{sn,rp}$  and effective snow grain radius  $r_e$ . The grid spacing for the radiation penetration calculations is 0.001 m. Results on this grid are interpolated onto the 0.01 m grid used for the subsurface calculations (see section 6.3.3). Increasing the grid resolution any further did not affect the results.

Energy released by radiation penetration in the snowpack is added to the appropriate subsurface model layers, and the total amount of penetrated radiation  $Q$  is subtracted from the surface skin layer. Equation 6.1, which is valid for the surface layer, formally becomes

$$SW_{net} + LW_{net} + H_{sen} + H_{lat} + G_s - Q = M \quad (6.9)$$

For an infinitesimally thin surface layer,  $SW_{net} = Q$  and these terms would cancel for the surface layer. Because of the discrete nature of the model numerics however, the surface layer energy budget retains the shape of equation 6.9.

The hypothesized effect of incorporating radiation penetration is that energy is released below the surface, enabling a more rapid warming of the snowpack.

### 6.3.3 Subsurface flux

To obtain the subsurface heat flux  $G$ , a subsurface module is included in the model, which calculates the one-dimensional heat-transfer equation on a 0.01 m grid up to a depth of 20 m, beyond which  $G$  is assumed to be zero. The model results are insensitive to grid size smaller than 0.01 m. It was already pointed out by *Dadic et al.* [2008] that modelling of subsurface processes should be done at a sufficiently high resolution, as the temperature gradient attains large values. The snow density profile,  $\rho_{sn}(z)$  is prescribed using measurements from several snow pits, and thus decoupled from the constant density required for the radiation penetration calculations. In each snow pit, we collected one pair of density profiles, spaced about 0.30 m apart to account for horizontal variations and to reduce the measurement error. In total, 7 pairs of density profiles have been collected with an approximate resolution of 0.02 m up to a depth of 1.0 m, which were interpolated in time to account for temporal variations, and interpolated onto the 0.01 m subsurface grid. Below 1.0 m, density is taken constant at 400 kg m<sup>-3</sup>.

Thermal conductivity of snow,  $k_{sn}$ , is prescribed as a function of  $\rho_{sn}(z)$  (in kg m<sup>-3</sup>), following *Anderson* [1976]:

$$k_{sn} = 0.021 + 2.5 \left( \frac{\rho_{sn}}{1000} \right)^2 \quad (6.10)$$

The specific heat capacity of ice,  $c_{p,ice}$ , is a function of  $T_{sn}(z)$ . The vertical snow temperature profile was initialized using measurements typical for June at Summit [*Hoch*, 2005], scaled in the uppermost meter with our own measurements of  $T_{sn}$ .

The subsurface heat flux at the surface is denoted as  $G_s$ , and calculated using the model temperature gradient at the surface. To compare our energy budget calculations with previous

studies [Cullen and Steffen, 2001; Hoch, 2005] that did not explicitly distinguish between subsurface heat fluxes by diffusion and subsurface radiation penetration, we will present their combined effects as  $\tilde{G}_s$  using model snow temperatures [Hoch, 2005]:

$$\tilde{G}_s = - \sum_{j=1}^{n-1} \frac{\Delta T_{sn}(z_j)/\Delta t + \Delta T_{sn}(z_{j+1})/\Delta t}{2} \cdot c_{p,ice,j} \cdot \rho_{sn,j} \cdot (z_j - z_{j+1}) \quad (6.11)$$

The temperatures at the subsurface grid are used, and at  $z = 0$  the observed  $T_{s,obs}$  is prescribed, making  $n = 2001$ . By calculating  $\tilde{G}_s$  in this way, the snowpack is regarded as a box containing a certain amount of heat, which is closed at the bottom (no heat exchange at the lower boundary) — the subsurface heat flux at the surface is thus assumed to equal the rate of change of the total heat storage in the snowpack, whether caused by heat diffusion or subsurface radiation absorption. In the terminology of the equations presented above:

$$\tilde{G}_s = G_s - Q \quad (6.12)$$

assuming that other subsurface heat sources or sinks (e.g. wind pumping or water vapour transport) are negligible. In that case,  $\tilde{G}_s$  is the same quantity as in equation 6.1.

## 6.4 Results and comparison with measurement data

As described before, the AWS measurements, as well as the measurements of  $SW_{net}$  and  $LW_{\downarrow}$ , drive the energy balance model. Its performance can be assessed by means of three criteria:

1. Calculated surface temperature  $T_{s,mod}$  and observed surface temperature,  $T_{s,obs}$ , derived from  $LW_{\uparrow}$  measurements, should be in good agreement
2. Calculated  $H_{sen}$  and the directly measured  $H_{sen,obs}$  from the sonic anemometer should be in good agreement,
3. The evolution of subsurface temperatures  $T_{sn,i}$  in the model should agree with observed snow temperatures.

In this section, we present model results in the optimal setting, perform a sensitivity analysis, and demonstrate the role of radiation penetration in the energy budget of the snowpack.

### 6.4.1 Results

The optimal results of the energy balance model, determined by the best performance on the above-mentioned criteria, are shown in figure 6.1, which compares  $T_{s,mod}$  and  $T_{s,obs}$  (criterion 1). This calculation will be referred to as the ‘optimal run’.

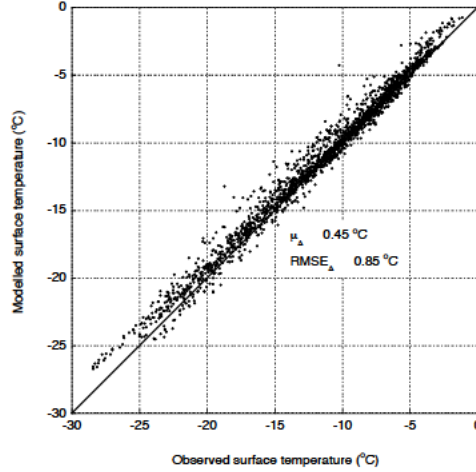


**Figure 6.1:**  $T_{s,mod}$  vs.  $T_{s,obs}$  (in  $^\circ\text{C}$ ) for the optimal run. Radiation penetration is enabled, with  $r_e = 100 \text{ } \mu\text{m}$ , and  $\rho_{sn,rp} = 280 \text{ kg m}^{-3}$ . Roughness length for momentum  $z_{0,u} = 3.8 \times 10^{-4} \text{ m}$ .

The scatter plot in figure 6.1 shows a small, systematic bias towards high  $T_{s,mod}$ , with  $\mu_{\Delta T_s} \equiv \overline{T_{s,mod} - T_{s,obs}} = 0.45^\circ\text{C}$  and a root mean square error ( $\text{RMSE}_{\Delta T_s}$ ) of  $0.85^\circ\text{C}$ . The model performs best for higher temperatures, whereas for lower temperatures,  $T_{s,mod}$  tends to be too high. The discrepancy is not necessarily rooted in the model:  $T_{s,obs}$  could be too low because of an offset in  $LW$  measurements, which would be typically  $1.9 \text{ W m}^{-2}$  for  $0.45^\circ\text{C}$ . This is well within the accuracy of the Eppley PIR pyrgeometers ( $10 \text{ W m}^{-2}$ ). The difference  $\mu_{\Delta T_s}$  turns out to be larger for clear-sky conditions, so either the model performs less well for meteorological conditions under a clear sky, or the measurements of  $LW$  under clear sky are biased — or a combination of both.

In figure 6.2, we show a plot of modelled vs. measured sensible heat fluxes (criterion 2). The agreement is reasonable (correlation coefficient  $r^2 = 0.66$ ). Negative values of  $H_{sen}$  are somewhat underestimated by the model whereas positive values are overestimated.

Lastly, we show the measured and modelled subsurface temperatures at 0.10, 0.50 and 0.75 m below the surface in figure 6.3(a). As is clearly visible in this plot, modelled temperatures follow the measured ones quite well, although they do not match perfectly, and especially in the first weeks of the experiment period, there is some discrepancy in the amplitude of the daily cycle at depth. We will discuss these points in section 6.4.3.

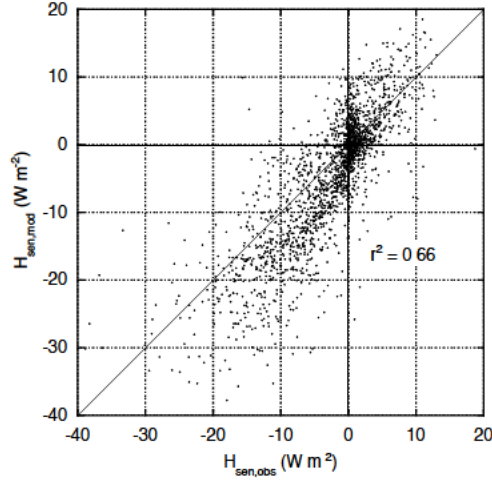
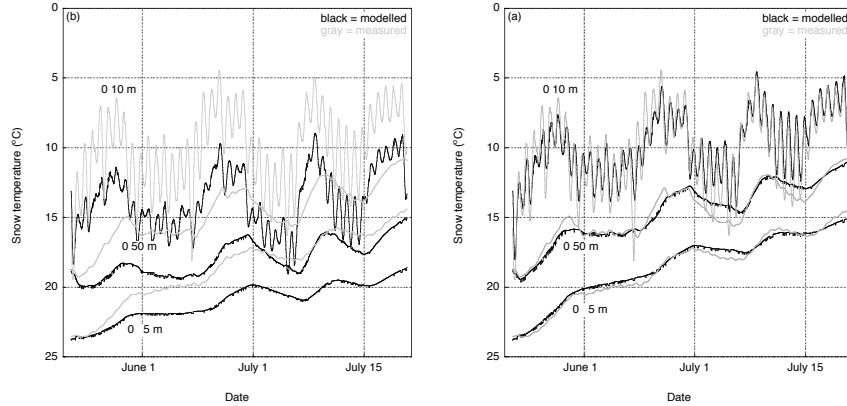


Figure 6.2:  $H_{sen,mod}$  vs.  $H_{sen,obs}$  (in  $W m^{-2}$ ) for the optimal run.

#### 6.4.2 Sensitivity experiments

In order to assess the sensitivity of the energy balance model to its settings and assumptions, we performed many sensitivity tests and compared the model outcome of each test with the optimal run. The results of 8 of these tests are summarized in table 6.1. If  $z_{0,u}$  is multiplied by 10,  $T_{s,mod}$  is hardly affected. Upon division of  $z_{0,u}$  by 10,  $T_{s,mod}$  will deviate more from  $T_{s,obs}$ . Note that, by changing  $z_{0,u}$  in these experiments, the roughness lengths  $z_{0,T}$  and  $z_{0,q}$  are also affected through the relations by *Andreas* [1987]. Limiting the stability correction functions slightly deteriorates the results, whereas omission of the stability correction functions altogether leads to a larger disagreement between  $T_{s,mod}$  and  $T_{s,obs}$ . The latter two tests show that applying an unlimited stability correction to the turbulent fluxes yields the best results. The robustness of the model regarding the turbulence calculations was also demonstrated by *Van As et al.* [2005a].

Furthermore, we tested the sensitivity of model results to errors in the measured input. We varied  $T_{2m}$  by  $\pm 0.1^\circ C$  to show that the model results are moderately affected. A systematic temperature measurement error of  $-0.7^\circ C$  would be necessary to match  $T_{s,mod}$  and  $T_{s,obs}$ , which is deemed very unlikely, since the air temperature measurements excellently agree with the independent thermocouple measurements from the sonic anemometer. Lastly, we increased snow densities  $\rho_{sn}$  and  $\rho_{sn,rp}$  by  $50 kg m^{-3}$ . We found that  $T_{s,mod}$  rises by a moderate  $0.04^\circ C$ . On the other hand, increasing snow density does have a small impact on modelled subsurface temperatures: the increase of  $50 kg m^{-3}$  results in a  $0.66^\circ C$  higher temperature at



**Figure 6.3:** Comparison between modelled (black) and observed (gray) snow temperatures at 0.10 m, 0.50 m, and 0.75 m, for (a) the optimal run with radiation penetration, and (b) the run without radiation penetration, all other settings being equal.

0.75 m after 42 days, and  $+0.55^{\circ}\text{C}$  at 0.10 m. The explanation is that both the extinction of subsurface radiation and the heat conductivity increase, enabling better conduction of more absorbed radiation. However, without modelling radiation penetration, a higher density alone can never explain the observed snow temperatures. Different density-dependent formulations for thermal conductivity  $k_{sn}$  (equation 6.10) have been tried, but the results changed insignificantly. In summary, tweaking the diffusive subsurface heat flux, either by varying  $\rho_{sn}$  or  $k_{sn}$  does not lead to a match between  $T_{s,mod}$  and  $T_{s,obs}$ .

### 6.4.3 Radiation penetration

As a part of the sensitivity study in section 6.4.2, the radiation penetration module was switched off. The resulting effect on the subsurface temperatures is shown in figure 6.3b. As can be clearly seen, the modelled snow temperatures remain systematically lower than the measured ones. Also, the amplitude of the signal at various time scales is underestimated.

Based on the following arguments, we rule out the possibility that the discrepancy between modelled and observed  $T_{sn}$  can be explained by erroneous measurements due to radiative heating of the sensors: (1) *Brandt and Warren* [1993] performed a field experiment shading the snow surface, and from their findings it can be concluded that radiative heating of thermistors is by far too small at depths greater than 0.10 m to explain the discrepancy between measured and modelled snow temperatures; (2) the discrepancy persists during the night when the solar flux is small. *Brandt and Warren* [1993] showed in their field experiment that errors due to radiative heating of thermistors vanish a few minutes after they are shaded. We would therefore expect that night-time readings are unaffected. What we observe is quite different

**Table 6.1:** Overview of sensitivity studies performed with the energy balance model.

Sensitivity test	$\mu_{\Delta T}$ ( $^{\circ}\text{C}$ )	RMSE $_{\Delta T}$ ( $^{\circ}\text{C}$ )
Optimal run	0.45	0.85
$z_{0,u} \times 10$	0.45	0.87
$z_{0,u}/10$	0.60	1.02
Limited stability correction	0.53	0.93
No stability correction	0.72	1.17
$T_a + 0.1^{\circ}\text{C}$	0.52	0.89
$T_a - 0.1^{\circ}\text{C}$	0.39	0.83
Snow density + 50 kg m $^{-3}$	0.49	0.89
No radiation penetration	0.47	1.03

however: at nighttime, measured and modelled snow temperatures do not converge; (3) the discrepancy between modelled and measured temperatures does not only play a role close to the surface (0.10 m), but also at greater depth (0.50 and 0.75 m). The thermistors are shielded with a white plastic protective cover, that is highly-reflective especially for the wavelengths that do penetrate to these depths. Only for the thermocouple at 0.10 m, the amplitude of the measured  $T_{sn}$  is greater than that of the modelled  $T_{sn}$  until the beginning of July. This could be indicative of a small amount of radiative heating of the thermistor; (4) other studies using exactly identical thermistor strings [Reijmer and Oerlemans, 2002; Van As *et al.*, 2005a] did not detect radiative heating of thermistors either. Rather, we propose that subsurface absorption of shortwave radiation deposits heat in snow below the surface, enabling a more rapid heating of the snowpack than by the subsurface heat flux  $G$  alone.

The amount of shortwave radiation absorbed below the surface is plotted in time in figure 6.4. Most of this radiation is absorbed close to the surface, and rapidly decreases with depth. On average, 6.3% of the incoming solar radiation is absorbed at least 0.5 cm below the surface (in the second and subsequent subsurface model layers), which equals about 37% of  $\text{SW}_{net}$ .

From a physical point of view, subsurface absorption of radiation is emphatically different from the subsurface heat flux. The first is a source term, whereas the latter is a diffusive term. This fundamental difference makes that adding a source term below the surface can successfully close the energy budget of the subsurface, whereas amending the diffusive process of heat conduction, by means of varying either  $k_{sn}$  or  $\rho_{sn}$  (section 6.4.2), cannot. This is illustrated in figure 6.5, in which the subsurface snow temperature profile is plotted at the end of the 42-day experiment. Observed snow temperatures cannot be explained without radiation penetration, nor by increasing the snow density.

While the inclusion of subsurface absorption of radiation changes snow temperatures, it hardly affects the temperature at the surface. In table 6.1, it is shown that the average differ-

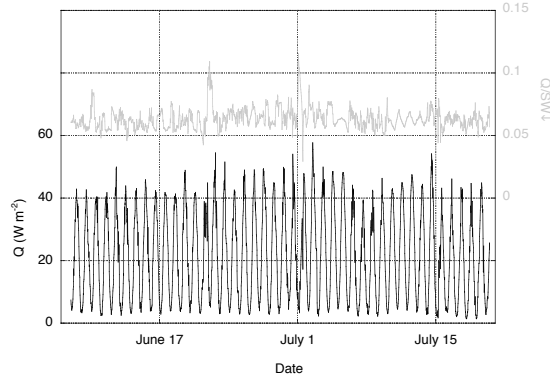


**Figure 6.4:** Amount of radiation absorbed at least 0.5 cm below the surface  $Q$  ( $W m^{-2}$ ) in black, and its fraction of incoming solar radiation  $SW_{\downarrow}$  in gray.

ence between model and observations,  $\mu_{\Delta T}$ , changes insignificantly. This can be explained as follows. Almost all of the penetrated radiation is absorbed a few cm below the surface, leading to some local heating of the snow just below the surface (the ‘solid-state greenhouse effect’ [Brandt and Warren, 1993]). The temperature gradient close to the surface will decrease or even reverse, and as a result,  $G$  increases close to the surface. For the energy balance of the surface layer (see equation 6.9), it means that the diminution of  $SW_{net}$  by the amount  $Q$  is compensated for by an increase of  $G_s$ , leaving  $T_{s,mod}$  almost unaltered.

#### 6.4.4 Radiative transfer modelling of radiation penetration

The radiation penetration model by Brandt and Warren [1993] requires a constant snow grain radius and snow density. From stereographical analysis of snow samples (see below), we know that these quantities vary strongly in the top few cm of the snowpack. We therefore investigated the penetration of shortwave radiation with the DAK radiative transfer model presented in chapters 2 and 3. The scattering functions  $F^a(\Theta)$  (equation 2.12) are calculated using the same ice optical constants as for the snow grains in the two-stream model.

We compared subsurface radiation penetration calculations from the two-stream model with those from the radiative transfer model, applied to the snowpack at Summit. During SURE 07, we collected several snow samples that were used to obtain  $r_e$  and density profiles in the top few cm of the snowpack. At five days between June 29 and July 17, we fixed samples in a dyed solution of diethyl phthalate. These samples were transported to a cold laboratory

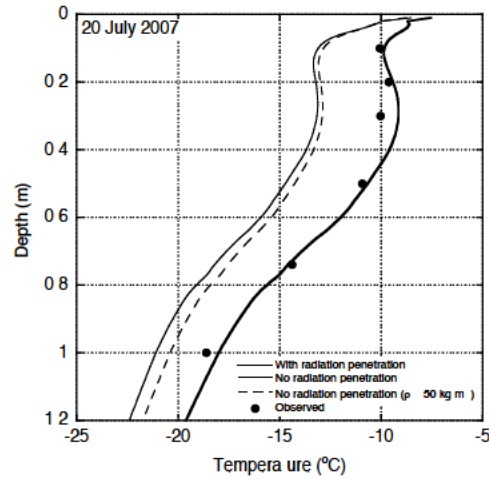


**Figure 6.5:** Temperature profiles at the end of the 42-day experiment, measured (solid dots) and modelled, with radiation penetration (thick solid line), without radiation penetration (thin solid line) and without radiation penetration and higher snow density ( $+50 \text{ kg m}^{-3}$ ).

in Davos, Switzerland, a surface section was cut out, and they were digitally photographed. Unbiased stereological counting of sample slices was used to get detailed profiles of  $r_e$  and snow density in the top 5 to 6 cm [Matz and Schneebeli, 2006]. Density and  $r_e$ -profiles of four of these samples are shown in Figure 6.6, and were prescribed in DAK. We selected four cases of clear-sky conditions close to the time of snow sample collection. For these cases, radiosonde profiles were used to specify the atmospheric composition. Subsurface radiation absorption  $dQ/dz$  profiles calculated by DAK are shown in figure 6.7(a)–(d) (red circles), together with results from the radiation penetration model for several values of  $r_e$  and  $\rho_{s,rp} = 280 \text{ kg m}^{-3}$  (black lines). All four plots show that radiation penetration in a snowpack with variable density and snow grain size is much more irregular than calculated with the idealized two-stream model. For the cases in figures 6.7(a)–(c), DAK results are close to the  $100 \mu\text{m}$ -profiles, while in figure 6.7(d), the  $350 \mu\text{m}$  profile better matches the DAK results. Which snow grain size in the Brandt and Warren [1993] model best describes the amount of absorbed radiation in the two-stream model depends very much on the density and snow grain size in the snow samples, and their vertical distributions.

The comparison between DAK and the two-stream model remains somewhat inconclusive. The vertical distribution of absorbed radiation is shown to be more complex than the two-stream model predicts, and results depend on snow density and snow grain size, as was shown by Brandt and Warren [1993]. Measured snow grain sizes range from 100 to  $500 \mu\text{m}$ , and

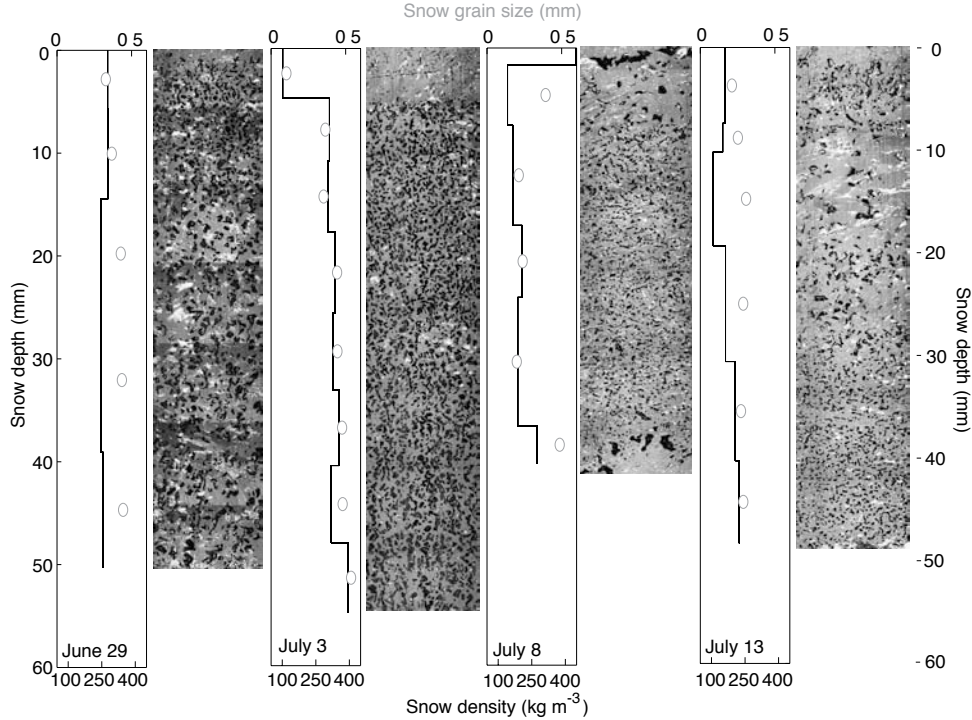


**Figure 6.6:** Profiles of snow density (black lines, lower horizontal axis) and snow grain size (gray circles, upper horizontal axis), from stereographical analysis of snow samples. The dates on which the snow samples were collected are displayed in each frame.

densities from  $100$  to  $450 \text{ kg m}^{-3}$ , but as figure 6.7 shows, the amount of absorbed radiation is sometimes better represented by choosing  $r_e = 100 \mu\text{m}$  in the two-stream model, and at other times,  $r_e = 350 \mu\text{m}$  fits better. For the simulation of snow temperatures by the energy balance model however, only  $r_e = 100 \mu\text{m}$  gives correct results for the entire period. Whether this contradicts snow grain size measurements cannot be concluded unambiguously. Unfortunately, a coupling between the DAK model and the energy balance model is computationally prohibitive at present.

Both Colbeck [1989a] and Alley *et al.* [1990] have shown that radiation penetration facilitates the emergence of low-density snow layers (depth hoar) just below the surface, so that radiation penetration, subsurface heat flux, snow grain size and density become coupled. In our model, these couplings are all absent. Despite the above, the conclusion remains that the inclusion of subsurface absorption of solar radiation is crucial for modelling the energy budget of both the surface and the subsurface correctly.

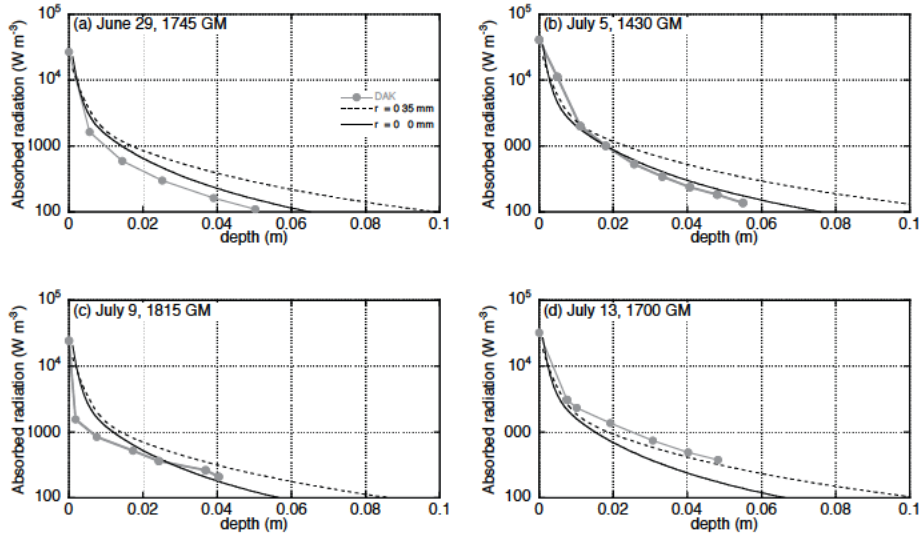


**Figure 6.7:** Profiles of absorbed radiation in  $W m^{-2}$  per  $m$ . Gray circles are calculations with the radiative transfer model DAK, whereas black lines are profiles from the two-stream model for snow grain radius  $100 \mu m$  (solid) and  $350 \mu m$  (dashed).

### 6.4.5 The diurnal cycle

To conclude section 6.4, the diurnal cycle of the components of the surface energy budget is presented, averaged over the entire measurement period. We compare our results with those reported by Hoch [2005] (H05) in June and July of 2001 and 2002.

Figure 6.8 shows this diurnal cycle. By far the largest source of energy at the surface is  $SW_{net}$  ( $+61 W m^{-2}$  on average; H05:  $+60 W m^{-2}$ ), whereas the largest sink is  $LW_{net}$  ( $-42 W m^{-2}$ ; H05:  $-45 W m^{-2}$ ). The average  $LW_{net}$  minimum value of  $-60 W m^{-2}$  occurs close to local noon (14:33 UTC), demonstrating that the temperatures of the surface snow and the air are instantly governed by solar radiation. Due to the inland location of Summit, advection of warmer air is negligible.

The turbulent fluxes are of comparable magnitude:  $H_{sen}$  and  $H_{lat}$  amount to  $-5$  and  $-7 W m^{-2}$ , respectively (H05:  $-1 W m^{-2}$  and  $-9 W m^{-2}$  respectively), and act as small heat sinks. Between 21:00 and 06:00 UTC,  $H_{sen}$  is a very small source of heat in a stably stratified near-surface boundary layer. Stronger mixing during daytime causes transport of heat from the surface to the air, as well as a small amount of sublimation (negative  $H_{lat}$ ). On average,

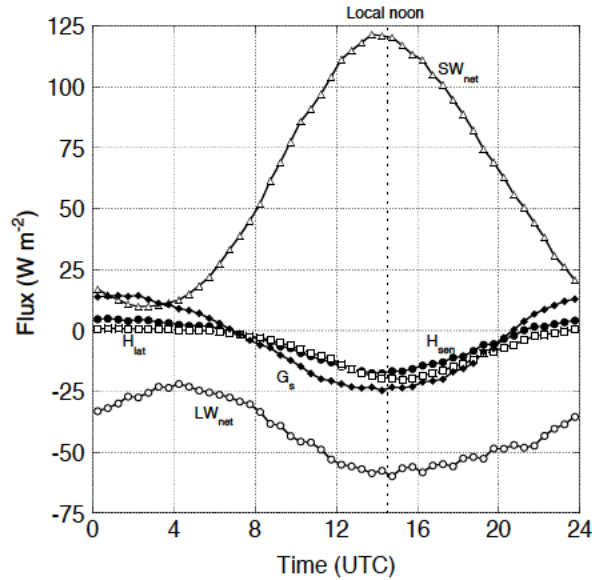


**Figure 6.8:** Average diurnal cycle of the surface energy balance components [ $\text{W m}^{-2}$ ]. Shown are net solar radiation (triangles), net longwave radiation (open circles), turbulent sensible (solid circles) and latent (open squares) heat fluxes, and subsurface heat flux (solid diamonds). The dashed vertical line represents the local noon at 14:33 UTC.

there is a very small amount of net deposition (fallout) or downward water vapour transport at nighttime (positive  $H_{lat}$ ), although this is confined to a few nights during the measurement period. Combining the effects of diffusion from surface temperature, and radiation penetration,  $\tilde{G}_s$  is  $-5 \text{ W m}^{-2}$  on average during the campaign (H05:  $-7 \text{ W m}^{-2}$ ), reflected in a continuous heating of the snowpack (figure 6.3). The maximum cooling rate (positive  $\tilde{G}_s$ ) of the snowpack is about  $+14 \text{ W m}^{-2}$  at night, and the maximum heating rate about  $-25 \text{ W m}^{-2}$  during daytime.

*Cullen and Steffen* [2001] report higher  $SW_{net}$  ( $+82 \text{ W m}^{-2}$ ) and lower  $LW_{net}$  ( $-68 \text{ W m}^{-2}$ ) values, but those were obtained in a period with dominantly clear-sky conditions.

## 6.5 Discussion and conclusions

In this chapter, we presented measurements and model results of the components of the energy balance of the snowpack at Summit, Greenland, during a 42-day period in June and

July 2007. The energy balance model simulates observed snow surface temperatures well, although on average modelled and observed snow surface temperatures differ by 0.45 °C. The energy balance model was shown to be somewhat sensitive to the prescribed surface roughness length, and to small errors in input 2-meter temperatures. Furthermore, the subsurface temperatures slightly depend on the prescribed snow density profile, but the effect is small in general. It was found that observed subsurface temperatures could not be reproduced without including a radiation penetration term in the energy balance model. Although observed snow grain radii in the top 5 cm range from 100 to 500  $\mu\text{m}$ , subsurface temperatures could only be reconstructed using a radius of 100  $\mu\text{m}$ . The use of a sophisticated radiative transfer model could not solve this possible discrepancy unambiguously, although for 3 out of 4 test cases, the 100  $\mu\text{m}$ -profiles fit the radiative transfer model calculations best. Nevertheless, we argued that the inclusion of a radiation penetration term is required to close the energy budget of the snowpack satisfyingly.

A natural question that comes to mind is why subsurface absorption of shortwave radiation is apparently important at Summit, while it has not been reported to be necessary to close the energy budget at other locations, either those like Hardangerjøkulen, a small, temperate ice cap in Norway [Giesen *et al.*, 2008], or in similar circumstances like the Antarctic Plateau [Van den Broeke *et al.*, 2004c; Van As *et al.*, 2005a]. In the case of measurements on Hardangerjøkulen and melting glaciers in general, the energy fluxes from melt and internal refreezing, and the associated model uncertainties, largely exceed those of absorbed subsurface radiation or the subsurface heat flux, making it hard to assess what importance radiation penetration has in the heating of the snowpack. Before the start of the melt season at Hardangerjøkulen, the modelled snow temperatures are in fact lower than the measured ones [R. H. Giesen, personal communication, 2009], suggesting that radiation penetration has some effect on snow temperature, but this might also be attributed to some intermittent meltwater percolation and refreezing, not captured by the model. Considering that, on glaciers, snow grains can become large, snow can get wet or bare ice can appear at the surface, the magnitude of absorbed subsurface radiation will be larger than at Summit, but still smaller than melt energy fluxes. Regarding the Antarctic Plateau measurements, it could be that a combination of larger snow density [Van As *et al.*, 2005a] and smaller snow grains (chapter 4) makes the effect much less apparent, but this requires further study.



## Spectral snow albedo and snow grain size

### Summary

In this chapter, we present measurements of spectral snow albedo, carried out at Summit, Greenland. Concurrently, we collected snow samples that were stereologically analyzed and that provided high-resolution vertical profiles of snow grain size. These profiles were used in the radiative transfer model DAK to calculate spectral albedo of snow. We show that there is a good agreement between the radiative transfer model results and the observations of spectral albedo. Thus, it is experimentally shown that the optical properties of a natural snowpack are determined by its physical properties. For correctly modelling spectral albedo, it is necessary to include a thin ( $\sim 0.5$ – $1.0$  mm) top layer of small snow grains, as suggested in previous literature. These small layers are also present in the observed snow profiles, stressing the need to measure snow grain size at millimeter resolution close to the surface.

## 7.1 Introduction

In chapter 4, we saw that the broadband albedo ( $\alpha$ ) of a snow surface is highly variable, even in the dry-snow zones of ice sheets. Observed values are typically between 0.78 and 0.84 under clear skies [Van den Broeke *et al.*, 2004a], and even higher when clouds are present. In chapter 4, I suggested that for dry snow, spatial and temporal variations in clear-sky albedo are mainly due to variability in the size of the surface snow grains. Spatial variations in snow grain size on Antarctica are demonstrated by a MODIS (Moderate resolution Imaging Spectrometer) snow grain size product [Scambos *et al.*, 2007], showing small grains on the Plateau and larger grains in coastal areas. The resulting variations in albedo have important implications for the energy budget of the snow surface: absorbed solar radiation is proportional to  $1 - \alpha$ , and so for high-albedo surfaces, a small change in albedo has a profound effect on the amount of absorbed radiation available for heating of the snowpack. Knowledge of the spectral optical properties of natural snow surfaces is therefore important.

It has been well established theoretically that snow microstructure has an effect on the optical properties of the snowpack, as I discussed in chapter 3. Wiscombe and Warren [1980] put forward a model based on Mie theory, that clearly demonstrates that larger snow grains decrease broadband albedo due to increased scattering of radiation in the forward direction. Flanner and Zender [2006] link the evolution of snow microstructure (i.e. changes in shape and size of snow crystals) to changes in broadband surface albedo.

The computation of the optical properties of irregularly-shaped snow crystals is difficult, but a versatile approximation is to replace the snow crystals with spherical snow grains that have the same volume-to-surface (V/S) ratio [Dobbins and Jizmagian, 1966; Warren, 1982, chapter 3 of this thesis]. The success of this approach has been underlined by Grenfell and Warren [1999] and Neshyba *et al.* [2003] for cylindrical and hexagonal-plate shaped crystals. Essentially, this approximation allows one to convert the specific surface area (SSA) [ $\text{m}^{-1}$ ] of any crystal shape mixture to an optically-equivalent snow grain radius  $r_e$  [m]. SSA is defined as the ratio between surface area and volume of the ice constituting the snow grains [Warren, 1982; Legagneux and Domine, 2005], and  $r_e$  is the radius of the equivalent V/S spheres that replace the actual snow crystals [Mitchell, 2002]. Measuring SSA (and thus  $r_e$ ) is therefore a useful way to link snow microstructure observations with radiative transfer model calculations using spherical particles.

Recently, there has been a considerable advance in fast and quantitative methods to obtain the SSA of snow samples. Among these methods are contact spectroscopy using the ice absorption feature at 1030 nm [Painter *et al.*, 2007], an integrating-sphere measurement of spectral albedo at 1310 and 1550 nm [Gallet *et al.*, 2009] and a combination of stereology and near-infrared (NIR) photography [Matzl and Schneebeli, 2006]. Apart from these optical methods, Legagneux *et al.* [2002] put forward a method based on the adsorption of methane in snow samples to determine SSA.

There are numerous accounts in literature on measurements of spectral snow albedo [Kuhn and Siogas, 1978; Grenfell and Perovich, 1984; Grenfell *et al.*, 1994; Zhou *et al.*, 2003; Wutke *et al.*, 2006], many of which were performed in the Antarctic. Fewer are the attempts to compare observed spectral snow albedo with radiative transfer calculations over a snowpack using concurrent observations of snow grain size. Grenfell *et al.* [1994] compare measurements of albedo throughout the shortwave spectrum with traditional snow grain size measurements. Domine *et al.* [2006] combine methane-adsorption measurements of SSA with spectral albedo measurements at 4 wavelengths between 1310 and 2260 nm. However, these optical measurements are done on snow samples, not above a natural snow surface. It means that, for the optical characterization of the snow, the natural snow is disturbed in order to obtain a sample volume. The same is true for the study by Gallet *et al.* [2009].

In this chapter, we combine field observations of spectral snow albedo with highly detailed observations of SSA (and using the equal V/S approximation also  $r_e$ ) in the first few centimeters of the snowpack. Both the optical characterization of the snow and the determination of SSA is done on a virtually undisturbed snow surface.

In section 7.2, we will present the data and methods that are used for this study, and explain the corrections that have been applied to the data. In the subsequent section, we will show examples of spectral albedo, show the consistency of the results, and compare the spectral albedo measurements with radiative transfer calculations. In section 7.4, the results are discussed and this chapter is concluded.

## 7.2 Data and methods

The data used in this study were collected during the 42-day Summit Radiation Experiment 2007 (SURE '07) in June and July 2007 at the Greenland Environmental Observatory at Summit (72°34' N 38°28' W, 3209 m a.s.l.), on top of the Greenland Ice Sheet (see section 1.6).

### 7.2.1 Spectroradiometer

Spectral snow albedos were collected using an ASD (Analytical Spectral Devices) FieldSpec Pro FR spectroradiometer, covering the solar spectrum between 350 and 2500 nm in 1 nm intervals. The spectral resolution (full width at half-maximum) is 3 nm at 700 nm and 10 nm at 1400 and 2100 nm. Hemispherical spectral irradiances [ $\text{W m}^{-2} \text{nm}^{-1}$ ] were recorded using a white diffuser plate that guides radiation from a half-sphere into a fiber optical cable to the spectroradiometer. Incoming spectral irradiance  $E_{\lambda\downarrow}$  was measured by leveling the diffuser plate horizontally, viewing the sky, whereas reflected spectral irradiance  $E_{\lambda\uparrow}$  was measured

in the opposite direction, facing the snow surface. Using the definition

$$\alpha_\lambda = \frac{E_{\lambda\uparrow}}{E_{\lambda\downarrow}}, \quad (7.1)$$

spectral albedo  $\alpha_\lambda$  as a function of wavelength  $\lambda$  is calculated. Each measurement of  $E_\lambda$  is an average of 15 consecutive scans. Pairs of  $E_{\lambda\downarrow}$  and  $E_{\lambda\uparrow}$  measurements were collected by alternating upward- and downward-looking measurements, and five of these pairs were combined to obtain one average spectrum of  $E_{\lambda\downarrow}$ ,  $E_{\lambda\uparrow}$ , and  $\alpha_\lambda$ . So all in all, an average albedo spectrum  $\alpha_\lambda$  is based on  $2 \times 5 \times 15 = 150$  scans, 75 of which are  $E_{\lambda\downarrow}$ , and 75 are  $E_{\lambda\uparrow}$ . Recording one such average albedo spectrum takes about 10 minutes. A measurement error  $\sigma_E(\lambda)$  is determined using the standard deviation of these 75 spectra. The measurement error in albedo  $\sigma_\alpha(\lambda)$  is calculated from  $\sigma_{E_\downarrow}(\lambda)$  and  $\sigma_{E_\uparrow}(\lambda)$ , assuming that these are independent.

Between 16 June and 16 July 2007, 112 of these averaged spectra were collected during widely varying illumination conditions, under clear and overcast skies, and with the solar zenith angle  $\theta_0$  ranging from  $49.1^\circ$  to  $83.0^\circ$ . The change of the solar zenith angle  $\theta_0$  during the measurements is corrected for.

## 7.2.2 Spectroradiometer corrections

Following Grenfell *et al.* [1994], we applied a wavelength-dependent correction to the irradiance spectra for the non-ideal cosine response of the diffuser plate. If the measured response is  $S_\lambda(\theta)$ , the response correction is given as  $f_\lambda(\theta) = S_\lambda(\theta)/\cos\theta$ . For direct incident radiation arriving from solar zenith angle  $\theta_0$ , the correction becomes

$$E_{\lambda\downarrow}^{dir}(\text{true}) = \frac{E_{\lambda\downarrow}^{dir}(\text{observed})}{f_\lambda(\theta_0)}. \quad (7.2)$$

Also for diffuse irradiance, a correction  $C_\lambda$  is necessary, such that

$$E_{\lambda\downarrow}^{dif}(\text{true}) = C_\lambda E_{\lambda\downarrow}^{dif}(\text{observed}) \quad (7.3)$$

Assuming that the diffuse irradiance is isotropic,  $C_\lambda$  is given as

$$C_\lambda = \left[ 2 \int_0^{\pi/2} f_\lambda(\theta) \sin\theta \cos\theta d\theta \right]^{-1}. \quad (7.4)$$

See Grenfell *et al.* [1994] for a more complete derivation. Considering that a fraction  $F_\lambda^{dif}$  of the incoming irradiance is diffuse, and that  $F_\lambda^{dif} + F_\lambda^{dir} = 1$ , the true spectral albedo can be

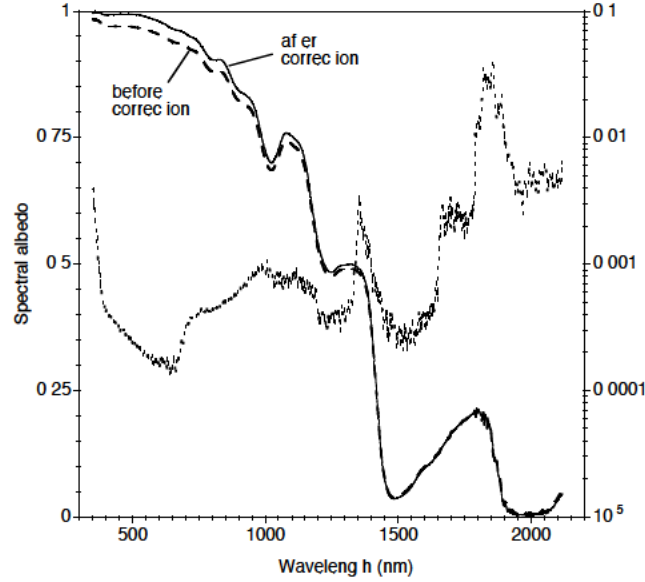


**Figure 7.1:** Example of the correction of a clear-sky snow albedo spectrum as a function of wavelength. The scale for the uncorrected (dashed line) and corrected (solid line) albedos is on the left, while the logarithmic scale on the right corresponds to the standard deviation of the corrected spectrum (dotted line). The spectrum was recorded on 5 July 2007, 14:00 UTC.

calculated:

$$\alpha_{\lambda} = \frac{C_{\lambda} E_{\lambda \uparrow}(\text{obs})}{C_{\lambda} F_{\lambda}^{\text{dif}} E_{\lambda \downarrow}(\text{obs}) + (1 - F_{\lambda}^{\text{dif}}) E_{\lambda \downarrow}(\text{obs}) / f_{\lambda}(\theta_0)} \quad (7.5)$$

Unfortunately, we did not have measurements of  $f_{\lambda}(\theta)$  for our own instrument. We therefore used a function for another instrument of exactly the same type [T. Malthus, personal communication, 2009], adapted to yield realistic albedo curves in the visible part of the spectrum. Especially above  $\theta = 70^{\circ}$  however, the correction factor  $f_{\lambda}(\theta)$  can deviate significantly from one, so the corrections become quite large. Since it is uncertain to what extent  $f_{\lambda}(\theta)$  is transferable from one instrument to another, the induced errors could become large.

The spectral diffuse fraction  $F_{\lambda}^{\text{dif}}$ , required for equation 7.5, was calculated using the radiative transfer model presented in section 7.2.4, for various values of  $\theta_0$ . For overcast skies, we assumed  $F_{\lambda}^{\text{dif}} = 1$ , and the correction for the albedo drops out of equation 7.5 [Grenfell et al.,

1994].

Next, we corrected for the fraction of the field-of-view of the diffuser plate that was occupied by the instrument casing during measurements of  $E_{\lambda,\uparrow}$  [see *Wuttke et al.*, 2006, their equation 4]. For each measurement of the reflected spectral irradiance, we assumed an occupied fraction of the field-of-view of 0.018, and a wavelength-independent albedo of the instrument casing of 0.20. This correction leads to slightly higher albedos (up to +0.01) in the visible part of the spectrum.

Despite the correction for the non-ideal cosine response of the diffuser plate, measurements under clear sky with  $\theta_0 > 70^\circ$  feature visible albedos  $> 1$  and larger uncertainties of spectral albedo in the NIR region due to very small irradiances. The high visible albedos suggest that the cosine response correction  $f_\lambda(\theta)$  is not adequately known for high  $\theta$ . Therefore, clear-sky measurements for  $\theta_0 > 70^\circ$  are discarded. Furthermore, cloudy-sky measurements for which the irradiance was insufficiently stable (e.g. due to rapidly fluctuating cloud optical thickness) were discarded as well. Out of the 112 averaged spectra, we retain 18 spectra under a completely clear sky, 29 spectra under skies with 1/8 cloud cover (not blocking the sun), and 11 spectra under homogeneous cloud cover. Cloud cover was determined by eye, and checked with observations from a Total Sky Imager.

An example of a clear-sky spectral albedo measurement before and after corrections is shown in figure 7.1. Note that irradiance measurements turned out not to be reliable between 2120 and 2380 nm, due to a low signal-to-noise ratio of the spectroradiometer. Spectral albedo curves are therefore shown up to 2120 nm. The corrections are most prominent in the visible and decrease towards the NIR. Also shown in figure 7.1 is the measurement error  $\sigma_\alpha(\lambda)$ , which steadily grows between 500 and 2200 nm. Local maxima occur around 1350 and 1850 nm, where absorption by water vapour causes larger uncertainties in  $E_{\lambda,\downarrow}$ .

### 7.2.3 Snow grain size profiles

During SURE '07, we collected several snow samples that were used to obtain SSA and density profiles in the top few cm of the snowpack (see also sections 1.6 and 6.4.4). At five days between June 29 and July 17, we fixed samples in a dyed solution of diethyl phthalate. These samples were transported to a cold laboratory in Davos, Switzerland, a surface section was cut out, and they were digitally photographed. Unbiased stereological counting of sample slices [*Matzl*, 2006] was used to get detailed profiles of snow grain size and snow density in the top 5 to 6 cm. Invoking the equal-V/S theory, the inverse of SSA is proportional to the optically-equivalent snow grain radius  $r_e$  [m]. For the top 5 mm, the resolution of the stereological grid was increased by a factor of 3 (nine times more grid points) to capture variability very close to the surface. The results are independent on the resolution of the stereological grid.

In figure 7.2, we show the uppermost millimeters of the vertical snow grain profiles taken on

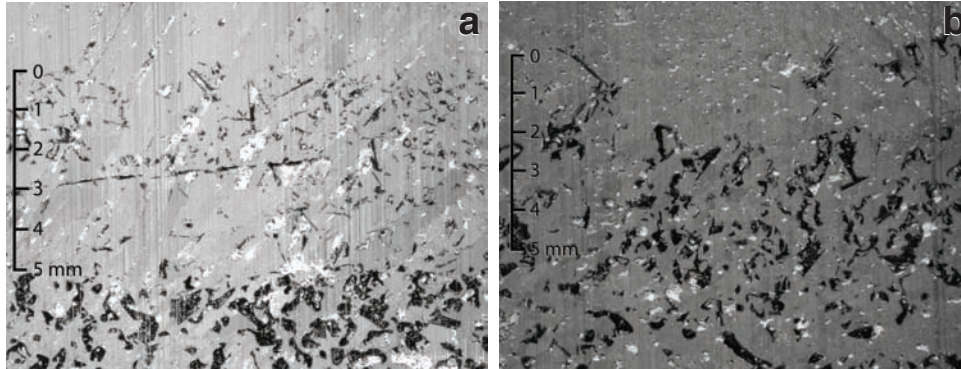


**Figure 7.2:** Observed surface snow grains on (a) 3 July 2007, and (b) 13 July. Snow grains are in black, the white spots are air bubble inclusions and should be ignored. A scale is shown on the left of each panel.

July 3 and July 13. In section 7.3.4, these profiles will be used in two case studies (I and II) that compare observations of spectral albedo with radiative transfer modelling calculations (section 7.2.4). In figure 7.3, the vertical profiles of  $r_e$  for both cases are shown. On 3 July, the topmost 5 mm consisted of very fine wind-broken snow crystals, with an effective snow grain radius of  $0.053 \pm 0.018$  to  $0.096 \pm 0.010$  mm. Below this layer,  $r_e$  ranges from  $0.35 \pm 0.04$  to  $0.54 \pm 0.05$  mm. On 13 July, the topmost 5 mm has an  $r_e$  of  $0.053 \pm 0.022$  to  $0.151 \pm 0.015$  mm. Deeper down, the snow grain radius ranges from  $0.25 \pm 0.03$  to  $0.53 \pm 0.05$  mm. Errors are larger for thinner layers where the statistics of the stereological method is based on smaller numbers.

## 7.2.4 Radiative transfer model

For the modelling of spectral snow albedo, we use the broadband doubling-adding radiative transfer model DAK, that I presented in chapters 2 and 3.

## 7.3 Results

### 7.3.1 Comparison with broadband measurements

In order to assess the quality and consistency of the spectral measurements, the observed and corrected spectra were integrated between 350 and 2500 nm, and compared to broadband pyranometer measurements. The latter are of the type Kipp & Zonen CM21 and have a range

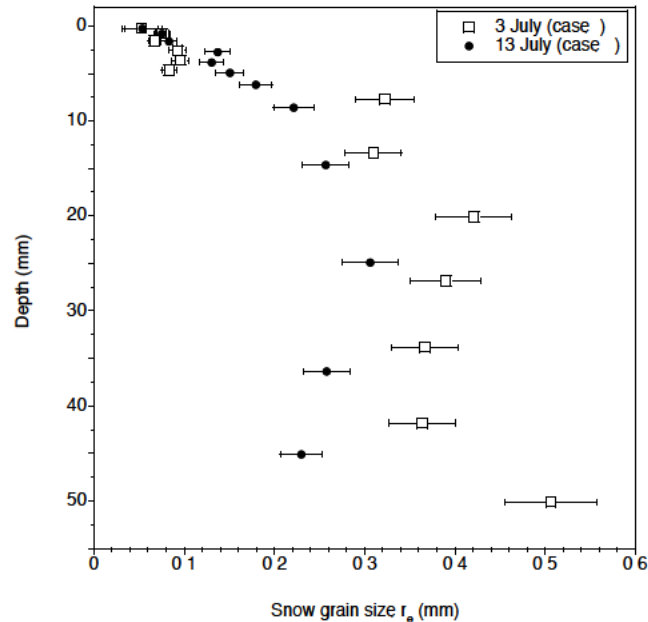


**Figure 7.3:** Stereographically determined vertical profiles of effective snow grain size  $r_e$  as a function of depth, for the snow samples taken on 3 July (case I, open squares) and 13 July (case II, solid circles).

from 300 to 3000 nm. To correct for these different wavelength ranges, a correction was applied, based on typical irradiance spectra. For clear skies, integrated spectral irradiance is multiplied by 1.0204, and for overcast conditions, this multiplication factor is 1.0294.

For the calculation of broadband albedos from the integration of spectral albedos, the spectrum between 2120 and 2380 nm, that is affected by the low signal-to-noise ratio, is replaced by a scaled typical solar spectrum for Summit obtained with a radiative transfer model, for either clear or overcast skies. Integrated irradiance spectra are plotted against broadband irradiances in Figure 7.4, for clear, almost clear, and overcast skies. The left panel shows incoming irradiance and the right panel shows reflected irradiance. Both for incoming and reflected irradiance, the spectral integration yields lower irradiances than measured by the pyranometers. For incoming radiation, the integrated spectra values are on average 7.7% lower than pyranometer values (slope 0.9235,  $r^2 = 0.99$ ), and for reflected radiation, the integrated spectra values are on average 6.3% lower (slope 0.9371,  $r^2 = 0.97$ ). Thus, the spectroradiometer underestimates the total amount of shortwave irradiance. There appears to

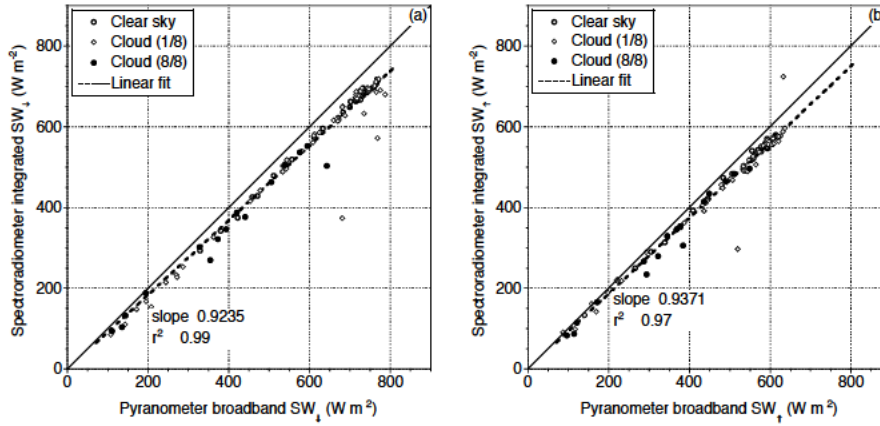


**Figure 7.4:** (a) Integrated incoming irradiance [ $\text{W m}^{-2}$ ] versus broadband irradiance measured by a pyranometer. Open circles are measurements under clear sky; open diamonds are measurements with 1/8 cloud cover, and solid dots represent measurements under homogeneous 8/8 cloud cover. The dashed line is a line fitted to all points, and has a slope of 0.9235; (a) Idem for reflected irradiance, fit slope 0.9371.

be no dependence of this deviation on solar zenith angle or cloudiness: therefore, the cause of this underestimation is likely contained in the diffuse fraction. Lack of knowledge of the actual spectral diffuse fraction  $F_\lambda$ , and the possibly large errors in  $f_\lambda(\theta)$  for high  $\theta$ , could explain the underestimation. Another possible explanation is a non-perfect absolute calibration. This would not influence spectral albedos in the remainder of this chapter, however. The random spread around the trend lines in figure 7.4 is on average 4.3% (incoming) and 3.6% (reflected) of the integrated value, which seems reasonable given typical random errors for broadband pyranometers equipped with a white diffuser plate, and considering errors from continuous realignment of the diffuser plate after one measurement of spectral irradiance.

### 7.3.2 Cloudy-sky spectral measurements

Out of the 11 spectra recorded under homogeneously cloudy skies, 4 were taken later than 22:00 UTC, when  $\theta_0 > 74^\circ$ . These 4 spectra feature somewhat inconsistent visible albedos, and the calculated spectral albedo is noisy in many parts of the spectrum where the incident irradiance is very low. We therefore show spectral albedos of the remaining 7 spectra only, in figure 7.5. The two spectra from 26 June are very alike, and so are those from 7 July in

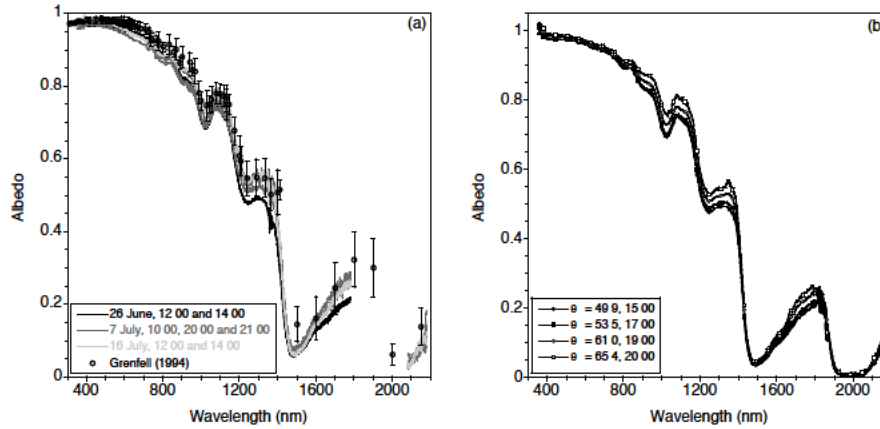


**Figure 7.5:** (a) Observed spectral albedo for 7 cloudy-sky cases. Also shown are measurements by Grenfell *et al.* [1994] for the snow surface at South Pole and Vostok, Antarctica, with corresponding error bars; (b) observed spectral albedo on 5 July 2007 during clear-sky conditions, at different times of the day. Clearly visible is the dependence of spectral albedo on solar zenith angle  $\theta_0$ .

the evening, and from 16 July. For comparison, the spectral albedo measured at South Pole and Vostok [Grenfell *et al.*, 1994] is plotted in the same figure. There is a good agreement between the observations by Grenfell *et al.* and ours, except that we sometimes find somewhat lower albedos in the visible range. Furthermore, our albedo around 1500 nm is lower than that of Grenfell *et al.*. Both Flanner *et al.* [2007] and I (chapter 3) experienced that their modelled albedo at 1500 nm was lower than measured by Grenfell *et al.*, so the measurements by Grenfell *et al.* could well be slightly erroneous in this part of the spectrum.

### 7.3.3 Clear-sky spectral measurements

Opposed to cloudy-sky spectral measurements, the solar zenith angle  $\theta_0$  has an effect on clear-sky spectral snow albedo. We have observed this effect, presented in figure 7.5. To minimize the effect of changing snow properties on spectral albedo, we selected spectral albedos from one clear day only (5 July), and show spectral albedo measurements at different times of that day in the figure to illustrate the effect of  $\theta_0$ . As  $\theta_0$  increases, the measured spectral albedo increases, most prominently for the NIR region covered by the spectrometer (800 – 2200 nm). This entirely accords with both theoretical considerations [Wiscombe and Warren, 1980], albedo modelling results [Aoki *et al.*, 1999, and chapter 3 of this thesis] and

observational evidence from different locations [Grenfell *et al.*, 1994].

### 7.3.4 Spectral albedo modelling

An effort was made to simulate the observed spectral albedo using a radiative transfer model that includes both the atmosphere and the snowpack. We considered two cases of clear-sky measurements: in case I, we use the spectral albedo measurement on 5 July at 14:30 UTC with a vertical profile of snow grain measurements taken on 3 July. Case II is the spectral albedo measurement on 13 July at 19:00 UTC, combined with the vertical snow grain profile taken a few hours earlier on the same day. The model atmospheres for both cases were based on the standard subarctic summer atmosphere [Anderson, 1976], adapted with temperature, pressure and specific humidity measurements from weather balloon data taken daily at 14:00 UTC. Unfortunately, exactly on 5 July, the weather balloon data was not captured due to a software error, so for case I we used an atmospheric profile from another clear day, scaled with surface temperature, pressure and humidity as observed on 5 July at 15:00 UTC. The associated error is likely very small, as the impact of atmospheric composition on snow albedo is small, both broadband (chapter 4) and spectral (not shown).

In the left panel of figure 7.6, we present results for the simulation of case I. The agreement between observations and model results is good throughout the solar spectrum, although between 500 and 850 nm, the model albedos are a little lower than the observed ones. An important detail in the visible part of the spectrum is that we measured an albedo maximum of 0.987 between 440 and 480 nm, apparently in line with findings from Grenfell *et al.* [1994], who found spectral albedo peaking at 0.982 between 400 and 540 nm at South Pole and Vostok, Antarctica. However, the spectral albedo curve is very flat for these wavelengths, and measurement uncertainties are large enough in this part of the spectrum to be able to shift the peak albedo to smaller wavelengths: therefore, it cannot be ruled out that the true peak albedo wavelength is lower than 440 nm. The model albedo peaks earlier and higher, at more than 0.99 at 390 nm, which is due to the prescribed absorption coefficients published by Warren *et al.* [2006]. It is unclear why the measured peak albedo (0.987) is lower than the modelled peak albedo ( $> 0.99$ ), but it is likely beyond the accuracy limits of the spectroradiometer and the measurement setup. It cannot be attributed to impurities in the snowpack, as the concentration of black carbon in the surface snow at Summit is so low, in the order of 1.0–2.0 ng g<sup>-1</sup> [Hagler *et al.*, 2007], that it has an undetectable influence on spectral albedo, even for the visible part of the spectrum (see also chapter 3).

The right panel of figure 7.6 shows the results for the simulation of case II. Again, the model results are in good agreement with the observed spectral albedo, although in the visible part of the spectrum, modelled albedo is somewhat higher than the observations. The spikes around 1800 nm in the observed spectral albedo are due to a low signal-to-noise ratio of the spectroradiometer.

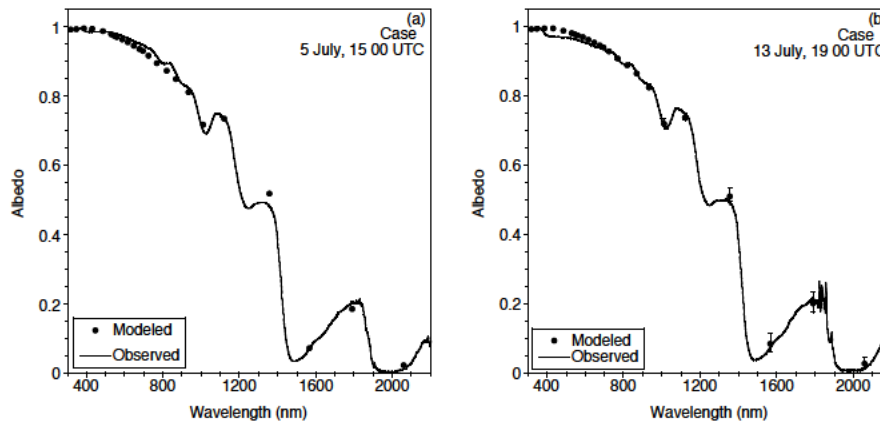


**Figure 7.6:** (a) Observed spectral albedo (black lines) and modelled spectral albedo, for case I, 5 July at 15:00 UTC; (b) *idem* for case II, 13 July at 19:00 UTC.

*Grenfell et al.* [1994] found a discrepancy between observed and modelled spectral albedo as they compared radiative transfer computations for a snowpack of 0.1 mm radius grains with spectral measurements made above a snowpack that contained snow grains with a radius of 0.1 mm (derived from snow microphotography). They found a much better match between model results and observations by including a 0.25 mm thick surface layer of smaller snow grains (0.03 mm radius). Since the absorption coefficient for ice above 1400 nm is so large, only the uppermost snow grains in the snowpack can contribute to scattering. *Grenfell et al.* [1994] did not recognize the importance of this effect at the time of their field research, so they could not back this two-layer setup with observations from the uppermost (sub-)millimeter of the snowpack. They motivated the two-layer configuration by suggesting that the smallest snow grains are suspended longer in the air during episodes of strong wind, and always settle on top when the wind diminishes. Using high-resolution stereology, we are now able to detect this sub-millimeter surface layer. Therefore, we can confirm that the approach taken by *Grenfell et al.* [1994] is a valid one, and perhaps, the presence of the thin layer is a regular feature of dry snow surfaces on polar ice sheets.

To assess the uncertainty of NIR albedo due to measurement uncertainty of snow grain size in the uppermost layer, we performed the radiative transfer computations using the lower and higher bounds of  $r_e$  for each layer, and plotted these as error bars in figure 7.6(b). Beyond 1000 nm, the accuracy of the model results is decreased, but observations still agree well with model results.

## 7.4 Discussion and conclusions

In section 7.3, we have demonstrated the ability of the radiative transfer model to simulate observed spectral albedo curves closely. We have shown experimentally that there is a direct link between the microstructure of the surface snow and the observed spectral surface albedo. Of key importance for a good agreement between spectral albedo measurements over a snow surface and modelling results is the availability of vertical profiles of snow grain size at a sufficiently detailed resolution, in the order of 1 mm. Below, we will discuss possible sources of error in our study, and discuss the possibilities and limitations of existing SSA-retrieval methods to relate spectral albedo measured over a snow surface to the snow microstructure.

A possible source of error in case I is that there are two full days between the snow sampling (3 July) and the spectral albedo observations (5 July). It is possible that the snow surface has changed during these days, but on the other hand, the weather was sunny, cold, almost windless and without snowfall during these two days, implying that no wind crust has formed, no small grains were deposited on top, no snow was eroded away, and that little snow metamorphism has taken place. If anything, sublimation due to turbulent latent heat fluxes of approximately  $-15 \text{ W m}^{-1}$  during the day helped to maintain small snow grains near the surface (chapter 6). We argue that the vertical profile of snow grains must have been much alike on 3 and 5 July, at least within the error bounds shown in figure 7.3.

Stereological analysis of snow crystals in very thin layers poses the problem that these layers become as thin as the typical surface roughness of a natural snow surface. While the calculation of SSA and  $r_e$  is independent of the (somewhat arbitrary) definition of the snow surface in the stereology images, the snow density needed for the radiative transfer calculations is not. We assume however that the impact of this error on the radiation calculations is not larger than the uncertainty of the modelled spectral albedo caused by the uncertainty in the determination of snow grain size (the error bars in figure 7.6).

While technological advance has triggered the development of a number of techniques to measure SSA by optical means, not all of these techniques can provide the high resolution needed for a good quantification of the optical properties of a snow surface. While the stereological method employed here can in principle handle the  $< 1 \text{ mm}$  resolution as shown in this study [Matzl and Schneebeli, 2006], the method by Painter *et al.* [2007] can resolve 2 cm layers, and that by Gallet *et al.* [2009] has a resolution that is dictated by how thin a layer can be collected undisturbed into one snow sample. For those methods to become even more useful in the characterization of the optical properties of natural snow surfaces, it remains a challenge in future development to increase the resolution even further.



## Bibliography

- Albert, M. R., and E. F. Shultz (2002), Snow and firn properties and air-snow transport processes at Summit, Greenland, *Atmos. Environ.*, *36*, 2789–2797.
- Allen, P. A., and J. L. Etienne (2008), Sedimentary challenge to Snowball Earth, *Nat. Geosci.*, *1*, 817–825.
- Alley, R. B., E. S. Saltzman, K. M. Cuffey, and J. J. Fitzpatrick (1990), Summertime formation of depth hoar in Central Greenland, *Geophys. Res. Lett.*, *17*(13), 2393–2396.
- Allison, I., G. Wendler, and U. Radok (1993), Climatology of the East Antarctic ice sheet (100°E to 140°E) derived from automatic weather stations, *J. Geophys. Res. (D)*, *98*(D5), 8815–8823.
- Ambach, W. (1974), The influence of cloudiness on the net radiation balance of a snow surface with high albedo, *J. Glaciol.*, *13*(67), 73–84.
- Anderson, E. A. (1976), A point energy and mass balance model of a snow cover, *Tech. Rep. NWS19*, NOAA.
- Anderson, G. P., S. A. Clough, F. X. Kneizys, J. H. Chetwynd, and E. P. Shettle (1986), AFGL atmospheric constituent profiles (0–120 km), *Tech. Rep. AFGL-TR-86-0110*, Air Force Geophysics Laboratory, Hanscom, MA.
- Andreas, E. L. (1987), A theory for the scalar roughness and the scalar transfer coefficients over snow and sea ice, *Boundary-Layer Meteorol.*, *38*, 159–184.
- Ångström, A., and O. Tryselius (1934), Total radiation from sun and sky at Abisko. (68° 21'.2 N, 18° 49'.3 E), *Geogr. Ann.*, *16*, 53–69.
- Aoki, T., T. Aoki, M. Fukabori, and A. Uchiyama (1999), Numerical simulation of the atmospheric effects on snow albedo with a multiple scattering radiative transfer model for the atmosphere-snow system, *J. Meteorol. Soc. Japan*, *77*(2), 595–614.
- Berk, A., L. S. Bernstein, G. P. Anderson, P. K. Acharya, D. C. Robertson, J. H. Chetwynd, and S. M. Adler-Golden (1998), MODTRAN cloud and multiple scattering upgrades with application to AVIRIS, *Rem. Sens. Environ.*, *65*, 267–375.
- Bintanja, R., and R. S. W. Van de Wal (2008), North American ice-sheet dynamics and the onset of 100,000-year glacial cycles, *Nature*, *545*, 869–872.
- Bintanja, R., and M. R. van den Broeke (1996), The influence of clouds on the radiation budget of ice and snow surfaces in Antarctica and Greenland in summer, *Int. J. Climatol.*, *16*, 1281–1296.
- Boé, J., A. Hall, and X. Qu (2009), September sea-ice cover in the Arctic Ocean projected to vanish by 2100, *Nat. Geosci.*, *2*, 341–343.
- Box, J. E., D. H. Bromwich, B. A. Veenhuis, L.-S. Bai, J. C. Stroeve, J. C. Rogers, K. Steffen, T. Haran, and S.-H. Wang (2006), Greenland ice sheet surface mass balance variability (1988–2004) from calibrated polar MM5 output, *J. Clim.*, *19*, 2783–2800.
- Brandt, R. E., and S. G. Warren (1993), Solar-heating rates and temperature profiles in Antarctic snow and ice, *J. Glaciol.*, *39*(131), 99–110.
- Brock, B. W., I. C. Willis, and M. J. Sharp (2000), Measurement and parameterization of albedo variations at Haut Glacier d'Arolla, Switzerland, *J. Glaciol.*, *46*(155), 675–688.
- Budyko, M. I. (1969), The effect of solar radiation variations on the climate of the Earth, *Tellus*, *21*(5), 611–619.
- Carroll, J. J., and B. W. Fitch (1981), Effects of solar elevation and cloudiness on snow albedo at the South Pole, *J. Geophys. Res. (C)*, *86*(C6), 5271–5276.
- Chandrasekhar, S. (1950), *Radiative transfer*, Oxford University Press, London, New York.
- Clarke, A. D., and K. J. Noone (1985), Soot in the Arctic snowpack: A cause for perturbation in radiative transfer, *Atmos. Environ.*, *19*, 2045–2053.
- Colbeck, S. C. (1989a), Air movement in snow due to windpumping, *J. Glaciol.*, *35*(120), 209–213.

- Colbeck, S. C. (1989b), Snow-crystal growth with varying surface temperatures and radiation penetration, *J. Glaciol.*, 35(119), 23–29.
- Cullen, N. J., and K. Steffen (2001), Unstable near-surface boundary conditions in summer on top of the Greenland ice sheet, *Geophys. Res. Lett.*, 28(23), 4491–4493.
- Cullen, N. J., K. Steffen, and P. D. Blanken (2007), Nonstationarity of turbulent heat fluxes at Summit, Greenland, *Boundary-Layer Meteorol.*, 122, 439–455.
- Dadic, R., M. Schneebeli, M. Lehning, M. A. Hutterli, and A. Ohmura (2008), Impact of the microstructure of snow on its temperature: A model validation with measurements from Summit, Greenland, *J. Geophys. Res. (D)*, 113(D14303), doi:10.1029/2007JD009562.
- De Haan, J. F., P. B. Bosma, and J. W. Hovenier (1987), The adding method for multiple scattering calculations of polarized light, *Astron. Astrophys.*, 183, 371–391.
- De Rooij, W. A., and C. C. A. H. van der Stap (1984), Expansion of Mie scattering matrices in generalized spherical functions, *Astron. Astrophys.*, 131, 237–248.
- Deepak, A., and H. E. Gerber (Eds.) (1983), *WCP-55. World Climate Research report of the experts meeting on aerosols and their climatic effects.*, Williamsburg, Virginia, 28–30 March 1983.
- Dobbins, R. A., and G. S. Jizmagian (1966), Optical scattering cross sections for polydispersions of dielectric spheres, *J. Opt. Soc. Am.*, 56, 1345–1350.
- Domine, F., R. Salvatori, L. Legagneux, R. Salzano, M. Fily, and R. Casacchia (2006), Correlation between the specific surface area and the short wave infrared (SWIR) reflectance of snow, *Cold Reg. Sci. Technol.*, 46, 60–68.
- Dubovik, O., A. Smirnov, B. N. Holben, M. D. King, Y. J. Kaufman, T. F. Eck, and I. Slutsker (2000), Accuracy assessments of aerosol optical properties retrieved from Aerosol Robotic Network (AERONET) sun and sky radiance measurements, *J. Geophys. Res. (D)*, 105(D8), 9791–9806.
- Dürr, B., and R. Philipona (2004), Automatic cloud amount detection by surface longwave downward radiations measurements, *J. Geophys. Res. (D)*, 109, doi:10.1029/2004JD004182.
- Dyer, A. J. (1974), A review of flux-profile relationships, *Boundary-Layer Meteorol.*, 7, 363–372.
- Dyurgerov, M., and M. F. Meier (2005), *Glaciers and the changing Earth system: a 2004 snapshot*, Occasional paper 58, 118 pp., Institute of Arctic and Alpine Research, Boulder, CO.
- Ettema, J., M. R. van den Broeke, E. van Meijgaard, W. J. van de Berg, J. L. Bamber, J. E. Box, and R. C. Bales (2009), Higher surface mass balance of the Greenland ice sheet revealed by high-resolution climate modelling, *Geophys. Res. Lett.*, 36, L12,501, doi:10.1029/2009GL038110.
- Fettweis, X., J. P. van Ypersele, H. Gallée, F. Lefebvre, and W. Lefebvre (2007), The 1979–2005 Greenland ice sheet melt extent from passive microwave data using an improved version of the melt retrieval XPGR algorithm, *Geophys. Res. Lett.*, 34, L05,502, doi:10.1029/2006GL028787.
- Fitzpatrick, M. F., R. E. Brandt, and S. G. Warren (2004), Transmission of solar radiation by clouds over snow and ice surfaces: a parameterization in terms of optical depth, solar zenith angle, and surface albedo, *J. Clim.*, 17, 266–275.
- Flanner, M. G., and C. S. Zender (2006), Linking snowpack microphysics and albedo evolution, *J. Geophys. Res. (D)*, 111, D12,208, doi:10.1029/2005JD006834.
- Flanner, M. G., C. S. Zender, J. T. Randerson, and P. J. Rasch (2007), Present-day climate forcing and response from black carbon in snow, *J. Geophys. Res. (D)*, 112, D11,202, doi:10.1029/2006JD008003.
- Gallet, J.-C., F. Domine, C. S. Zender, and G. Picard (2009), Rapid and accurate measurement of the specific surface area of snow using infrared reflectance at 1310 and 1550 nm, *The Cryosphere Discuss.*, 3(1), 33–75.
- Gay, M., M. Fily, C. Genthon, M. Frezzotti, H. Oerter, and J. G. Winther (2002), Snow grain-size measurements in Antarctica, *J. Glaciol.*, 48(163), 527–535.
- Giesen, R. H., M. R. van den Broeke, J. Oerlemans, and L. M. Andreassen (2008), Surface energy balance in the ablation zone of Middalsbreen, a glacier in southern Norway: interannual variability and the effect of clouds, *J. Geophys. Res. (D)*, 113, D21,111, doi:10.1029/2008JD010390.
- Giesen, R. H., L. M. Andreassen, M. R. van den Broeke, and J. Oerlemans (2009), Comparison of the meteorology and surface energy balance at Storbreen and Middalsbreen, two glaciers in southern Norway, *The Cryosphere*, 3, 57–74.
- Grenfell, T. C., and G. A. Maykut (1977), The optical properties of ice and snow in the Arctic basin, *J. Glaciol.*,

- 18(80), 445–463.
- Grenfell, T. C., and D. K. Perovich (1984), Spectral albedos of sea ice and incident solar irradiance in the southern Beaufort Sea, *J. Geophys. Res.*, *89*, 3573–3580.
- Grenfell, T. C., and S. G. Warren (1999), Representation of a nonspherical ice particle by a collection of independent spheres for scattering and absorption of radiation, *J. Geophys. Res. (D)*, *104*(D24), 31,697–31,709.
- Grenfell, T. C., S. G. Warren, and P. C. Mullen (1994), Reflection of solar radiation by the Antarctic snow surface at ultraviolet, visible, and near-infrared wavelengths, *J. Geophys. Res. (D)*, *99*(D9), 18,669–18,684.
- Greuell, W., and J. Oerlemans (2004), Narrowband-to-broadband albedo conversion for glacier ice and snow: equations based on modeling and ranges of validity of the equations, *Rem. Sens. Environ.*, *89*, 95–105.
- Greuell, W., W. H. Knap, and C. J. P. P. Smeets (1997), Elevational changes in meteorological variables along a midlatitude glacier during summer, *J. Geophys. Res. (D)*, *102*(D22), 25,941–25,954.
- Griggs, J. A., and J. L. Bamber (2008), Assessment of cloud cover characteristics in satellite datasets and reanalysis products for Greenland, *J. Clim.*, *21*, 1837–1849.
- Gueymard, C. A. (2001), Parameterized transmittance model for direct beam and circumsolar spectral irradiance, *Solar Energy*, *71*(5), 325–346.
- Gueymard, C. A. (2004), The sun's total and spectral irradiance for solar energy applications and solar radiation models, *Solar Energy*, *76*, 423–453.
- Hagler, G. S. W., M. H. Bergin, E. A. Smith, and J. E. Dibb (2007), A summer time series of particulate carbon in the air and snow at Summit, Greenland, *J. Geophys. Res. (D)*, *112*, D21,309, doi:10.1029/2007JD008993.
- Hays, J. D., J. Imbrie, and N. J. Shackleton (1976), Variations in the Earth's orbit: pacemaker of the ice ages, *Science*, *194*(4270), 1121–1132.
- Henzing, J. S., W. H. Knap, P. Stammes, A. Apituley, J. B. Bergwerff, D. P. J. Swart, G. P. A. Kos, and H. M. ten Brink (2004), Effect of aerosols on the downward shortwave irradiances at the surface: measurements versus calculations with MODTRAN 4.1, *J. Geophys. Res. (D)*, *109*, D14,204, doi:10.1029/2003JD004142.
- Hess, M., R. B. A. Koelmeijer, and P. Stammes (1998a), Scattering matrices of imperfect hexagonal ice crystals, *J. Quant. Spectrosc. Radiat. Transfer*, *60*(3), 301–308.
- Hess, M., P. Koepke, and I. Schult (1998b), Optical properties of aerosols and clouds: the software package OPAC, *Bull. Am. Meteorol. Soc.*, *79*(2), 831–844.
- Hoch, S. W. (2005), Radiative flux divergence in the surface boundary layer. A study based on observations at Summit, Greenland, Ph.D. thesis, Swiss Federal Institute of Technology, Zürich.
- Hoffmann, P. F., A. J. Kaufman, G. P. Halverson, and D. P. Schrag (1998), A Neoproterozoic Snowball Earth, *Science*, *281*, 1342–1346.
- Holtslag, A. A. M., and H. A. R. de Bruin (1988), Applied modelling of the night-time surface energy balance over land, *J. Appl. Meteorol.*, *27*, 689–704.
- Hovenier, J. W., C. van der Mee, and H. Domke (2004), *Transfer of polarized light in planetary atmospheres*, Kluwer Academic Publishers, Dordrecht, The Netherlands.
- IPCC (2007), Climate change 2007: The physical science basis. Contribution of working groups I to the fourth assessment report of the Intergovernmental Panel on Climate Change.
- Jonsell, U., R. Hock, and B. Holmgren (2003), Spatial and temporal variations in albedo on Storglaciären, Sweden, *J. Glaciol.*, *49*(164), 59–68.
- Kärkäs, E., H. Granberg, K. Kanto, K. Rasmus, C. Lavoie, and M. Leppäranta (2002), Physical properties of the seasonal snow cover in Dronning Maud Land, East Antarctica, *Ann. Glaciol.*, *34*, 89–94.
- Kato, S., T. P. Ackerman, J. H. Mather, and E. E. Clothiaux (1999), The k-distribution method and correlated-k approximation for a shortwave radiative transfer model, *J. Quant. Spectrosc. Radiat. Transfer*, *62*, 109–121.
- Knap, W. H., C. H. Reijmer, and J. Oerlemans (1999), Narrowband to broadband conversion of Landsat-TM glacier albedos, *Int. J. Remote Sens.*, *20*(10), 2091–2110.
- Knap, W. H., L. C. Labonnote, G. Brogniez, and P. Stammes (2005), Modeling total and polarized reflectances of ice clouds: evaluation by means of POLDER and ATSR-2 measurements, *Appl. Opt.*, *44*(19), 4060–4073.
- Kneizys, F. X., E. P. Shettle, L. W. Abreu, J. H. Chetwynd, G. P. Anderson, W. O. Gallery, J. E. A. Selby, and S. A. Clough (1988), *A users guide to LOWTRAN7*, Air Force Geophysics Laboratory, Hanscom AFB, MA 01731.
- König-Langlo, G., and A. Herber (1996), The meteorological data of the Neumayer Station (Antarctica) for 1992,

- 1993 and 1994, *Ber. Polarforsch.* 187, Alfred Wegener Institute for Polar and Marine Research, Bremerhaven.
- König-Langlo, G., J. C. King, and P. Pettré (1998), Climatology of the three coastal Antarctic stations Dumont d'Urville, Neumayer, and Halley, *J. Geophys. Res. (D)*, 103(D9), 10,935–10,946.
- Konzelmann, T., R. S. W. van de Wal, W. Greuell, R. Bintanja, E. A. C. Henneken, and A. Abe-Ouchi (1994), Parameterization of global and longwave incoming radiation for the Greenland Ice Sheet, *Glob. Plan. Change*, 9, 143–164.
- Kuhn, M., and L. Siogas (1978), Spectroscopic studies at McMurdo, South Pole, and Siple stations during the austral summer 1977-78, *Antarct. J. US*, 13, 178–179.
- Lacis, A. A., and V. Oinas (1991), A description of the correlated k distribution method for modeling nongray gaseous absorption, thermal emission, and multiple scattering in vertically inhomogeneous atmospheres, *J. Geophys. Res. (D)*, 96(D5), 9027–9063.
- Legagneux, L., and F. Domine (2005), A mean field model of the decrease of the specific surface area of dry snow during isothermal metamorphism, *J. Geophys. Res. (F)*, 110, F04,011, doi:10.1029/2004JF000181.
- Legagneux, L., A. Cabanes, and F. Domine (2002), Measurement of the specific surface area of 176 snow samples using methane adsorption at 77 K, *J. Geophys. Res. (D)*, 107(D17), 4335, doi:10.1029/2001JD001016.
- Legagneux, L., A. S. Taillandier, and F. Domine (2006), Grain growth theories and the isothermal evolution of the specific surface area of snow, *J. Appl. Phys.*, 95(11), 6175–6184.
- Liljequist, G. H. (1956), Energy exchange of an Antarctic snow field: Short-wave radiation (Maudheim 71°03' S, 10°56' W), in *Norwegian-British-Swedish Antarctic Expedition, 1949-52, Scientific Results*, vol. 2, part 1A, Norsk Polarinstitut, Oslo.
- Liou, K. N. (2002), *An introduction to atmospheric radiation*, 2<sup>nd</sup> ed., Academic Press Inc., San Diego, USA.
- Liston, G. E., and J. G. Winther (2005), Antarctic surface and subsurface snow and ice melt fluxes, *J. Clim.*, 18, 1469–1481.
- Long, C. N., and T. P. Ackerman (2000), Identification of clear skies from broadband pyranometer measurements and calculation of downwelling shortwave cloud effects, *J. Geophys. Res. (D)*, 105(D12), 15,609–15,626.
- Macke, A., J. Mueller, and E. Raschke (1996), Single scattering properties of atmospheric ice crystals, *J. Atmos. Sci.*, 53(19), 2813–2825.
- Mahesh, A., V. P. Walden, and S. G. Warren (2001), Ground-based infrared remote sensing of cloud properties over the Antarctic plateau. Part II: cloud optical depths and particle sizes, *J. Appl. Meteorol.*, 40, 1279–1294.
- Marty, C., and R. Philipona (2000), The clear-sky index to separate clear-sky from cloudy-sky situations in climate research, *Geophys. Res. Lett.*, 27(17), 2649–2652.
- Matson, D. L., and R. H. Brown (1989), Solid-state greenhouses and their implications for icy satellites, *Icarus*, 77(1), 67–81.
- Matzl, M. (2006), Quantifying the stratigraphy of snow profiles, Ph.D. thesis, Swiss Federal Institute of Technology, Zürich.
- Matzl, M., and M. Schneebeli (2006), Measuring specific surface area of snow by near-infrared photography, *J. Glaciol.*, 52(179), 558–564.
- Meirolid-Mautner, I., and M. Lehning (2004), Measurements and model calculations of the solar shortwave fluxes in snow on Summit, Greenland, *Ann. Glaciol.*, 38, 279–284.
- Meyers, T. P., and R. F. Dale (1983), Predicting daily insolation with hourly cloud height and coverage, *J. Clim. Appl. Meteorol.*, 22, 537–545.
- Michalsky, J. J., G. P. Anderson, J. Barnard, J. Delamare, C. Gueymard, S. Kato, P. Kiedron, A. McComiskey, and P. Ricchiazzi (2006), Shortwave radiative closure studies from clear skies during the Atmospheric Radiation Measurement 2003 Aerosol Intensive Observation Period, *J. Geophys. Res. (D)*, 111, D14S20, doi:10.1029/2005JD006341.
- Milanković, M. (1930), *Mathematische Klimalehre und Astronomische Theorie der Klimaschwankungen. Handbuch der Klimologie Band 1*, Borntrager, Berlin.
- Mishchenko, M. I. (2008), Multiple scattering, radiative transfer, and weak localization in discrete random media: unified microphysical approach, *Rev. Geophys.*, 46.
- Mishchenko, M. I., L. D. Travis, and A. A. Lacis (2006), *Multiple scattering of light by particles: radiative transfer and coherent backscattering*, Cambridge University Press, Cambridge, UK.

- Mitchell, D. L. (2002), Effective diameter in radiation transfer: General definition, applications, and limitations, *J. Atmos. Sci.*, 59, 2330–2346.
- Neshyba, S. P., T. C. Grenfell, and S. G. Warren (2003), Representation of a nonspherical ice particle by a collection of independent spheres for scattering and absorption of radiation: 2. Hexagonal columns and plates, *J. Geophys. Res. (D)*, 108(D15), doi:10.1029/2002JD003302.
- Nolin, A. W., and J. Dozier (2000), A hyperspectral method for remotely sensing the grain size of snow, *Rem. Sens. Environ.*, 74(2), 207–216.
- Oerlemans, J., R. H. Giesen, and M. R. van den Broeke (2009), Retreating alpine glaciers: increased melt rates due to accumulation of dust (Vadret da Morteratsch, Switzerland), *J. Glaciol.*, 55(192), in press.
- Ohmura, A., et al. (1998), Baseline Surface Radiation Network (BSRN/WCRP): new precision radiometry for climate research, *Bull. Am. Meteorol. Soc.*, 79(10), 2115–2136.
- Painter, T. H., N. P. Molotch, M. Cassidy, M. G. Flanner, and K. Steffen (2007), Contact spectroscopy for determination of stratigraphy of snow optical grain size, *J. Glaciol.*, 53(180), 121–127.
- Potter, J. F. (1970), The delta function approximation in radiative transfer theory, *J. Atmos. Sci.*, 27, 943–949.
- Reijmer, C. H., and J. Oerlemans (2002), Temporal and spatial variability of the surface energy balance in Dronning Maud Land, East Antarctica, *J. Geophys. Res. (D)*, 107(D24), 4759–4770.
- Reijmer, C. H., E. van Meijgaard, and M. R. van den Broeke (2005), Evaluation of temperature and wind over Antarctica in a Regional Atmospheric Climate Model using 1 year of automatic weather station data and upper air observations, *J. Geophys. Res. (D)*, 110, doi:10.1029/2004JD005234.
- Ricchiuzzi, P., C. Gautier, and D. Lubin (1995), Cloud scattering optical depth and local surface albedo in the Antarctic: Simultaneous retrieval using ground-based radiometry, *J. Geophys. Res. (D)*, 100(D10), 21,091–21,104.
- Rignot, E., J. L. Bamber, M. R. van den Broeke, C. Davis, Y. Li, W. J. van de Berg, and E. van Meijgaard (2008), Recent Antarctic ice mass loss from radar interferometry and regional climate modelling, *Nat. Geosci.*, 1, 106–110.
- Rusin, N. P. (1961), Meteorological and radiational regime of Antarctica, *Tech. rep.*, Israel program for scientific translations, Jerusalem.
- Scambos, T. A., T. M. Haran, M. A. Fahnestock, T. H. Painter, and J. Bohlander (2007), MODIS-based Mosaic of Antarctica (MOA) data sets: continent-wide surface morphology and snow grain size, *Rem. Sens. Environ.*, 111(2-3), 242–257.
- Schlatter, T. W. (1972), The local surface energy balance and subsurface temperature regime in Antarctica, *J. Appl. Meteorol.*, 11(10), 1048–1062.
- Schneider, S. H., and R. E. Dickinson (1976), Parameterization of fractional cloud amounts in climatic models: the importance of modeling multiple reflections, *J. Appl. Meteorol.*, 15, 1050–1056.
- Shepherd, A., and D. Wingham (2007), Recent sea-level contributions of the Antarctic and Greenland ice sheets, *Science*, 315, 1529–1532.
- Shi, Y., and C. N. Long (2002), Techniques and methods used to obtain the best estimate of radiation fluxes at SGP central facility, in *Proceedings of the twelfth ARM science team meeting*, edited by D. Carrothers, U. S. Department of Energy, Richland, WA.
- Shine, K. P. (1984), Parameterisation of the shortwave flux over high albedo surfaces as a function of cloud thickness and surface albedo, *Quart. J. Roy. Meteorol. Soc.*, 110, 747–764.
- Stam, D., J. F. de Haan, J. W. Hovenier, and P. Stammes (2000), A fast method for simulating observations of polarized light emerging from the atmosphere applied to the oxygen-A band, *J. Quant. Spectrosc. Radiat. Transfer*, 64, 131–149.
- Stammes, P. (2001), Spectral radiance modelling in the UV–Visible range, in *IRS 2000: Current problems in atmospheric radiation*, edited by W. L. Smith and Y. M. Timofeyev, pp. 385–388, A. Deepak Publ, Hampton, VA.
- Stammes, P., J. F. de Haan, and J. W. Hovenier (1989), The polarized internal radiation field of a planetary atmosphere, *Astron. Astrophys.*, 225, 239–259.
- Stearns, C. R., and G. Wendler (1988), Research results from Antarctic automatic weather stations, *Rev. Geophys.*, 26(1), 45–61.
- Stephens, G. L. (1984), The parameterization of radiation for numerical weather prediction and climate models,

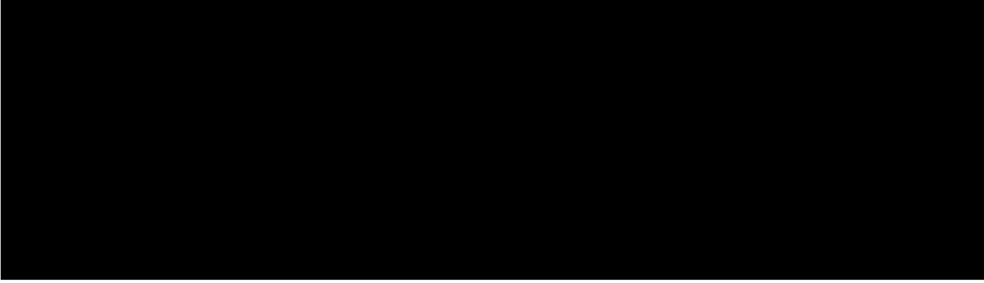
- Mon. Wea. Rev.*, 112, 826–867.
- Thomas, G. E., and K. Stamnes (1999), *Radiative transfer in the atmosphere and ocean*, 1<sup>st</sup> ed., Cambridge University Press, Cambridge.
- Town, M. S., V. P. Walden, and S. G. Warren (2007), Cloud cover over the South Pole from visual observations, satellite retrievals, and surface-based infrared radiation measurements, *J. Clim.*, 20, 544–559.
- Van As, D., M. R. van den Broeke, C. H. Reijmer, and R. S. W. van de Wal (2005a), The summer surface energy balance of the high Antarctic Plateau, *Boundary-Layer Meteorol.*, 115, 289–317.
- Van As, D., M. R. van den Broeke, and R. S. W. van de Wal (2005b), Daily cycle of the surface layer and energy balance on the high antarctic plateau, *Antarct. Sci.*, 17, 121–133.
- Van de Hulst, H. C. (1963), A new look at multiple scattering, *Tech. rep.*, Inst. Space Studies, NASA, New York.
- Van den Berg, W. J., M. R. van den Broeke, C. H. Reijmer, and E. van Meijgaard (2006), Reassessment of the Antarctic surface mass balance using calibrated output of a regional atmospheric climate model, *J. Geophys. Res. (D)*, 111, D11,104, doi:10.1029/2005JD006495.
- Van den Broeke, M. R., C. H. Reijmer, and R. S. W. van de Wal (2004a), Surface radiation balance in Antarctica as measured with automatic weather stations, *J. Geophys. Res. (D)*, 109, D09,103, doi:10.1029/2003JD004394.
- Van den Broeke, M. R., C. H. Reijmer, and R. S. W. van de Wal (2004b), A study of the surface mass balance in Dronning Maud Land, Antarctica, using automatic weather stations, *J. Glaciol.*, 50(171), 565–582.
- Van den Broeke, M. R., D. van As, C. H. Reijmer, and R. S. W. van de Wal (2004c), Assessing and improving the quality of unattended radiation observations in Antarctica, *J. Atm. Oc. Technol.*, 21, 1417–1431.
- Van den Broeke, M. R., C. H. Reijmer, D. van As, R. S. W. van de Wal, and J. Oerlemans (2005), Seasonal cycles of Antarctic surface energy balance from automatic weather stations, *Ann. Glaciol.*, 41, 131–139.
- Van den Broeke, M. R., C. H. Reijmer, D. van As, and W. Boot (2006), Daily cycle of the surface energy balance in Antarctica and the influence of clouds, *Int. J. Climatol.*, 26, 1587–1605.
- Van den Broeke, M. R., C. J. P. P. Smeets, J. Ettema, and P. Kuipers Munneke (2008a), Surface radiation balance in the ablation zone of the West Greenland ice sheet, *J. Geophys. Res. (D)*, 113, D13,105, doi: 10.1029/2007JD009283.
- Van den Broeke, M. R., C. J. P. P. Smeets, J. Ettema, C. van der Veen, R. S. W. van de Wal, and J. Oerlemans (2008b), Partitioning of melt energy and meltwater fluxes in the ablation zone of the west Greenland ice sheet, *The Cryosphere*, 2, 179–189.
- Van den Broeke, M. R., G. König-Langlo, G. Picard, P. Kuipers Munneke, and J. Lenaerts (2009), Surface energy balance, melt and sublimation at Neumayer station (East Antarctica), *Antarct. Sci.*, in press.
- Wang, P., W. H. Knap, P. Kuipers Munneke, and P. Stamnes (2008), Clear-sky atmospheric radiative transfer: a model intercomparison for shortwave irradiances, in *IRS 2008: Current problems in atmospheric radiation*.
- Wang, P., W. H. Knap, P. Kuipers Munneke, and P. Stamnes (2009), Clear-sky shortwave radiative closure for the Cabauw Baseline Surface Radiation Network site, the Netherlands, *J. Geophys. Res. (D)*, 114, D14,206, doi: 10.1029/2009JD011978.
- Warren, S. G. (1982), Optical properties of snow, *Rev. Geophys. Space Phys.*, 20(1), 67–89.
- Warren, S. G. (1984), Optical constants of ice from the ultraviolet to the microwave, *Appl. Opt.*, 23(8), 1206–1225.
- Warren, S. G., and A. D. Clarke (1990), Soot in the atmospheric and snow surface of Antarctica, *J. Geophys. Res. (D)*, 95(D2), 1811–1816.
- Warren, S. G., and W. J. Wiscombe (1980), A model for the spectral albedo of snow. II: Snow containing atmospheric aerosols, *J. Atmos. Sci.*, 37, 2734–2745.
- Warren, S. G., and W. J. Wiscombe (1985), Dirty snow after nuclear war, *Nature*, 313, 467–470.
- Warren, S. G., R. E. Brandt, and T. C. Grenfell (2006), Visible and near-ultraviolet absorption spectrum of ice from transmission of solar radiation into snow, *Appl. Opt.*, 45(21), 5320–5334.
- Wild, M., et al. (2005), From dimming to brightening: decadal changes in colar radiation at Earth’s surface, *Science*, 308, 847–850.
- Wiscombe, W. J., and S. G. Warren (1980), A model for the spectral albedo of snow. I: Pure snow, *J. Atmos. Sci.*, 37, 2712–2733.
- Wuttke, S., G. Seckmeyer, and G. König-Langlo (2006), Measurements of spectral snow albedo at Neumayer, Antarctica, *Ann. Geophys.*, 24, 7–21.

- Zachos, J., M. Pagani, L. Sloan, E. Thomas, and K. Billups (2001), Trends, rhythms, and aberrations in global climate 65 Ma to present, *Nature*, 292, 686–693.
- Zeng, Q., M. Cao, X. Feng, F. Liang, X. Chen, and W. Sheng (1984), A study of spectral reflection characteristics for snow, ice and water in the north of China, in *Hydrological applications of remote sensing and remote data transmission*, vol. 145, edited by B. Goodison, pp. 451–462, IAHS.
- Zhou, X., S. Li, and K. Stamnes (2003), Effects of vertical inhomogeneity on snow spectral albedo and its implication for optical remote sensing of snow, *J. Geophys. Res. (D)*, 108(D23), doi:10.1029/2003JD003859.





## Dankwoord



[Redacted text block]



## Curriculum vitae

Peter Kuipers Munneke werd geboren op 31 maart 1980 te Groningen. Hij groeide op in Annen en Zuidlaren. In 1998 behaalde hij zijn VWO-diploma aan het Willem Lodewijk Gymnasium te Groningen. Behoudens wat uitstapjes in de Zweedse Taal- en Letterkunde en Technische Planologie, volgde hij van 1999 tot 2005 de opleiding Natuurkunde aan de Rijksuniversiteit Groningen. In de loop van zijn studie raakte hij geïnteresseerd in de fysica van het klimaatsysteem, en volgde daarin een groot aantal vakken, ook aan de Universiteit Utrecht. Peter combineerde zijn interesse voor gletsjers met die voor de Zweedse taal tijdens een afstudeeronderzoek aan de Universiteit van Uppsala, onder begeleiding van dr. Veijo Pohjola en prof. dr. Harro Meijer. Gegevens die hij verzamelde tijdens een veldwerkonderzoek in Svalbard, Noorwegen, gebruikte hij om historische lengteveranderingen van de gletsjer Nordenskiöldbreen te modelleren. In 2005 studeerde hij hierop ‘met veel genoegen’ af en begon aansluitend aan een promotieonderzoek aan het Instituut voor Marien en Atmosferisch onderzoek Utrecht onder begeleiding van dr. Carleen Tijm-Reijmer (co-promotor) en prof. dr. Johannes Oerlemans (promotor). Tijdens zijn promotie zette hij een veldwerkonderzoek op dat in juni en juli 2007 werd uitgevoerd op de Groenlandse ijskap. De komende drie jaar zal hij als post-doc onderzoek doen naar het voorkomen van smeltperiodes op de Antarctische ijskap samen met prof. dr. Michiel van den Broeke.



## Publications

Kuipers Munneke, P., C. H. Reijmer, M. R. van den Broeke, P. Stammes, G. König-Langlo, and W. H. Knap (2008), Analysis of clear-sky Antarctic snow albedo using observations and radiative transfer modeling, *J. Geophys. Res. (D)*, *113*, D17,118, doi:10.1029/2007JD009653.

Kuipers Munneke, P., M. R. van den Broeke, C. H. Reijmer, M. M. Helsen, W. Boot, M. Schneebeli, and K. Steffen (2009), The role of radiation penetration in the energy budget of the snowpack at Summit, Greenland, *The Cryosphere*, *3*, 155–165.

Kuipers Munneke, P., C. H. Reijmer, and M. R. van den Broeke (2009), Assessing the retrieval of cloud properties from radiation measurements over snow and ice, *submitted to Int. J. Climatol.*

Kuipers Munneke, P., C. H. Reijmer et al. (2009), Observation and modeling of spectral snow albedo, *in preparation*.

Van den Broeke, M. R., C. J. P. P. Smeets, J. Ettema, and P. Kuipers Munneke (2008), Surface radiation balance in the ablation zone of the West Greenland ice sheet, *J. Geophys. Res. (D)*, *113*, D13,105, doi:10.1029/2007JD009283.

Wang, P., W. H. Knap, P. Kuipers Munneke, and P. Stammes (2008), Clear-sky atmospheric radiative transfer: a model intercomparison for shortwave irradiances, in *IRS 2008: Current problems in atmospheric radiation*.

Van den Broeke, M. R., G. König-Langlo, G. Picard, P. Kuipers Munneke, and J. Lenaerts (2009), Surface energy balance, melt and sublimation at Neumayer station (East Antarctica), *Antarct. Sci.*, *in press*.

Wang, P., W. H. Knap, P. Kuipers Munneke, and P. Stammes (2009), Clear-sky shortwave radiative closure for the Cabauw Baseline Surface Radiation Network site, the Netherlands, *J. Geophys. Res. (D)*, *114*, D14,206, doi:10.1029/2009JD011978.

